ABSTRACT

Title of Dissertation:	Effect of Protein Folding State and Conformational Fluctuations on Hydrogel Formation and Protein Aggregation
	Shakiba Nikfarjam, Doctor of Philosophy, 2022
Dissertation directed by:	Professor Taylor J Woehl, Department of Chemical and Biomolecular Engineering
Dissertation co-directed by:	Professor Mikhail Anisimov, Department of Chemical and Biomolecular Engineering

In this thesis we investigate the role of protein unfolding on protein aggregation and hydrogel formation in two different systems. In the context of designing protein-based hydrogels as biomaterials, we investigate how protein unfolding affects the formation dynamics of hydrogels in response to temperature changes, denaturation, and chemical reactions. In a second context we establish how microsecond to millisecond fluctuations in an amyloid forming protein, beta-2-microglobulin, correlate to the amyloid forming propensity of the protein, with an emphasis on understanding how conformational changes in the native folded state provide thermodynamic driving forces for amyloid nucleation.

The work on protein hydrogel yielded two key results. First, we observed that the lifetime of dissipative hydrogels decreased and their mechanical stiffness increased with increasing denaturant concentration and constant fuel concentration. At a higher denaturant concentration,

the concentration of solvent-accessible cysteines increases the stiffness of the hydrogel at the cost of a faster consumption of H_2O_2, which is the cause of the shorter gel lifetime. This work utilizing biological macromolecules in kinetically controlled dissipative structures opens the door to future applications of such systems in which the biomolecules' structures can control the reaction kinetics.

Another substantial outcome of our work is to uncover mechanisms underlying the initiation of nucleation in the initial stages of amyloid aggregate formation. The study of conformational fluctuations in the structure of the amyloid-forming protein beta 2-microglobulin (β_2M) yielded three key results. First, β_2M variants' aggregation propensity correlates with their conformational fluctuations rate. A longer-lived misfolded subpopulation increases the chance of aggregation initiation by increasing the collision chance of the protein's sticky regions. Second, the observed millisecond interconversions agree with the timescales required for the interconversion of a protein's structure between its subpopulations. Third, the fluctuations themselves could be a driving force for the nucleation of aggregates by decreasing the lag-time of nucleus formation by a sudden large fluctuation.

EFFECT OF PROTEIN FOLDING STATE AND CONFORMATIONAL FLUCTUATIONS ON HYDROGEL FORMATION AND PROTEIN AGGREGATION

by

Shakiba Nikfarjam

Dissertation submitted to the Faculty of the Graduate School of the
University of Maryland, College Park, in partial fulfillment
of the requirements for the degree of
Doctor of Philosophy
2022

Advisory Committee:
Professor Taylor J Woehl, Chair
Professor Mikhail Anisimov, Co-chair
Professor Amy J Karlsson
Professor Srinivasa Raghavan
Professor Silvina R. Matysiak

Dedication

I dedicate my PhD dissertation to my parents and sisters for all the encouragements and support they provided me throughout my PhD studies.

Acknowledgements

I want to express my warmest thanks to my PhD advisors, Professor Taylor Woehl, and Professor Mikhail Anisimov. Thank you so much for trusting, encouraging, and supporting me in all the ups and downs throughout the seven years of my studies under your supervision. You turned me into an independent scientist and helped me build my confidence. I will always be thankful.

Dear Professor Karlsson, thank you for giving me valuable advice from the first days I entered graduate school. Your warmth and positivity is the first thing I remember about you. And thank you so much for providing me with valuable research guidance and allowing me to use your lab space. It felt like my second home.

I also want to thank my dearest friend Marzyeh Kheradmand who sincerely helped me, supported me in any way you could, and shared your knowledge with me. Your support made my work much less difficult and made my time in the lab enjoyable. I would also like to thank awesome Dinara Konakbaya and Wright Makambi for being great friends and always being there for me.

I also thank my fellow lab members of both Woehl lab and Karlsson lab. Dr. Mei Wang, Umesha Dissayanake, and Medha Ruth, for their friendship, love, and support. You are the best lab mates I could ask for.

I also want to thank Elene Jouravleva, who was my best mentor. Your encouragement, warmth, and support were a substantial help throughout these years.

I also want to acknowledge the Army research office award #W911NF-20-1-0169 for providing funding for part of this research.

Table of Contents

Dedication ii
Acknowledgements iii
Table of Contents iv
List of Tables vii
List of Figures viii
List of Abbreviations xiii
Chapter 1: Introduction 1
1.1 Protein Folding, Conformational Energy Landscape and Aggregation 1
1.1.1 Protein folding and Energy Landscape 1
1.1.2 Protein Aggregation and Amyloid Formation 7
1.1.2.1 Importance of Protein Aggregation 8
1.1.2.2 Protein Aggregation *in vivo* 9
1.1.2.3 Amyloid Fibrils 10
1.1.2.4 Early Stages of Amyloid Formation 11
1.1.3 Beta 2-Microglobulin 13
1.2 Dynamic Light Scattering 16
1.2.1 Basics of Light Scattering 16
1.2.2 Light Scattering Instrument 20
1.3 Fluorescence Techniques 20
1.3.1 Fluorescence Spectroscopy 20
1.3.2 Fluorescence Resonance Energy Transfer (FRET) 26
1.3.3 Fluorescence Correlation Spectroscopy (FCS) 30
1.3.4 FCS-FRET Technique 32
1.4 Goals and Outline of The Dissertation 33
Chapter 2: Effect of Protein Unfolding on Aggregation and Gelation in Lysozyme Solutions 37
2.1 Introduction 38
2.2 Materials and Methods 40
2.3 Results 41
2.3.1 Apparent Monomer Size 41
2.3.2 Continuous Heating 43
2.3.3 Preventing Gelation and Long-Time Monitoring 46
2.3.4 Formation of Polydisperse Aggregates 49
2.4 Discussion 52
2.5 Conclusions 55
Chapter 3: Chemically Fueled Dissipative Assembly of Protein Hydrogels Mediated by Protein Unfolding 57
3.1 Introduction 57
3.2 Experimental Section 59
3.2.1 Reagents and Hydrogel Preparation 59
3.2.2 Dynamic Light Scattering 60

3.2.3 Intrinsic Fluorescence and ANS Binding 61
3.2.4 Free Cysteine Concentration and Crosslinking Density 62
3.2.5 Rheology Measurements 63
3.2.6 Microscopy and Fluorescence Imaging Spectroscopy 63
3.3 Results and Discussion 64
3.3.1 Redox Cycle for Dissipative Assembly 64
3.3.2 Hydrogel Lifetime Measurements 66
3.3.3 Viscoelastiv Properties of Hydrogels 70
3.3.4 Protein Unfolding and Solvent Exposed Cysteines 71
3.3.5 H_2O_2 Consumption Rate 73
3.3.6 Varying the Redox Reaction Rates 75
3.3.7 Mechanism for The Effect of Protein Unfolding on Dissipative Assembly 76
3.4 Conclusions 79
Chapter 4: Enhanced Recombinant Production and Purification of Beta 2-microglobulin using SUMO as a Soluble Partner 80
4.1 Introduction 80
4.2 Methods 81
4.2.1 Plasmid Construction 81
4.2.1.1 Construct 1 (6xHis-TEV-β_2M) 81
4.2.1.2 Construct 2 (6xHis-SUMO-β_2M) 82
4.2.2 Site Direscted Mutagenesis 85
4.2.3 Protein Expression in Bacterial Strains 87
4.2.4 Protein Extraction, P`urification, and Refolding from Inclusion Bodies 88
4.3 Results and Discussion 90
4.3.1 Comparison of β_2M From the Two Constructs and Challenges 90
4.3.1.1 Comparison of Expression Level in Soluble and Insoluble Fractions 90
4.3.1.2 Comparison of Aggregation and Cleavage Efficiency 91
4.4 GFP Expression and Purification 96
4.5 Conclusions 98
Chapter 5: Probing Conformational Fluctuations in Beta 2-microglobulin Using Single-Molecule FRET and FCS 99
5.1 Introduction 99
5.2 Experimental Section 110
5.2.1 Protein Purification and Labeling 111
5.2.2 Single-molecule FRET and FCS 112
5.2.2.1 Single-molecule FRET (sm-FRET) 112
5.2.2.2 FCS-FRET 115
5.3 Results and Discussion 116
5.3.1 Visualization of Amyloid Fibrils by GFP Using Confocal Fluorescence Microscopy 116
5.3.2 smFRET 118
5.3.3 FRET-fluctuation Spectroscopy Indicates Milisecond Conformational Fluctuations in β_2M Mutants 123
5.3.3.1 Control Experiments for Validation of FCS-FRET 127
5.4 Conclusions 128

Chapter 6: Conclusions and Future Work 130
6.1 Conclusions 130
6.2 Future Work 132
6.2.1 Improving the Biocompatibility of the BSA Hydrogels 132
6.2.2 Testing FCS-FRET on Other Amyloid-forming Proteins 134
6.2.3 Themodynamic/Kinetic Modeling 136
Appendices 137
Bibliography 138

List of Tables

Table 1. Fitting parameters in the diffusion-limited aggregation law, with $df = 3$……52

Table 4.1 List of synthesized oligonucleotides (primers) for the construction of 6xHis-SUMO_B2M used in this study……...……91

Table 4.2. List of synthesized oligonucleotides (primers) for the construction of 6xHis-sf-GFP used in this study……103

Table 5.1. Decay rates associate with each $\beta_2 M$ variant……132

Table 6.1. Protein precursors associated with amyloid disease…….....144

List of Figures

Figure 1.1. Protein's sequence primary structure (top), Secondary structure alpha-helix and beta-sheets (middle), tertiary and quaternary structure (bottom)……2

Figure 1.2. The first structure of myoglobin at 6 Å resolution published by Kendrew and co-workers in 1958……...…3

Figure 1.3. A schematic energy landscape for protein folding and aggregation…….5

Figure 1.4. (a) One-dimensional cross-section from the high-dimensional energy landscape of a protein. (b) Timescale of dynamic processes in proteins……....6

Figure 1.5. Electron microscopy on $A\beta$(1-42) fibrils…….11

Figure. 1.6. Mechanisms of protein aggregation and amyloid aggregation……12

Figure 1.7. Cartoon representation of the solution structure of monomeric native wild-type $\beta_2 M$ (PDB code 2XKS) ……13

Figure 1.8. Hypothetical fluctuation of scattering intensity of larger particles and smaller particles……17

Figure 1.9. Schematic autocorrelation function of the intensity of scattered light……....19

Figure 1.10. Schematic representation of the optical setup of a DLS system……20

Figure 1.11. Excitation state in fluorescence…….21

Figure 1.12. Structure of typical fluorescent molecules……22

Figure 1.13. Jablonski energy level diagram showing the various decay paths in an excited state molecule……...23

Figure 1.14. Absorption and emission spectra of rhodamine 6G……..24

Figure 1.15. Steady-state (A) corrected fluorescence and (B) normalized fluorescence spectra……...25

Figure 1.16. The overlap in the excitation and emission spectra of donor and acceptor molecules……..26

Figure 1.17. Distance dependence of FRET efficiency…….28

Figure 1.18. Schematic of a confocal microscope setup used for the acquisition of diffusion-based smFRET data……..29

Figure 1.19. Fluorescence correlation spectroscopy (FCS) setup…….31

Figure 2.1. Apparent hydrodynamic radius of lysozyme monomers……..44

Figure 2.2. Heating protocol (a) and DLS analysis (b) and (c) demonstrating the process of aggregation and gelation in the 18 mg/mL lysozyme solution…….46

Figure 2.3. DLS analysis in the 20 mg/mL lysozyme solution gradually heated to 60 °C and kept at this temperature for 18, 42 and 90 h…….47

Figure 2.4. Wave number dependence for three scattering angles……..48

Figure 2.5. Long-term monitoring of the 18 mg/mL lysozyme solution via DLS……..49

Figure 2.6. Long-term monitoring of the 30 mg/mL lysozyme solution via DLS……..50

Figure 7. Average hydrodynamic radius of lysozyme aggregates in solutions of 18 mg/mL and 30 mg/mL samples, as a function of time…….51

Figure 2.8. DLS size distribution analysis of a 60 mg/mL lysozyme sample heated for 30 min at 80 °C to trigger aggregation and monitored for 24 days…….52

Figure 2.9. DLS distribution analysis of a 60 mg/mL lysozyme sample heated for 10 min at 80 °C to screen the effect of heating on the aggregation process……..54

Figure 2.10. SDS-PAGE gel image for Lysozyme (30 mg/mL) incubated at room temperature for three weeks prior running the gel……55

Figure 2.11. Fraction of unfolded lysozyme as a function of temperature……..57

Figure 3.1. Formation of transient protein hydrogels using a redox cycle…….70

Figure 3.2. Measuring protein hydrogel lifetime using DLS and protein aggregate tracers……...72

Figure 3.3. Time-dependent viscoelastic behavior of BSA hydrogels……...74

Figure 3.4. BSA unfolding increases the solvent accessible cysteine group concentration and the disulfide crosslinking density……...77

Figure 3.5. Fluorescence imaging and spectroscopy measurements of the redox environment in the transient hydrogels……...79

Figure 3.6. Impact of DTT and H_2O_2 concentrations on hydrogel lifetime……81

Figure 3.7. Location of cysteine groups in hydrophobic and hydrophilic regions and the impact on dissipative assembly……..83

Figure 4.1. Plasmid map of 6xHis-TEV-B_2M…….88

Figure 4.2. PCR product for GA loaded on DNA gel……..89

Figure 4.3. (a) Schematic description of the Gibson Assembly steps……..90

Figure 4.4. Western Blot comparing the soluble and insoluble expression of β_2M……97

Figure 4.5. Sedimentation equilibrium data showing concentration gradients at three speeds for two concentrations of β_2M……100

Figure 4.6. Size exclusion chromatography and SDS-PAGE gel on $\beta_2 M$ expressed and purified without soluble partner……..101

Figure 4.7. SEC and CD measurements on purified, refolded, and cleaved $\beta_2 M$ expressed as a fusion to SUMO protein……..103

Figure 4.8. Sf-GFP plasmid map construction by GA……104

Figure 5.1. Schematic illustration of aggregation pathways……...107

Figure 5.2. Beta 2-microglobulin ($\beta_2 M$) crystal structure (PDB ID: 2d4f) with the disulfide bond marked in magenta……..109

Figure 5.3. Reaction coordinate diagrams showing fast versus slow interconversion……112

Figure 5.4. Three-dimensional illustration of the interconversion and aggregation reaction coordinates……..114

Figure 5.5. Representation of two interconverting state……116

Figure 5.6. D76N-$\beta_2 M$ SDS-PAGE gel. Multiple washing fractions of flow through of cleavage reaction show >95% purity for monomeric protein……119

Figure 5.7. Schematics of the experimental setup……121

Figure 5.8. An example time trace of the fluorescence intensities collected from the donor and acceptor channels of our system……122

Figure 5.9 GFP bind various amyloid fibrils……..124

Figure 5.10. GFP binds $\beta_2 M$ amyloid fibrils……125

Figure 5.11. Cartoon representation of $WT - \beta_2 M$ structure with cysteine mutants added at the N and C termini shown in red and green with a separation distance of 46.6 Å. (PDB ID: 2d4f)……127

Figure 5. 12. sm-FRET histograms extracted from $\beta_2 M$ variants in native conditions, labeled with Alexa488/Alexa594 at both terminals……128

Figure 5.13. The Gaussian approximation (full curves) tested against exact FRET efficiency histograms (bars) for two conformational states with FRET efficiencies = 0.4 and = 0.8….129

Figure 5.14. Correlation analysis demonstrating distinct FRET-fluctuation patterns for different $\beta_2 M$ variants…….132

Figure 5.15. (a) denaturing conditions (pink curve). (b) A mixture of donor and acceptor covalently attached on separate β_2M molecules (green curve). (c) Donor-only labeled β_2M (brown curve)……..135

List of Abbreviations

6xHis	6x-Histidine tag
A488	Alexa Fluor 488
A594	Alexa Fluor 594
ALS	amyotrophic lateral sclerosis
ANS	8-Anilononaphthalene-1-sulfonic acid
ATP	adenosine triphosphate
AUC	analytical ultracentrifugation
b	the baseline (accidental) correlation level
BSA	bovine serum albumin
CCD	charged-coupled device
CD	circular dichroism
D	diffusion coefficient
DLS	dynamic light scattering
DRA	dialysis-related amyloidosis
DTNB	5,5-dithio-bis-(2-nitrobenzoic acid
DTT	dithiothreitol
E	FRET transfer efficiency
E. coli	Escherichia Coli
EDTA	ethylenediaminetetraacetic acid
FCS	fluorescence Correlation Spectroscopy
FLCS	fluorescence lifetime correlation spectroscopy
FPs	fluorescent proteins
FRET	Förster Resonance Energy Transfer
G	Gibbs free energy
GA	Gibson Assembly
H202	hydrogen peroxide
HDX-ESI-MS	hydrogen/deuterium exchange electrospray ionization mass spectrometry
HPLC	high performance liquid chromatography
IA	acceptor intensity
ID	donor intensity
IMAC	by immobilized metal affinity chromatography
IPTG	isopropyl β-D-1-thiogalactopyranoside
IT	folding intermediate
K	equilibrium constant
K_b	Boltzmann's constant
kDa	kilodalton
MHC I	major histocompatibility complex class 1
M_w	molecular weight
NaOH	sodium hydroxide
NEB	New England Biolabs
NEM	n-ethylmaleimide
NGO	non-genetic origin

Ni-NTA	nickel (II) nitriloacetate
OD	optical density
PBS	phosphate-buffered saline
PMT	photomultiplier detector
R	inter-dye distance
R_0	the Förster distance
RAM	replica-averaged metadynamics
RASA	relative solvent accessible surface area
R_h	hydrodynamic radius
RMSD	root-mean-square-deviation
RPM	round per minute
SDS-PAGE	sodium dodecyl sulfate–polyacrylamide gel electrophoresis
SEC	size exclusion chromatography
sf-GFP	super folder green fluorescence protein
smFRET	single-molecule FRET
SUMO	small ubiquitin-related modifier
t	time
TCEP	tris(2-carboxyethyl) phosphine
TEM	transmission electron microscopes
ThT	thioflavin T
tnb	2-nitro-5thiobenzonate
UV-Vis	ultraviolet-visible
WT	wild type
Z_0	latera radius
β2M	beta 2-microglobulin
λ	the laser wavelength
ω_0	axial radius
Θ	scattering angle
τ	lag time between two time points
τ_c	decay time
Γ	decay rate
n	refractive index
κ	the eccentricity

Chapter 1. Introduction

1.1 Protein Folding, Conformational Energy Landscape and Aggregation

1.1.1 Protein Folding and Energy Landscape

Proteins make up more than 50 percent of cells' dry weight and have prominent roles in essential processes in living organisms. The protein building blocks are a set of 20 amino acids, organic molecules with carboxyl and amino groups[1]. Proteins provide structural support, substance transport, signaling, and defense. Enzymes participate in biochemical reactions in cells. In mammalian cells, ribosomes synthesize more than 10,000 types of proteins[2]. These diverse and vital microscopic molecules play essential functions in mammals, including tissue repair, gene regulation and protections[3].

Some proteins provide structure and stiffness to the cells[4]. Some play the role of a shuttle for molecules in the cells[5], and some catalyze intracellular reactions[6]. In order to perform all of those specific and broad functions, proteins must assume three-dimensional folded structures by transitioning from a linear chain of amino acids into a globular compact form through a complex folding process[7]. Protein folding is an essential, ubiquitous instance of self-assembly in biology, during which the one-dimensional synthesized peptide chain self-assembles into its biologically active conformation[8,9]. How a protein chain folds upon itself depends on the sequence of its amino-acid building blocks (primary structure). Figure 1.1 illustrates α-helices and beta sheets, the two structures that form initially called the protein's secondary structure.

When an amino acid's backbone C ─ H group hydrogen bonds to the C ═ O group on another amino acid's backbone located four units far from the first amino acid, a right-hand helix conformation forms, which is the α-helix. Beta-sheets are zigzag patterns that make a typical structural pattern of a protein's secondary structure. Beta strands, 3-10 amino-acid long, connect through backbone hydrogen bonds to form the beta-sheets[10,11].

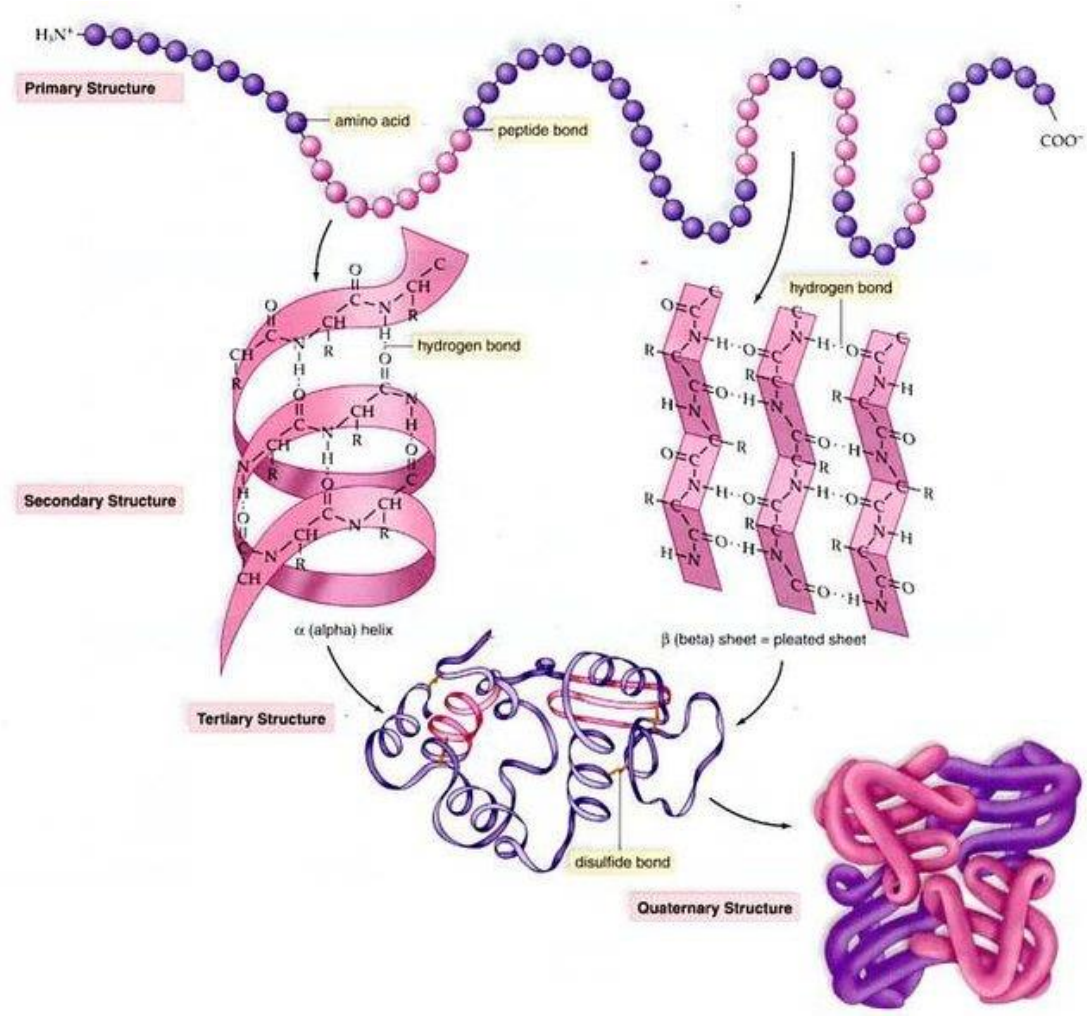

Figure 1.1. Protein's sequence primary structure (top), Secondary structure alpha-helix and beta-sheets (middle), tertiary and quaternary structure (bottom). Figure reproduced with permission from [12].

The three-dimensional form of a protein is called the tertiary structure. The tertiary structure may contain one or more secondary structure domains. The interactions within the amino acids' backbone and side chain bonds support the tertiary structure. The thermodynamic and kinetic constraints for protein folding are a relatively stable unique folded conformation with a minimized Gibbs free energy in physiological conditions and reaching that stable fold within a reasonable time[13]. These interactions include polar hydrogen bonds and ionic interactions from outside and the hydrophobic interactions between non-polar amino acids from inside. Disulfide bonds, which covalently link the sulfur-containing cysteine's side chains, are the only covalent bond stabilizing a protein's tertiary structure by firmly attaching parts of the polypeptide chain. Quaternary structure is the fourth classification for structural levels of proteins and happens two or more chains or subunits of proteins form a higher order molecular complex[14]. Hemoglobin and DNA polymerase are two examples of proteins with quaternary structure[15]. Figure 1.2 shows the first experimentally measured structure of a globular protein, myoglobulin.

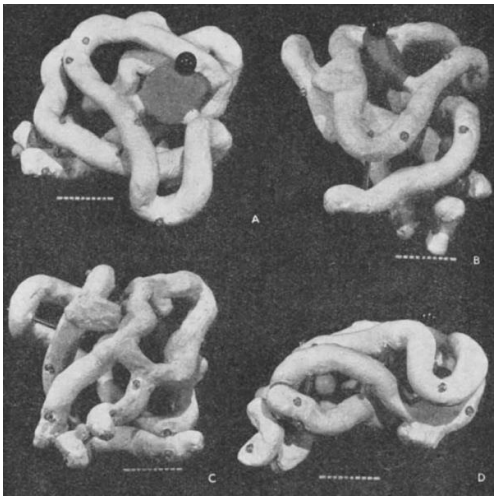

Figure 1.2. The first structure of myoglobin at 6 Å resolution published by Kendrew and co-workers in 1958. Figure reproduced with permission from reference[7,16].

From the physics point of view, proteins are soft materials that possess an average structure with each individual protein in an ensemble assuming a specific confirmation at each point in time, each with some variation from the average determined by statistics. The folding, structure, and structural variability can be described by considering the energy landscape of a single protein. This energy landscape defines thermodynamics, approximate probabilities of conformational states, kinetics, and the energy barrier height between those conformational states[17]. Not all the proteins share similar structural flexibilities; The measure of average distance between the backbone atoms of superimposed proteins, which is defined as root-mean-square-deviation (RMSD), and other parameters show different measures of structural variabilities in proteins[18]. The free energy barrier height defines the rate of the conformational exchange between different substates of proteins. The larger the RMSD, the higher the free energy barrier[19]. Since 1970, with the emergence of theoretical, experimental[20,21], and molecular dynamics simulations[22], multiple populated protein configurations substates have been noticed in addition to the three-dimensional structures identified by x-ray crystallography[23,24]. The presence of folding substates can be explained by the fact that proteins are not completely thermodynamically stable because they require conformational flexibility to function[2].

The energy landscape concept was applied to folded proteins more than 45 years ago[25]. In the complex and diverse concept of protein folding, initial random forces,[26] and hydrophobic interactions[2], play a crucial role in limiting the number of

possible conformations for the burial of nonpolar amino acids. Generally, there are multiple partially folded intermediates[27] in the funnel-like landscape[28] of protein folding (Figure 1.3) prior to the protein assuming the native folded state, which is the global free energy minimum[29]. During the folding process kinetic barriers, shown as roughness on the free-energy surface (Figure 1.3), can lead to formation of kinetically trapped partially folded intermediates[30,31]. The partially folded species expose the hydrophobic regions to the surface; hence at higher protein concentrations, the tendency for aggregation increases[32].

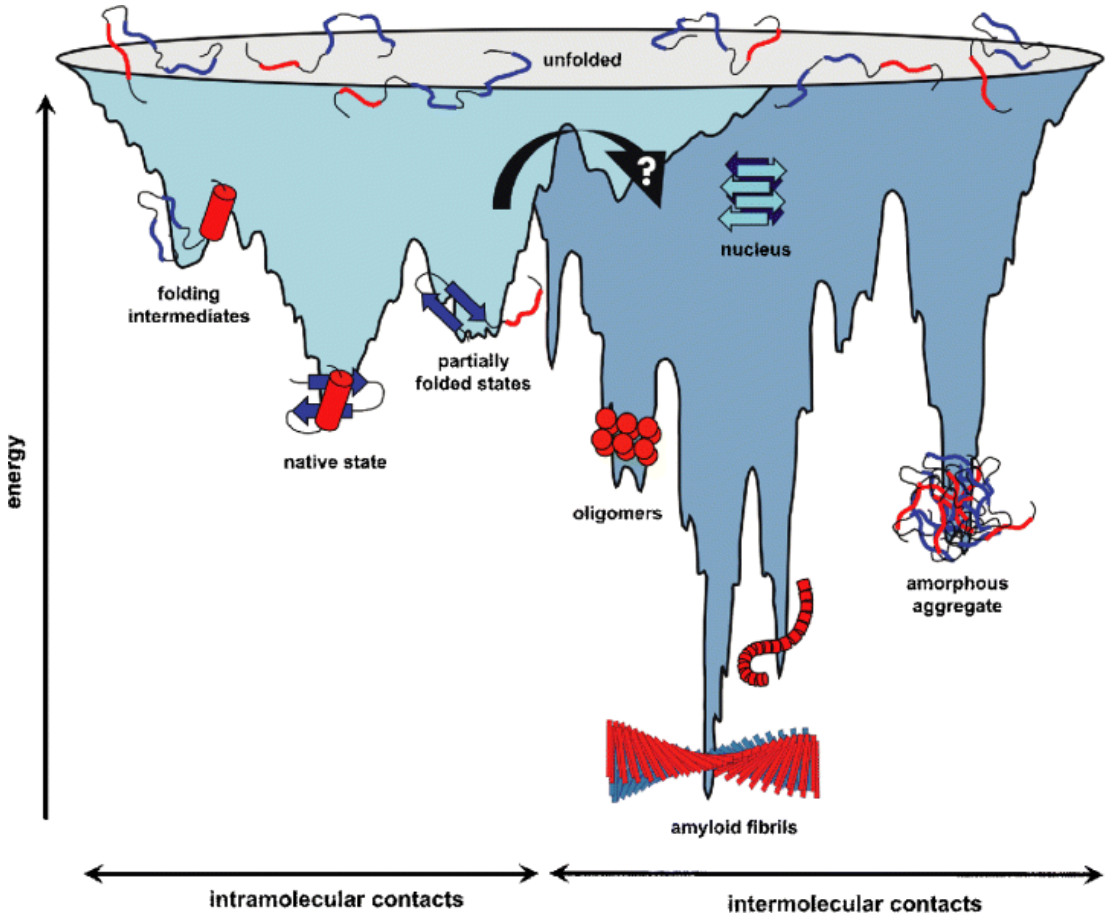

Figure 1.3. A schematic energy landscape for protein folding and aggregation. The surface shows the multitude of conformations 'funneling' towards the native state via intramolecular

contact formation or towards the formation of amyloid fibrils via intermolecular contacts. Figure and caption reproduced with permission from reference[33].

The initial features of the energy landscape, like the height of the energy barrier and the coexistence of multiple conformational substates, were characterized by Frauenfelder and colleagues by connecting the concept of energy landscape to the function of the model protein myoglobin[34]. Various characteristics of protein energy landscapes have been elucidated through the advancement of experimental and computational techniques[17].

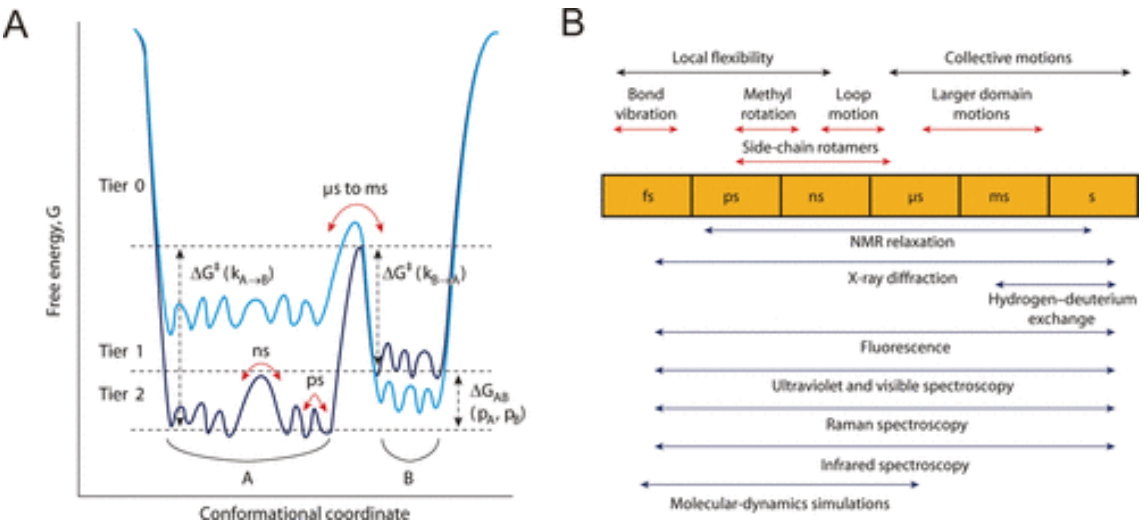

Figure 1.4. (a) One-dimensional cross-section from the high-dimensional energy landscape of a protein showing the hierarchy of protein dynamics and the energy barriers. Each tier is classified following the description introduced by Frauenfelder and co-workers. Each minimum in the energy surface represents a state. The maximum between walls corresponds to a transition state. The height of energy barrier between states (ΔG) which is the difference between their free energies, tells us about the rate of interconversion between states. Tier-0 which has two major states, A and B, includes many interconverting substates with faster fluctuations. The dark and light blue each represents energy landscape with a shift in the energy

of major states (the order of magnitude is multiples of k_BT. This shift can be a result of changes in the environment or ligand binding. (b) Timescale of dynamic processes in proteins and the experimental methods that can detect fluctuations on each timescale. Figure and caption reproduced with permission from reference [17].

As shown in Figure 1.4, protein conformational dynamics can either have slow or fast timescales depending on the length scale of the conformational change and the associated energy barrier. Interconversion between two distinct conformation states of a protein, such as ACBP[27], are typically separated by an energy barrier several times larger than that of the thermal energy of the system, which is Boltmann's constant (k_B) times the temperature, k_BT. The timescale of the interconversion between these states is on order of microseconds to milliseconds, depending on the height of the energy barrier. Smaller scale fluctuations, such as interconversion of single individual domains (*e.g.*, beta sheets) or individual amino acids within a protein, occur on faster time scales, ranging from nano- to picoseconds, due to the smaller energy barrier[17].

It is experimentally challenging to watch the movements of protein atoms to understand the protein dynamics[17]. The conformational dynamics within the native state of proteins were first revealed by hydrogen-deuterium exchange mass spectrometry, which was the first methodology showing fluctuations within the chain motion of proteins under native conditions.[35] For instance, it has been shown that peptidyl-prolyl bond isomerization for some proteins is the driving force for the presence of substates in native conditions[36,37]. In the case of Beta 2-microglobulin, the cis-trans isomerization of proline 32 has been shown to be responsible for the presence of multiple native intermediate states[38,39].

1.1.2 Protein Aggregation and Amyloid Formation

1.1.2.1 Importance of Protein Aggregation

As shown in Figure 1.3, protein aggregation can lead to a further decrease in the free energy of the system under the correct environmental conditions. Similar intermolecular forces that drive protein folding can also drive protein aggregation, such as hydrophobic interactions that lead to attractive protein-protein interactions. Protein aggregation is involved in the pathogenesis of numerous mammalian diseases[40–42]. Likewise, protein aggregation represents a major degradation pathway of biopharmaceuticals and limits the shelf life and storage conditions of protein based therapeutics[43]. Aggregation phenomena in protein formulations is generally undesirable because it alters the original properties of the solution. Both reversible self-association and irreversible aggregation contribute negatively to protein therapeutics. First, highly concentrated proteins have a propensity to form aggregates, which negatively impacts therapeutic effectiveness and quality of therapeutics, negatively impacting patients' health[44,45]. Large numbers of aggregates or formation of interlinked networks increases the viscosity of therapeutics, which is undesirable for manufacturing and administration to patients[45]. While aggregation can reduce or even annihilate the biological activity of proteins[46], even in presence of bioactivity, the immune response of a protein-based drug has been shown to be exacerbated due to the existence of protein aggregates[47–50]. The existing aggregates can be either soluble or insoluble[51]. The reversible aggregates with a low molecular weight (oligomers) are in the category of soluble aggregates. Usually, a small percentage of unavoidable soluble aggregates exist in biotherapeutic solutions (5 – 10%) without imposing negative risk

factors[52,53]. When the solubility limit of a protein formulation is reached, the previously soluble aggregates precipitate in the form of insoluble aggregates[52].

1.1.2.2 Protein Aggregation *in vivo*

Misfolding and aggregation of proteins is involved in the pathogenesis of many neurodegenerative diseases[54–57]. Alzheimer's disease, Parkinson's disease, Huntington's disease, amyotrophic lateral sclerosis (ALS), and transmissible spongiform encephalopathies are examples of diseases caused by protein aggregation. While some of these diseases have a genetic origin (Huntington), and some have a non-genetic origin (ALS), protein aggregation is observed in all of these diseases' pathologies[58].

A complicated network of processes controlling proper protein folding and degradation is utilized to maintain a healthy cellular environment[59]. This complicated network is called “protein homeostasis,” or proteostasis, and its actions ensure the presence of proteins in their proper concentrations and conformations[60]. Proteostasis empowers cell differentiation for organ development and preventing diseases by affecting cellular functions[61]. Under certain diseases states, misfolded conformers of disease-causing proteins accumulate within cells despite the presence of folding chaperons and proteasomes[62]. Even though the proteostasis system precisely controls the conformation of all proteins, in the case of aggregate-prone disease-causing proteins, aging can increase their tendency for aggregation and eventually overcomes the ability of the proteostasis network to degrade misfolded proteins, leading to cellular dysfunction[63,64].

1.1.2.3 Amyloid Fibrils

Amyloid fibrils are unbranched cross-Beta-sheet structured aggregates of proteins (Figure 1.5). These aggregates have an affinity to aromatic dyes such as thioflavin T (ThT) and Congo red[65]. The amyloid state is a universal and highly stable configuration of protein chains in which many proteins with different original native folds can acquire that cross-B structure[66]. Usually, the building blocks of these extended assemblies are similar proteins or peptides, and fibrils are made of two twisted proto filaments lined up in a helical symmetry with two folds. The fibrils' cross-Beta-sheet segments are parallel to each other and perpendicular to the fibril's axis[67].

Hydrogen bonding between backbone amide functional groups of segments of different proteins drives them into an amyloid state. The backbone amide groups must first be exposed for hydrogen bonding to occur. Partial denaturation[68], formation of inclusion bodies by overexpression[69], peptide cleavage, and high concentrations of intrinsically disordered proteins are some of the causes for backbone amide group exposure. In all these conditions, the concentrations of proteins should be sufficiently high for the nucleation of amyloid formation to happen[61,70,71].

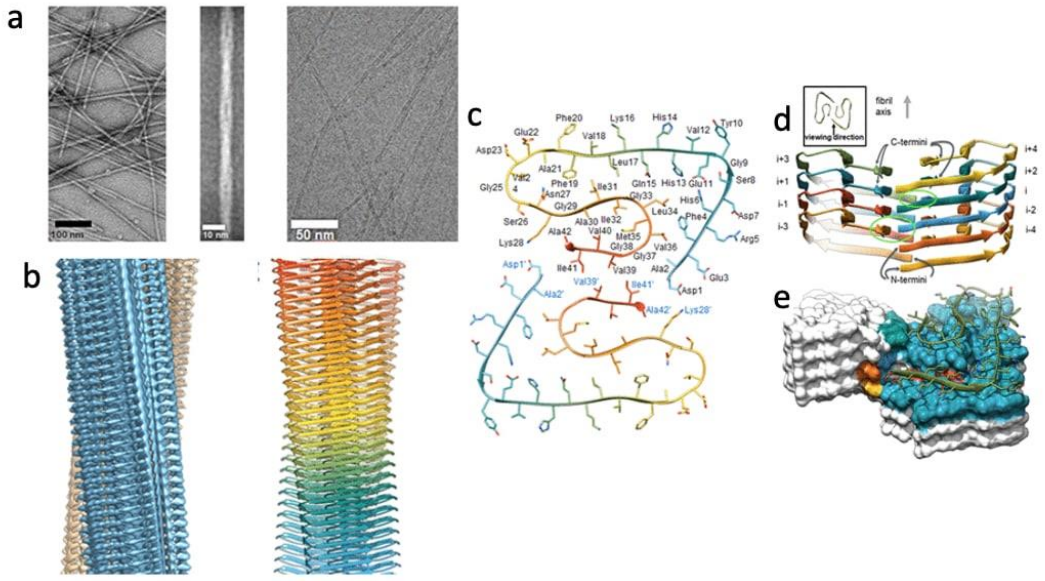

Figure 1.5. Electron microscopy on *A*β(1-42) fibrils. (a) Twisted fibrils shown in a high contrast negative stain TEM image (first image), a close-up of the twisted fibril (second image), and the cryo-EM image of fibrils (third). (b) density map and the cartoon representation of the atomic fibril model. (c) Two symmetric proto filaments from a cross-section view. (d, e) Side view of cartoon and sphere atomic models. Figure and caption reproduced with permission from reference[67].

1.1.2.4 Early Stages of Amyloid Formation

Amyloid aggregate formation occurs by nucleation of seeds followed by polymerization (Figure 1.6)[65]. Like how it is illustrated in Figure 1.6(a) light-bule part, and 1.6(b) white part, a substantial step in the development of amyloid structures is the formation of pre-amyloid soluble oligomers[72]. Amyloidogenesis and protein folding share similar driving forces, such as hydrogen bonding and hydrophobic effect[65]. Because in these pre-amyloid oligomers (Figure 1.6 a,b), the accessible sticky hydrophobic patches are exposed to the surface, they are thought to be highly toxic for the cells by disturbing the cellular functions[65]. These few unstable pre-amyloid

oligomers play the role of a nucleus in such nucleation-dependents polymerization. Upon the formation of cross-Beta amyloids, these sticky patches and peptide backbones bury in the stable cross-beta structures[73]. The dynamic process of *in vivo* protein aggregation consists of many components[65]. Several mechanisms for amyloid aggregation have been proposed over the past couple of years (Figure 1.6)[74–80]. Nucleation is common among all the identified mechanisms for amyloid aggregate formation[65,78,79]. In contrast to the mechanism in Figure 1.6a, in which the nucleation is the rate-limiting step, in Figure 1.6b, the lower free energy of oligomers speeds up their formation, and the conformational conversion of its monomeric building blocks to the unstable nucleus is the rate-limiting step.

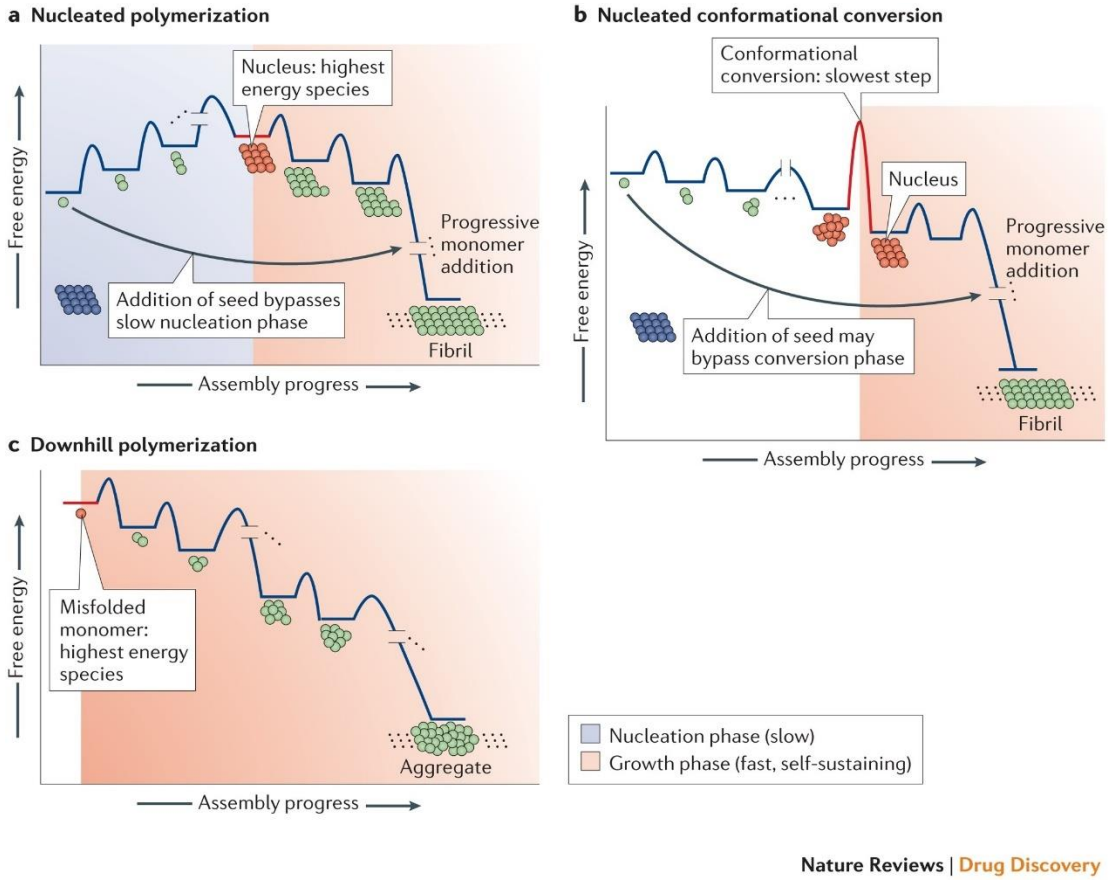

Figure. 1.6. Mechanisms of protein aggregation and amyloid aggregation. (a) A nucleation step is required for the initiation of aggregation. The nucleus is a rare species that is comprised of partially folded monomers. Monomers are rapidly added to the nucleus after its formation. These partially folded oligomers are less stable than fully folded monomers. (b) In this proposed mechanism, the monomers and oligomers with heterogenous structures are in equilibrium, with oligomers in a more stable energy state. Oligomers convert to the nucleus in a time-dependent manner. (c) oligomerization starts with misfolded monomers. The rate-limiting step here is the formation of misfolded monomers from natively folded protein. Figure and caption reproduced with permission from reference[65].

1.1.3 Beta 2-microglobulin

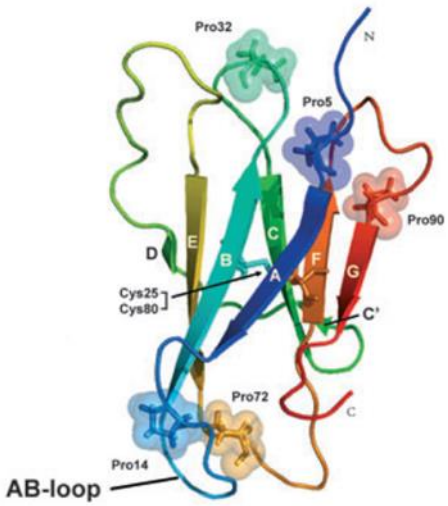

Figure 1.7. Cartoon representation of the solution structure of monomeric native wild-type $\beta_2 M$ (PDB code 2XKS showing β-strands A (amino acids 6–11), B (21–28), C (36–41), C (44–45), D (50–51), E (64–70), F (79–83) and G (91–94). Highlighted are the residues Pro 5, Pro14, Pro 32, Pro 72 and Pro 90 (in sticks, spheres) and the disulfide bond between residues Cys 25

and Cys 80 (in sticks). N, N-terminus; C, C-terminus. Figure and caption is reproduced with permission from reference[81].

β_2M is the light chain of the major histocompatibility complex class 1 (MHC I)[82]. β_2M is a 99-amino acid protein with a beta-sandwich fold in which there are seven antiparallel β-strands, stabilized by a single disulfide bridge[81,83]. Upon dissociation from MHC I, β_2M would be released in the blood to be further degraded by kidneys[84,85]. In patients with kidney failure, β_2M concentrations in the blood increase[86]. DRA fibrils usually deposit in the dialysis patients' joints, causing conditions like bone cysts, carpal tunnel syndrome, joint arthropathy, and other problems[87,88]. The thermodynamically unfavorable trans-isomerization of Pro32 residue has been thought to be a driving force for its tendency for amyloid formation[32]. Some studies mention that another possible trigger for amyloid formation could be the microsecond to millisecond dynamic conformational fluctuations in the D-strand and the DE-loop in the structure of β_2M[89]. Previous hydrogen/deuterium exchange electrospray ionization mass spectrometry (HDX-ESI-MS) studies have revealed that β_2M upon release from MHC I complex acquires a flexible and dynamic structure compared to its bound state due to higher solvent accessibility and weaker packing forces within β_2M's structure in its unbound isolated form[90,91]. Native β_2M is resistant to amyloid formation in vitro; it is unclear which factors stimulate the formation of amyloid-forming folding intermediates[85]. It is proposed that a probable culprit for aggregation of β_2M is a folding intermediate (IT) with an overall structure close to the native state. A prolyl-peptide bond with a non-native trans conformation is the crucial difference between IT and native β_2M[92,93]. The formation of IT, which is driven by the fluctuation in the structure, is a required step

before aggregation. Such fluctuations cause the exposure of hydrophobic sequences, which are usually buried in a native state[94–96].

Researchers conducted extensive studies on the $\beta_2 M$ amyloid formation mechanism. Studies include the role of extracellular matrix components (collagen, low molecular weight collagen, and polipoprotein E), induction of fibril formation by seeds, effects of pH[32,97], physiological factors[85], point mutation dependent conformational stability[98], fibrillar structure studies[99], Cu-induced amyloid formation, and the role of small molecules in inhabitation of fibril formation[100]. Techniques such as mass spectroscopy, NMR, Cryo-EM, and TEM have widely been used for obtaining high-resolution structural information of the amyloid fibrils even at an atomic resolution[67,99]. Molecular dynamic simulations have been used in studies of conformational dynamics and solving the intermediate states of $\beta_2 M$, enhancing the protein-protein interactions and aggregation[96,101].

There are still numerous unknowns about the structure and dynamics of amyloidogenic intermediates[102]. Studies on the structure of a few oligomeric protein assemblies have shown high β-sheet content in some of them and a heterogeneous structure. So far, more information about these oligomeric species has not been obtained[67]. Little is known about the nucleation mechanism for amyloid formation, i.e., how thermodynamically stable proteins in solution become unstable and form nuclei. Nucleation is often the rate-limiting step for protein aggregation, significantly impacting the timeline of disease progression in various neurological diseases involving protein aggregation.

1.2 Dynamic Light Scattering (DLS)

Here we review the fundamental principles of DLS, which is utilized to characterize protein aggregation and protein hydrogel formation. We describe the instrument setup, fundamental underlying scattering physics, thermodynamics of scattering methods, and the information provided by the technique.

1.2.1 Basics of Light Scattering

In a quiescent fluid solution, the thermal motion of solvent molecules leads to their random collision with dissolved solute molecules or colloids, which causes random displacement. This process, known as Brownian motion, can be embodied by a balance between thermal and viscous forces on the solute molecules *via* the Stokes-Einstein equation for the self-diffusion coefficient (D). Assuming spherical non-interacting particles the hydrodynamic radius, R_h, is related to the self-diffusion coefficient by Stokes-Einstein equation[103]:

$$R_h = \frac{\mathrm{k}_B T}{6\pi\eta D} \tag{1.1}$$

Where, k_B is Boltzmann's constant, T is the temperature, and η is the kinematic viscosity of the solvent.

As evidenced in equation (1.1), a characteristic of Brownian motion is that small molecules move faster than large ones due to decreased viscous hindrance.

A small fraction of light is scattered from a molecular or colloidal solution when it is irradiated with visible monochromatic light of high spatial and temporal coherence.

The intensity of this scattered light fluctuates in a time-dependent manner due to the continuously changing distances between particles, which leads either to constructive or destructive interference. DLS takes advantage of the particle size dependence of the scattered light fluctuations to gain information pertaining to size of particles. As discussed above, large particles diffuse slowly due to large viscous hinderance and thus cause less rapid fluctuations in the scattered light intensity, compared to small fast moving particles[104] (Figure 1.8).

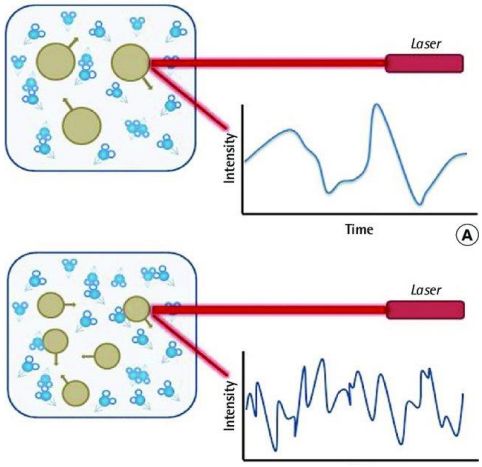

Figure 1.8. Hypothetical fluctuation of scattering intensity of larger particles and smaller particles. Figure and capture reproduced with permission from reference[105].

The autocorrelation function of the scattered-light intensity can be used to obtain the particle diffusion coefficient and size by correlating the intensity fluctuations of scattered light with respect to time. A digital autocorrelator is used to extract the correlations in intensity fluctuations related to the diffusion behavior of colloidal particles. The autocorrelation function, $G_2(\tau)$, is defined using a comparison of the intensity $I(t)$ of the scattered light at a time t with that at some later time $(t + \tau)$:[106,107],

$$G_2(\tau) = \langle I(t)I(t+\tau)\rangle, \tag{1.2}$$

where τ is the lag time between two time points. The normalized autocorrelation function can be written as:

$$g_2(\tau) = \frac{\langle I(t)I(t+\tau)\rangle}{\langle I(t)\rangle^2}. \tag{1.3}$$

The braces in equations 1.2 and 1.3 denote averaging of properties over time. For the simplest case of spherical monodisperse particles in a fluid, the autocorrelation function has a single characteristic decay time τ_c.

$$g_2(\tau) = 1 + e^{-2\Gamma\tau}, \tag{1.4}$$

The decay rate, Γ, is proportional to the diffusion coefficient of the particles and is the inverse of the decay time, τ_c, where

$$\Gamma = Dq^2. \tag{1.5}$$

Here $q = \left(\frac{4\pi n}{\lambda}\right)\left(\frac{\theta}{2}\right)$ is the wave vector, n is refractive index, λ is the laser wavelength, and θ is the scattering angle[108]. For spherical particles or solutes, the corresponding particle size can be determined by converting the diffusion coefficient to hydrodynamic radius using equation 1.1 and the known solution viscosity.

In our experiments, the heterodyne technique (which employs dual frequencies) is used, which is suitable for small intensities. Equation (1.5) relating the decay rate *Γ* to diffusion coefficient *D* is applicable for heterodyne experiments. Homodyne measurement is another technique that extracts information of the frequency of an

oscillating signal by comparing that signal with a standard oscillation, and is suitable for large intensities (e.g., near critical point of a fluid or for colloid systems). For homodyne spectrum, the relation between Γ and D is:

$$\Gamma = 2Dq^2 \tag{1.6}$$

The autocorrelation function $g_2(\tau)$ of the scattered light as a function of the decay time τ_c can be represented by[109]:

$$g_2(\tau) = b[1 + \varepsilon \exp\left(-\frac{\tau}{\tau_c}\right)] \tag{1.7}$$

Where $\frac{\tau}{\tau_c}$ is equal to $2Dq^2\tau$.

The baseline (accidental) correlation level b is proportional to the total scattered light intensity (I). Figure 1.9 shows a schematic of the correlation function. The coefficient ε depends on the amount of stray light and the apertures in the system and is an instrument dependent parameter.

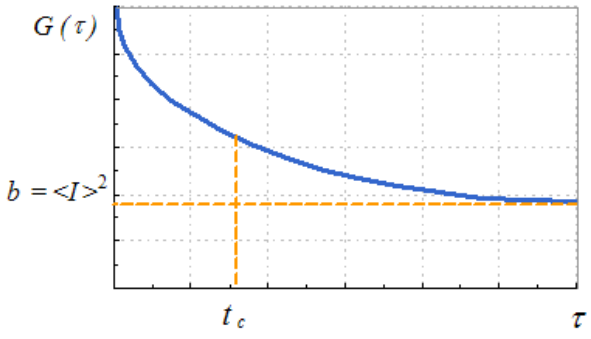

Figure 1.9. Schematic autocorrelation function of the intensity of scattered light. Figure and caption reproduced with permission from reference[110].

1.2.2. Light scattering instrument

A DLS instrument is composed of a laser light source, a sample cell, a detector placed at a fixed or variable angle, a photomultiplier amplifying the signal, and a correlator (Figure 1.10). A multi-angle dynamic and static light scattering instrument is used for the experiments in this thesis (Photocore Complex). The laser source is a thermo-electric cooler (TEC) stabilized diode laser 650 nm with 30 mW of power. The scattering angle was fixed at $\theta = 30^{\circ}$ and the duration of the measurement is 1 hour for each sample (120 repetitions of 30 second frames).

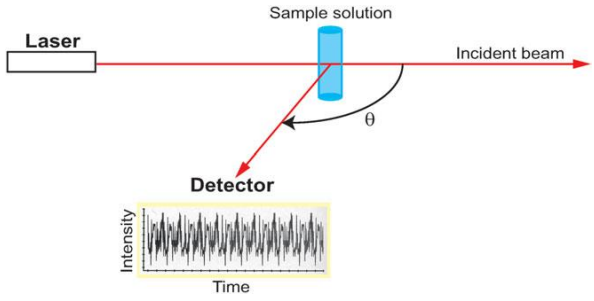

Figure 1.10. Schematic representation of the optical setup of a DLS system.

1.3 Fluorescence Techniques

1.3.1 Fluorescence Spectroscopy

Fluorescence spectroscopy is utilized to measure the response of a molecule to excitation by light at a specific wavelength[111]. This highly sensitive technique is vital for probing biomolecular structure, function, and biochemical reactions. Some example applications of fluorescence spectroscopy include medical diagnostic, DNA sequencing, and flow cytometry[112].

Fluorescence is a subset of the luminescence mechanism, during which light is emitted from the excited state of an electron. The electronic excited state can be created by absorbing light or chemical mechanisms. Fluorescence and phosphorescence are two categories of the photoluminescence phenomena, which are defined by the generation of luminescence after the excitation of a molecule by ultraviolet or visible light[113]. The fluorescent molecule absorbs light at a specific wavelength and emits light with a longer wavelength. The time interval between the excitation of an electron and going back to its ground state is called the fluorescence lifetime, which is around 10 ns for most molecules[112]. Figure 1.11 presents a simple illustration of a molecule excited by the external light (A), and how its electron travels from the ground state to the excited state (B).

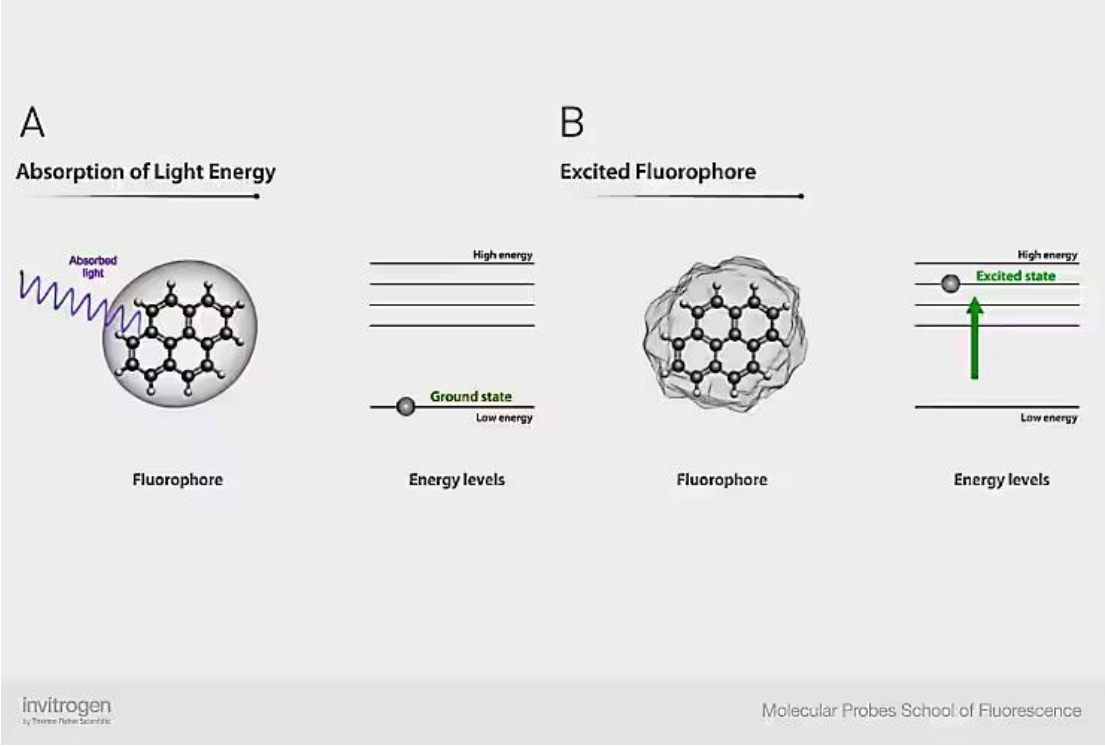

Figure 1.11. Excitation state in fluorescence. (A) Light emitted from an external source is absorbed by the molecule, which reaches an excited state (B). Figure and caption reproduced with permission from reference [114].

Most aromatic molecules are fluorescent where the excitation of delocalized electrons in the aromatic rings gives the aromatic molecules fluorescent properties[115]. Some typical fluorescent molecules are shown in figure 1.12.

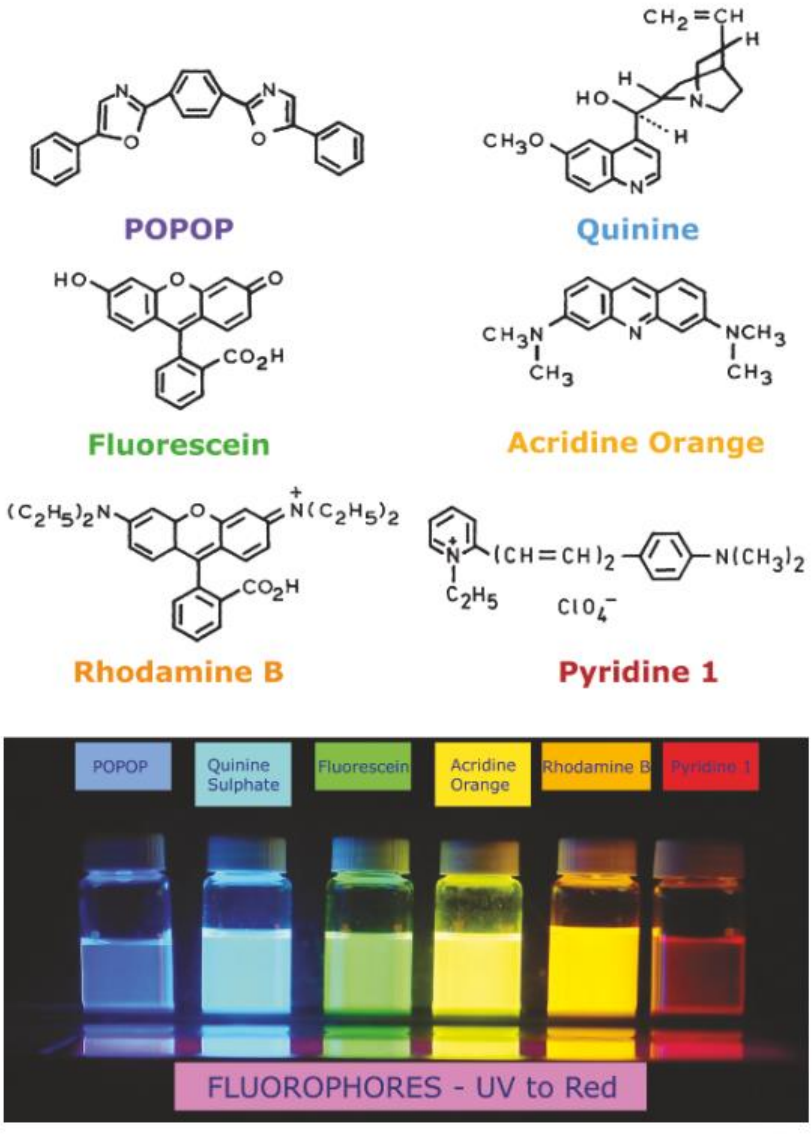

Figure 1.12. Structure of typical fluorescent molecules[112].

Professor Alexander Jablonski, the father of fluorescence spectroscopy, developed the Jablonski diagram, (Figure 1.13) which describes the electronic processes occurring in a molecule during the absorption and emission of light[116]. According to the Jablonski diagram, once a fluorophore is in the excited state, many processes can happen, each of which has a unique rate[117]. One example of these processes is a non-radiative transition which is particularly important in this work for being the basic phenomenon happening in the primary technique we used in this work, fluorescence resonance energy transfer. This non-radiative process transfers energy between a luminescent donor and a chromophoric acceptor. The donor and acceptor pair participating in this process can be organic dyes, fluorescent proteins, or nanoparticles in proximity of 1 – 10 nm from each other[118].

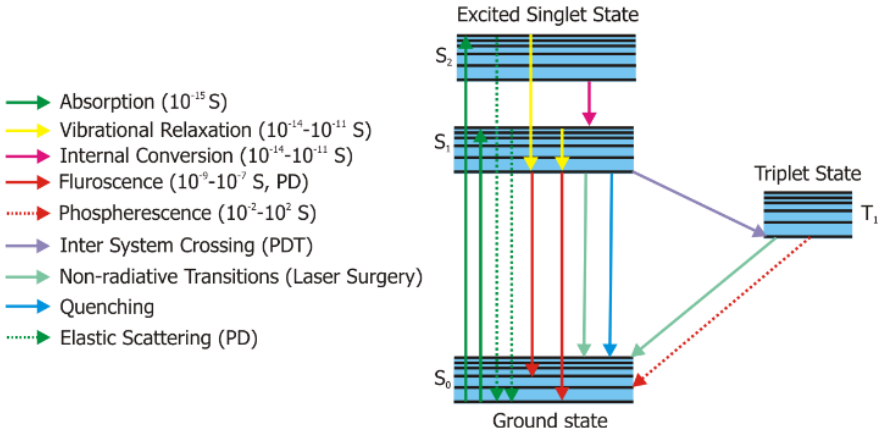

Figure 1.13. Jablonski energy level diagram showing the various decay paths in an excited state molecule. Figure and caption reproduced with permission from[119].

Sir George G. Stokes was the first scientist who described fluorescence in 1852 and observed the lower energy (longer wavelength) of fluorescence[120]. Figure 1.14

shows a typical excitation-emission plot for a common fluorophore, rhodamine 6G. The maximum excitation wavelength of a fluorophore is the wavelength at which the highest excitation efficiency can be achieved. A fluorophore can also be excited in wavelengths near the excitation maximum with a lower excitation efficiency. Similar to the excitation, the maximum output of fluorescence can be achieved is the fluorophore's emission maximum. Fluorescence at higher or lower wavelength can still be detected, but with less intensity. Since the excitation and emission processes are associated with energy loss through non-radiative electronic transitions, the emission maximum occurs at a higher wavelength of light with less energy. The difference between these two maximum wavelengths is called the Stokes shift (Figure 1.14), named after its discoverer, Sir George G. Stokes[121].

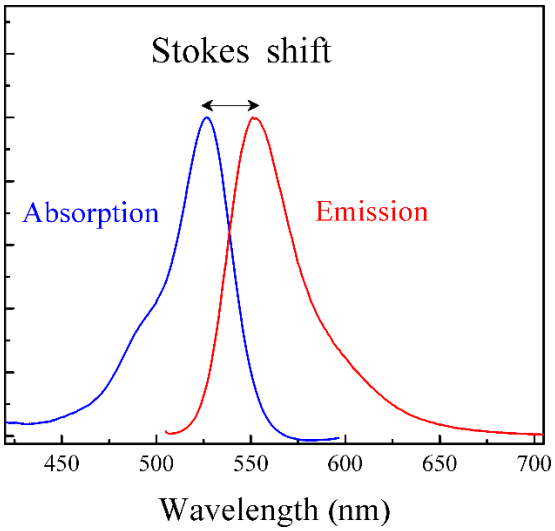

Figure 1.14. Absorption and emission spectra of rhodamine 6G. Figure is reproduced from Wikipedia[122].

Fluorophores show sensitivity to their environment due to their interaction with solvent molecules, the presence of co-solutes, temperature, and pH, which can affect their fluorescence emission intensity and maximum emission wavelength. The

advantage of fluorophore sensitivity to environment is that changes in fluorescence emission spectra can be used to probe the local environment of the fluorophore within a larger molecule, such as a protein. For example, the fluorescent properties of the aromatic amino acid tryptophan are sensitive to the polarity of the local environment. The relative polarity of tryptophan groups in a protein are therefore revealed based on the emission spectra, where the peak emission occurs at longer wavelengths upon unfolding of a protein exposing the non-polar tryptophan to water[112]. Figure 1.15 clearly shows how the height and location of the tryptophan fluorescence emission changes according to the unfolding state. As more denaturant (guanidine hydrochloride) was added to the buffer, the emission peak height decreased and red shifted due to changes in the hydrophobicity of the environment surrounding the tryptophan.

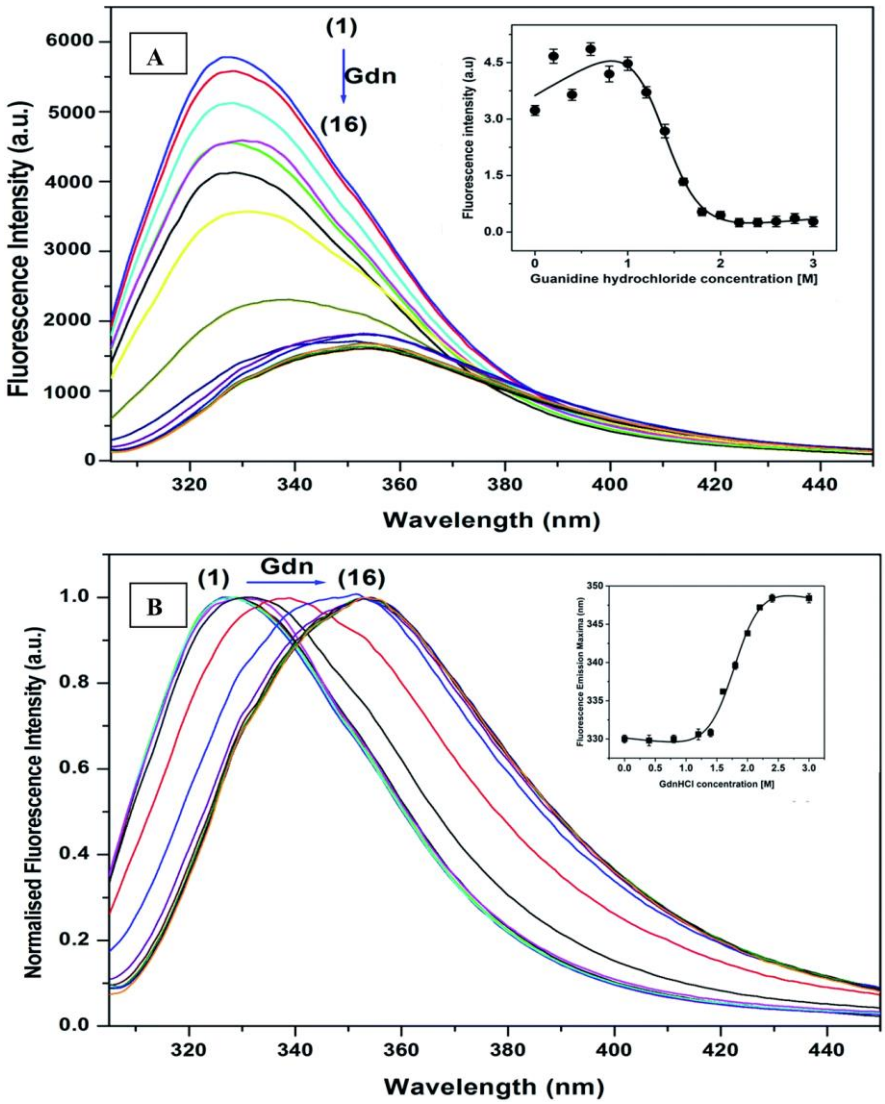

Figure 1.15. Steady-state (A) corrected fluorescence and (B) normalized fluorescence spectra of 5 μM MPT63 with varying concentrations of Gdn at 298 K. Figure and caption reproduced with permission from reference[123].

1.3.2 Fluorescence (Förster) Resonance Energy Transfer (FRET)

Fluorescence resonance energy transfer (FRET), identified in 1984 by Theodor Förster, occurs when an excited fluorescence molecule (donor) transfers an excited state electron through a non-radiative pathway to another fluorophore (acceptor)[124]. The excited electron in the acceptor molecule returns to its ground state by emitting a

photon with lower energy than the donor molecule, *i.e.*, at a longer wavelength. The emission spectra of the donor molecule and the excitation spectra of the acceptor molecule should have an overlap for FRET to occur (Figure 1.16)[125].

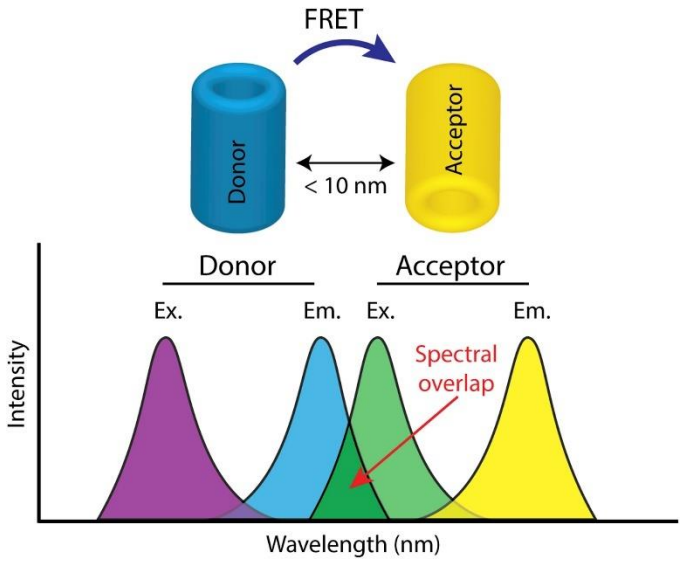

Figure 1.16. The overlap in the excitation and emission spectra of donor and acceptor molecules. The donor and acceptor molecules must be in the proximity of less than 10 nm of each other. Figure reproduced with permission from[125].

The amount of spectral overlap between donor and acceptor, the donor quantum yield, the orientation of fluorophore transition dipoles, and the spatial distance between donor and acceptor all affect the rate of energy transfer. Due to the latter impact of separation distance on donor-acceptor pair, the measurement of spatial distance between different points in biomolecules, such as proteins and DNA, has become possible due to the sensitivity of FRET efficiencies on the distances between donor and acceptor molecules. FRET can be used in research on macromolecules such as proteins and DNA and in membrane studies to measure distances in the range of 15 to 60

angstroms. Some examples of FRET applications are in studies of protein association, DNA hybridization, and binding studies[112].

The Förster distance (R_0) is defined as the acceptor to donor distance where the FRET transfer efficiency, E (Equation 1.8), drops by 50%[126]. In a single-molecule FRET experiment, the apparent E can be extracted from the donor and acceptor fluorophore intensities as:

$$E = \frac{I_A}{I_A + I_D} \tag{1.8}$$

where I_D and I_A are donor and acceptor intensities after background subtraction[127].

Therefore, the inter-dye distance can be estimated from the ratio of the acceptor fluorescence emission intensity to the sum of the donor and acceptor emission intensities[112]. Equation 1.9[112] and Figure 1.17 show how the FRET efficiency, E, change as a function of separation distance between the donor and acceptor dye:

$$E = \frac{1}{1 + \left(\frac{R}{R_0}\right)^6}, \tag{1.9}$$

where R is the inter-dye distance.

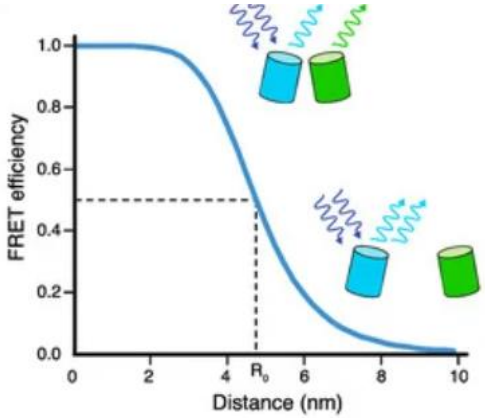

Figure 1.17. Distance dependence of FRET efficiency. Förster distance (R_0) is the separation where efficiency is 50%. Figure reproduced with permission from reference[126].

Conventional FRET utilizes a macroscopic sample and conventional fluorescence spectrometer to measure the average FRET efficiency for an entire ensemble of molecules. In an ensemble FRET measurement, the concentration of the dual-labeled molecule is ~0.1 μM. The spectrometer's light source excites the donor molecules at its excitation peak's wavelength, then records the spectra of acceptor's emission. The height of the donor and acceptor's emission peaks would be used for the calculation of FRET efficiency[128].

It is not possible to isolate heterogeneous acceptor-donor distances in a population using conventional FRET. On the other hand, single-molecule FRET (smFRET) utilizes a nanometer sized optical probe to sample the FRET efficiency of individual single molecules[112,129]. smFRET has been utilized to investigate protein and DNA folding and conformational dynamics[130,131] and recombination[132] among other subjects. smFRET uses a diffraction limited confocal laser probe, with a size on the order of 200 nm, to measure the donor and acceptor emission from a single molecule or complex and thus measure the FRET efficiency of a single molecule. The population distribution of donor-acceptor distances in single molecules can be determined by gathering a large number of FRET efficiencies for single molecules[133]. As the confocal probe volume is very low and contains only a single freely diffusing molecule for a few microseconds, smFRET is able to capture transient fluctuations in the structure of proteins and complexes labeled with donor and acceptor dyes.[134] Immobilizing molecules to a surface enables measuring longer dynamics up to minutes[135]. Figure 1.18 illustrates a confocal microscope setup for collecting smFRET data.

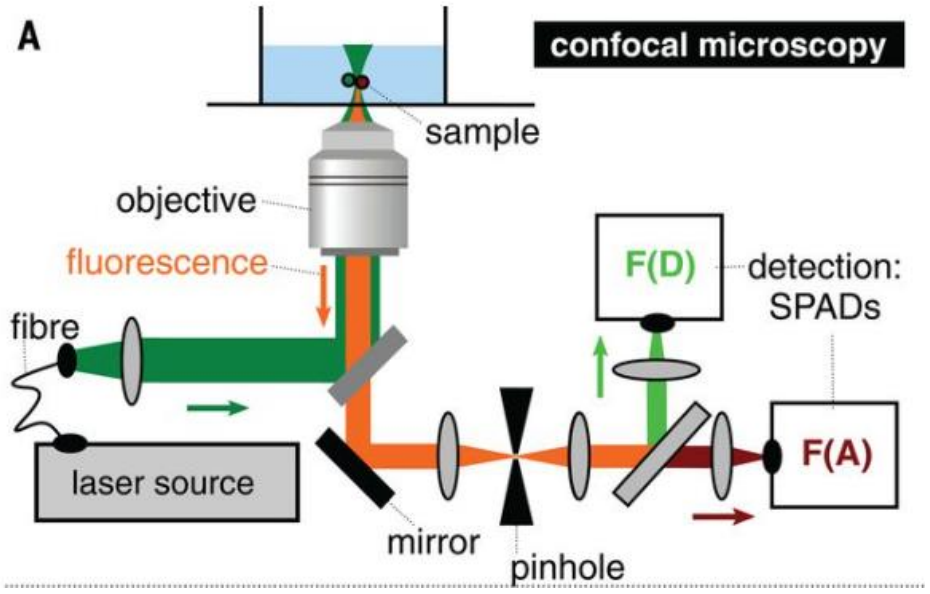

Figure 1.18. Schematic of a confocal microscope setup used for the acquisition of diffusion-based smFRET data; F(D) and F(A) indicate the donor and acceptor detection channels, respectively. Figure and caption reproduced with permission from reference[136].

After collecting the intensity data from the donor and acceptor channels, the FRET efficiency can be calculated as *E* (Equation 1.8). It should be noted that the calculated intensity here is the apparent intensity. Corrections for the detector quantum efficiencies and the quantum yields of the dyes are required to calculate the true FRET efficiency and absolute inter-dye distances[137].

1.3.3 Fluorescence Correlation Spectroscopy (FCS)

FCS measures temporal fluorescence intensity fluctuations of single fluorophores diffusing in and out of a femtoliter observation volume, which provides information about the translational diffusion coefficient of molecules[112]. The rate of fluorophore diffusion affects the rate at which the fluorescence intensity changes in a similar manner as DLS, where a larger particle remains in the focal volume for longer,

resulting in smaller (slower) fluctuations[138]. The very few small numbers of observed fluorophores at any time, typically 1 – 10 molecules in the focal volume at an instant, makes FCS particularly sensitive to single molecule properties. FCS provides quantitative information about molecule concentration, diffusion coefficient, and molecular interactions[139]. The small observation volume that confocal microscopy provides in FCS measurements increases the accuracy of measurements profoundly by improving signal-to-noise ratios[140].

As illustrated in Figure 1.19, fluorescent-labeled molecules in the confocal probe volume are excited with a pulsed laser and emit photons that are captured by the objective lens. The collected fluorescence emission then passes through a long-pass dichroic mirror and is subsequently collected by sensitive detectors, typically photomultipliers or avalanche photodiodes. Based on the arrival time of the detected photons, the autocorrelation function is calculated by software in a manner similar to DLS. When using a pulsed laser two timings are recorded for each detected photon, the macroscopic arrival time corresponding to the initial time of the experiment and a delay time corresponding to the onset of each excitation pulse. The benefit of using a pulsed excitation is an enhanced fluorescence intensity and removal of after-pulse noise[141,142].

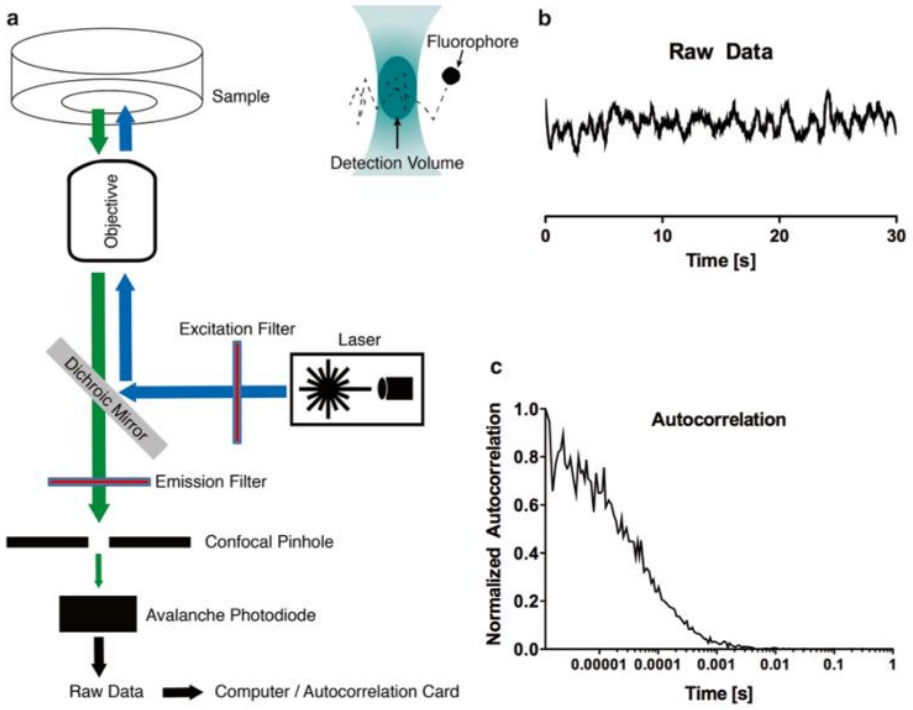

Figure 1.19. Fluorescence correlation spectroscopy (FCS) setup. (a) A confocal microscope, laser, dichroic mirror, and detector. (b) Raw data showing the time dependent fluorescence intensity over the course of measurement. (c) real time autocorrelation function constructed from the time dependent intensity trace. Figure and caption reproduced with permission from reference[143].

To extract the information regarding the concentration and diffusion of particles from the intensity data, the raw data should first be processed into an autocorrelation function using the equation 1.10 in which G(τ) is the autocorrelation function, δF(t) is the fluctuation from the mean value of the signal, $< F(t) >$ is the average signal, and τ is the delay time.

$$G(\tau) = \frac{<\delta F(t) \times \delta F(t+\tau)>}{<F(t)>^2} \qquad (1.10)$$

The autocorrelation data then would be fitted by equation 1.10 to find the τ_D, the diffusion lag-time (where half of the maximum G(τ) is located on the time axis) and κ, the eccentricity of the focal volume.

$$G(\tau) = \frac{1}{N}\left(1 + \frac{\tau}{\tau_{diff}}\right)^{-1} . \left(1 + \frac{\tau}{\kappa^2 \tau_{diff}}\right)^{-\frac{1}{2}} + 1 = G_{Diff}(\tau) + 1 \qquad (1.11)$$

By using a diffusing particle with a known diffusion coefficient and concentration, equations 1.12 – 1.14 can be used for extracting the diffusion coefficient of unknown molecules[144].

$$V_{conf} = \left(\frac{\pi}{2}\right)^{\frac{3}{2}} \omega_0^2 z_0 = \left(\frac{1}{2}\right)^{\frac{3}{2}} V_{eff} \qquad (1.12)$$

$$\omega_0^2 = 4D\tau_{diff} \qquad (1.13)$$

$$V_{eff} = \pi^{\frac{3}{2}} \kappa (4D\tau)^{\frac{3}{2}} \qquad (1.14)$$

Here τ_{diff} is the gat time for which the correlation has dropped to half of its maximum. $z_0 = \kappa \times \omega_0$ in which z_0 is the latera radius, ω_0 is the axial radius, and κ is the eccentricity of confocal volume. V_{conf} is the confocal volume and V_{eff} is the effective volume. By finding the V_{eff} using a bright freely diffusing fluorophore with a known diffusion coefficient and concentration, the diffusion coefficient (D) of unknown molecules can be calculated by the equation 1.14.

1.3.4 FCS-FRET Technique

When using FCS as a tool for studying the conformational dynamics of biopolymers, a serious limitation associated with this technique is that the fluorescence fluctuations result from the translational diffusions and the conformational changes together. How long a molecule stays in the focal volume (τ_D) and the timescales of the

dynamics under investigation affect how one interprets autocorrelation and cross-correlation curves. Since there is an overlap between the residence time of biological molecules in the focal volume, which is between 0.01 – 1 ms, further analysis is required for separating the conformational dynamic and the translational diffusion142.[145].

In the FCS-FRET correlation spectroscopy approach, the autocorrelation curve calculated by $G_{xy}(\tau) =< I_x(t)I_y(t+\tau) >/< I_x(t) >< I_y(t) >$ for donor fluorescence fluctuations (G_{DD}), and the cross-correlation between donor and acceptor molecules (G_{DA}) are recorded simultaneously for one molecule, contributing to translational diffusion equal in the two correlation functions. Therefore, the ratio of the two correlation curves (G_{DD}/G_{DA}), provides us with a correlation function with just the contributions of FRET fluctuations (conformational diffusion) and removes the contribution of translational diffusion. In this work, the function resulting from the ratio of these two correlation curves is named FRET-fluctuations[146–148].

1.4 Goals and Outline of The Dissertation

In this dissertation, we aimed to find a connection between the interconversion within the protein structure and its tendency to aggregate. We utilized FCS and FRET techniques for quantifying the rates of proteins' internal motions and the differences in the structural fluctuations among the different variants of the same protein, Beta 2-microglobulin ($\beta_2 M$), which shows enhanced aggregation in some variants, we tried to rationalize the fact that fluctuations can induce the nucleation of pre-amyloid oligomerization, which is the rate-limiting steps in most known aggregation mechanisms. There is a need for a driving force to overcome the more significant free

energy barrier between the monomers and aggregates, which have lower energy compared to the monomers. Depending on the Gibbs free energy difference between these states, this driving force could be the fluctuations between folded and the equilibrium species of folding intermediates. To initiate, we studied the aggregation mechanism in the hen egg white lysozyme solutions, which is a well-folded globular protein mainly by using dynamic light scattering.

Furthermore, we studied the redox-driven gelation in the bovine serum albumin (BSA) solutions in the unfolded states. Optical microscopy, dynamic light scattering, fluorescence spectroscopy, and rheology measurements are the main techniques used for the characterization of the BSA hydrogel. Finally, we performed fluorescence resonance energy transfer (FRET) and fluorescence correlation spectroscopy (FCS) measurements on $\beta_2 M$, which we purified using our optimized recombinant production protocol. In this dissertation, we will address the following questions:

1- How does heat-induced folding/unfolding equilibrium impact aggregation and gelation of the globular protein lysozyme?
2- What are the main drivers of aggregation in lysozyme solutions at medium (60 ° C to low (25 ° C) temperatures?
3- How does the degree of unfolding of a protein affect the kinetics of redox driven hydrogel formation?
4- How can we optimize the recombinant production, purification, and fluorescence labeling of highly monomeric $\beta_2 M$ for single molecule spectroscopy?

5- How are conformational fluctuations and intermediate folding state of $\beta_2 M$ and disease relevant mutants related to their amyloid forming ability?

The answer to the first and second questions is discussed in **Chapter 2.** Here aggregation of lysozyme, which previous studies showed does not occur under native conditions at room temperature, was stimulated by systematically heating the protein for various times to aggregate or form gels. We found that if the lysozyme solutions are held at a medium temperature (60 ° C) for a longer period, the partially unfolding of lysozyme leads to the formation of a gel network. However, if the gelation is prevented by heating for a very short period of time, the partial unfolding of lysozyme molecules causes the formation of aggregate nuclei, which grow over time. The third question is addressed in **Chapter 3,** where we used chaotropic salts to unfold bovine serum albumin to expose thiol crosslinking sites for gelation, which is driven and controlled by redox reactions. We found that using higher denaturant concentrations causes the exposure of more cysteine residues, leading to the formation of a stiffer gel network with more crosslinking. However, the larger number of exposed cysteines led to a faster consumption of fuel (H_2O_2), thus, reducing the lifetime of the gel. Question 4 is discussed in **Chapter 4,** in which we explained the step-by-step protocols for producing aggregated-free $\beta_2 M$ solutions. Here we establish a new expression protocol involving recombinant production and purification of $\beta_2 M$ with high yields of purified protein. The high quality of produced protein resulted from fusing it to SUMO, a soluble partner, which assisted in refolding and improved cleavage yield. Finally, the last question is addressed in **Chapter 5**, where we perform single-molecule fluorescence experiments on $\beta_2 M$ and its aggregation-prone variants. A combination

of fluorescence correlation spectroscopy and single molecule FRET showed the presence of intermediate folding states in β_2M and its aggregation-prone variants and revealed that these intermediates interconvert on time scales ranging from tens of microseconds to milliseconds. Together the experiments suggested the existence of 3 intermediate folding states that led to observable changes in FRET efficiency. These results demonstrated that the time scale of the conformational fluctuations correlated with the aggregation propensity of aggregation prone β_2M variants. This work supports our hypothesis that interconversion between intermediate folding states serves as the driving force for oligomer formation and/or amyloid nucleation in β_2M variants. We conclude the thesis in **Chapter 6** by summarizing the work and proposing future avenues for research in these topic areas.

Chapter 2: Effect of Protein Unfolding on Aggregation and Gelation in Lysozyme Solutions[1]

2.1 Introduction

Aggregation of proteins and peptides is a broad and complex phenomenon with several subsets, each progressing via a distinct mechanism[149]. Neurodegenerative diseases such as Alzheimer's disease and Parkinson's disease, caused by misfolding and aggregation of proteins followed by precipitation of these aggregates in the central nerves system, are examples of indigenous protein aggregation[150]. Detailed understanding of the aggregation mechanism would help to gain insight into the origin of diseases and their prevention[151]. Because some of the amyloidogenic proteins have a three-dimensional folded structure[152], studying the difference between the driving forces for aggregation of finely folded and partially unfolded proteins would help to elucidate the aggregation mechanisms of pathogenic proteins responsible for amyloid diseases. In biopharmaceuticals protein-based drug formulations may undergo reversible or irreversible aggregation at high concentrations, which negatively affects their therapeutic efficiency and consequently introduces challenges in their production and clinical administration[153]. The increase in the number of protein drugs and the obstacles, caused by aggregation, in production and shelf-life of these drugs is another motivation for studying the aggregation mechanisms[151].

[1] Note: This chapter was previously published by Nikfarjam et al. and reproduced here with minor modifications: Nikfarjam, S.; Jouravleva, E. V.; Anisimov, M. A.; Woehl, T. J. Effects of Protein Unfolding on Aggregation and Gelation in Lysozyme Solutions. Biomolecules 2020, 10 (9), 1262. https://doi.org/10.3390/biom10091262.

There are several known mechanisms of aggregation in proteins[154]. Depending on the degree of protein folding in the aggregate, the aggregates can be formed either reversible or irreversible[154]. While primary and secondary structures of a protein are internal factors affecting the aggregation propensity of a protein, external factors such as the temperature, pH, ionic strength, shear stress and concentration can also affect the aggregation of proteins in solutions[155–157]. The reversible protein oligomers arise from monomers in their native states[158]. As a next step, these oligomers can form irreversible aggregates if the interactions in an oligomeric state favor the conformational change of the monomers towards an aggregate prone state[153,159]. In aggregation through another mechanism, originated from non-native contacts, alteration in conformation of proteins due to heat or physical stress may lead to the formation of irreversible aggregates[154,160,161]. Depending on the pH and ionic strength of solution and at high enough protein concentrations[162,163], by prolong heating, the aggregates associate and eventually can form a gel network[164–166].

A clear mechanism of interplay between protein aggregation, phase separation and gelation, is difficult to establish for several reasons—proteins show unique behavior depending on their amino acid content and function. Additionally, aggregation comprises multiple steps depending on the environment. Finally, detection of smaller aggregates with a short lifetime is experimentally nontrivial. Lysozyme is a popular model protein, due to its structural and functional simplicity, extensive documentation and commercial availability. However, there are several unresolved

issues regarding lysozyme aggregation. In particular, the nature of its folding/unfolding intermediates, transient oligomerization and the role of gelation.

Several publications of lysozyme solutions mentioned the presence of mesoscopic aggregates or so called "mesoscopic protein-rich clusters"[167,168]. It was found that these aggregates typically had a diameter between 60–200 nm and a fraction of ~10−4 of total soluble protein[169]. The aggregates were commonly thought to be reversible[170], undergoing dynamic molecular exchange with protein in solution[171].

In our previous study[172] on the nature of mesoscopic aggregates in solutions of lysozyme, we investigated the effects of concentration, filtration and temperature on the sizes and relative amount of mesoscopic aggregates in solutions of lysozyme. We showed that systematic filtration through 20 nm filters completely removed the aggregates from solution. Moreover, the aggregates did not reemerge. This indicates that the aggregates of lysozyme are unlikely to be a result of reversible self-assembly of unfolded lysozyme molecules. Therefore, the aggregates do not form from lysozyme monomers in their native, biologically active folded state. However, the origin of the main driving forces of aggregation in lysozyme solutions at moderate and low temperatures remain elusive.

In this work we investigate a connection between the formation of lysozyme aggregates and protein unfolding triggered by heating. In particular, we clarify the effect of heating duration on the formation and growth of lysozyme aggregates and a gel network. Formation of the gel network at a nearly neutral pH and low ionic strength occurs in concentrated solutions of lysozyme at about the same temperature as protein

denaturation, which prevents direct studies of protein aggregation without being affected by gelation. To block the formation of a gel, we used rapid heating to the protein melting temperature following by quenching to the room temperature. This protocol enabled us to monitor in real time the step-by-step formation of small aggregates, which originate from a certain fraction of unfolded protein molecules, acting as nucleus of amyloid aggregates, by forming amorphous nanoscale aggregates first. If gelation is prevented, nanoscale aggregates (about 10–15 nm radius) are formed. At room temperature, when the samples are monitored for weeks, these clusters persist and can further form larger aggregates. If gelation is not prevented, these clusters become the building blocks of the gel network and define its mesh size.

2.2 Materials and Methods

Lyophilized powder of lysozyme (Mw = 14 kDa) was obtained from ThermoFisher Scientific (20,000 units/mg solid). HEPES buffer (Sodium salt of 4-(2-hydroxyethyl)-1-piperazineethanesulfonic acid, >99%) was supplied as a solid powder from VWR. All lysozyme samples for dynamic light scattering (DLS) studies were prepared in a 20 mM HEPES buffer at pH 7.8 and filtered through 100 nm and 20 nm pore filters, according to the procedure explained in our previous work172.

By DLS, we studied three concentrations of lysozyme, 18, 30 and 60 mg/mL. The concentration of protein samples were measured by using the absorbance at 280 nm. The details the DLS techniques and measurements are described in our previous work [172]. The lyophilized lysozyme powder was directly dissolved in the buffer for the preparation of the concentrated stock solution. The concentrations were measured after filtration with 200 nm filters. The samples with the desired concentrations were then

prepared by dilution. DLS measurements were taken using a multi-angle dynamic light scattering complex from Photocor. Autocorrelation functions were generated for 600 s at each specific angle and temperature. HEPES buffer has a temperature coefficient equal to −0.14, increasing the temperature to 80 °C would decrease the pH less than by 10%, which that should not affect the aggregation. Additionally, a sodium dodecyl sulfate–polyacrylamide gel electrophoresis (SDS-PAGE) gel analysis on both heated and unheated 30 mg/mL samples was performed to investigate the possibility of protein's degradation. The unheated samples and the sample heated to 80 °C for 30 min were incubated at room temperature for three weeks prior to running the SDS-PAGE gel. Also, the heated and unheated samples were additionally incubated at 95 °C for 5 min right before running the gel.

2.3 Results

2.3.1 Apparent Monomer Size

Primarily, DLS measures the scattering intensity autocorrelation function, exponentially decaying with the diffusive relaxation rate of optical inhomogeneities that exhibit Brownian motion in solution[173],

$$\Gamma = Dq^2, \tag{1}$$

where D is the diffusion coefficient and $q=(4\pi/\lambda)n\sin(\theta/2)$ is the scattering wave number (with λ being the wavelength of light, n the refractive index, θ the scattering angle).

The hydrodynamic radius of inhomogeneities, such as the protein molecules or aggregates, is obtained by assuming the validity of the Stokes-Einstein equation that

relates the diffusion coefficient (D), viscosity of the solvent (η) and hydrodynamic radius R[173]:

$$D = \frac{kBT}{6\pi\eta R}, \quad (2)$$

where k_B is Boltzmann's constant and T is the temperature.

This assumption is fully justified only for dilute solutions of presumably spherical, noninteracting inhomogeneities. Formal application of the Stokes-Einstein equation to semi-dilute and concentrated protein (or, generally, polymer) solutions, results in obtaining a so-called "apparent" hydrodynamic radius that is smaller than the actual hydrodynamic radius of noninteracting individual molecules (moreover, decreasing with the increase of polymer concentration)[174]. The apparent hydrodynamic radius as a function of lysozyme concentration, obtained in our new DLS measurements for three concentrations of lysozyme, is in good agreement with our data reported previously[172]. As demonstrated in Figure 2.1, the apparent radius corresponds to the actual size of individual molecules ("monomers") only in dilute solutions of lysozyme (<10 mg/mL). One of the goals in making this chart (Figure 2.1) was to track changes in sample concentrations using the apparent hydrodynamic radius of lysozyme monomers. During the three weeks of measurements, no change in hydrodynamic radius of lysozyme monomers where observed. This observation confirms that crystal growth and sedimentation did not affect the solution concentrations. This assumption is in agree with the reported phase diagram of

lysozyme phase separation and crystallization in 20 mM HEPES and pH of 7.8 reported in Reference[169].

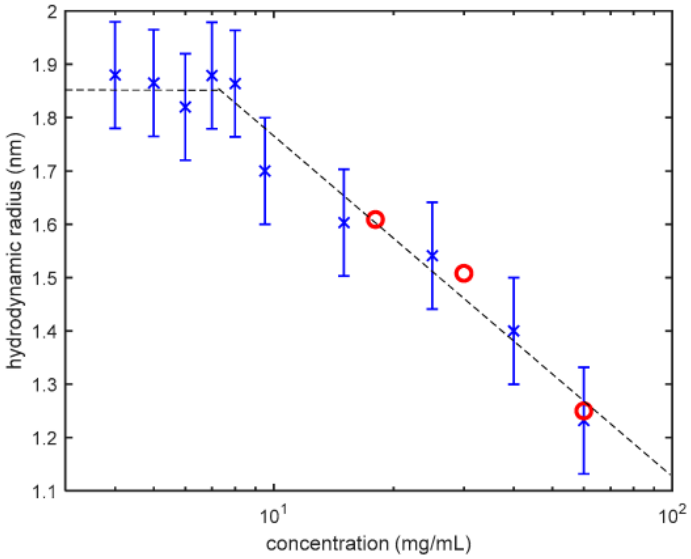

Figure 2.1. Apparent hydrodynamic radius of lysozyme monomers, obtained by DLS, as a function of concentration at 25 °C[158]. In dilute solutions (<10 mg/mL) it represents the actual size of the lysozyme monomers. Upon the increase of concentration, the apparent radius (blue crosses) sharply decreases because of the interactions between lysozyme molecules. Red circles are the results of our new measurements. The error bars represent a one percent error associated with the detected size,

It is important to note that the Stokes-Einstein equation remains valid for mesoscopic lysozyme aggregates even in concentrated solutions. This is because the number of the aggregates are relatively small. Therefore, with respects to the aggregates, the concentrated solution of lysozyme can be regarded as dilute. The hydrodynamic radius of the aggregates thus characterizes their actual size, provided that the actual viscosity of the solution is used in the equation.

2.3.2 Continuous Heating

We first studied an 18 mg/mL lysozyme solution heated from 25 °C to 62.5 °C. Using the protocol outlined in Figure 2.2a. After holding the solution for 8 h at 55 °C, we observed a change in the DLS autocorrelation function (g2), presented in Figure 2.2b, which marks the onset of aggregation. Two characteristic sizes of the aggregates, of the order of ~30 and ~100 nm, were detected. After further heating and holding the sample for about 60 h at 62.5 °C, as shown in Figure 2.2b, the autocorrelation function demonstrated a dramatic shift from a double exponential to a broader spectrum of the size distribution (Figure 2.2c). The distribution reveals three characteristic length scales, one corresponding to apparent size of lysozyme monomers ~1.5 nm, another one to small number of ~100 nm aggregates and a third to inhomogeneities with a length scale of about 15 nm in size, which are dominant. Cooling the sample back to the room temperature did not change the DLS characteristics of the sample. Visual observation showed that the sample was in the gel state. Therefore, we interpret the length scale of about 15 nm as the gelation mesh size.

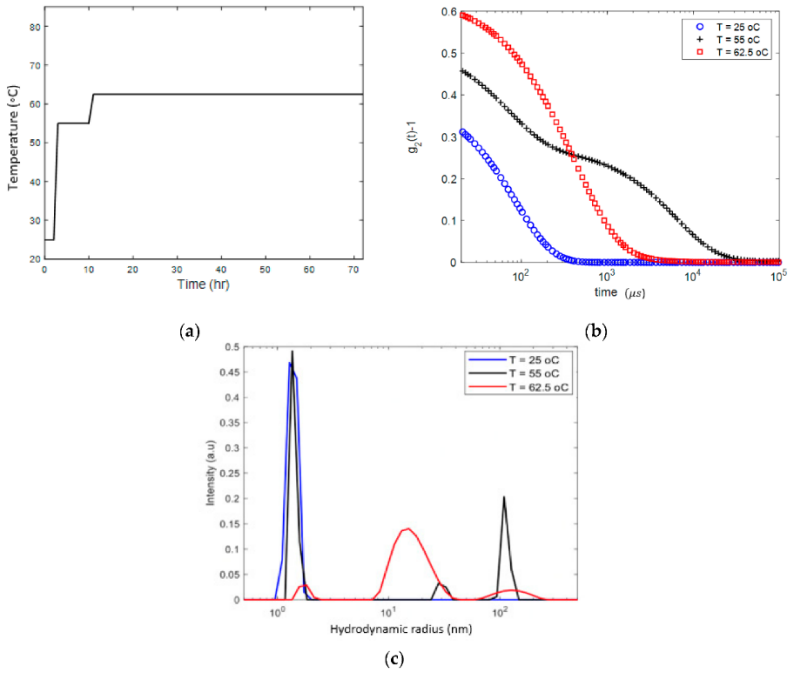

Figure 2.2. Heating protocol (a) and DLS analysis (b) and (c) demonstrating the process of aggregation and gelation in the 18 mg/mL lysozyme solution, gradually heated to 62.5 °C and kept at this temperature for 60 h. (b) DLS autocorrelation function (θ=45◦) before and after gel formation; (c) size distribution of the apparent inhomogeneities before and after gelation.

We performed another experiment on a lysozyme solution of about the same concentration (20 mg/mL) but with a different protocol. The sample was heated to 60 °C and the DLS correlation function was measured after 18, 42 and 90 h while held at this temperature. The results are presented in Figure 2.3. We observe the formation of inhomogeneities of a radius growing from ~17 nm after 18 h (with a significant dominance of the nano-sized monomers and oligomers) to ~40 nm after 42 h and to 80–90 nm after 90 h. Remarkably, after 90 h at 60 °C, a meso-size (~20–25 nm) reemerges, while the size distribution of the larger aggregates becomes narrower. Qualitatively, this experiment shares features with the results presented in Figure 2.2; the growth of aggregates (a faster process) starts before gelation (a slower process of formation of network with a mesh size of about 15–25 nm).

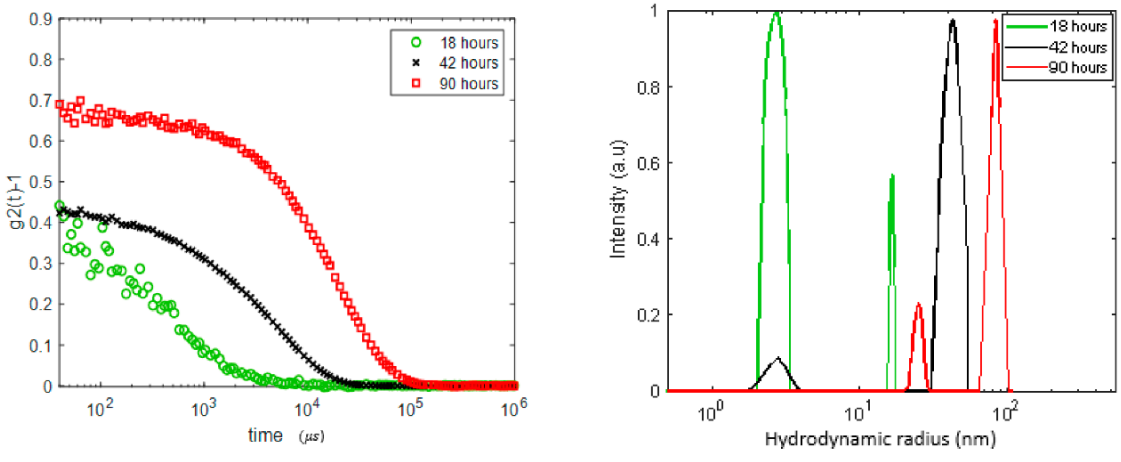

(a) (b)

Figure 2.3. DLS analysis in the 20 mg/mL lysozyme solution gradually heated to 60 °C and kept at this temperature for 18, 42 and 90 h. (a) DLS autocorrelation function (θ=90∘) before and after gel formation; (b) size distribution of the apparent inhomogeneities. Note an increase in apparent monomer size due to oligomerization.

We have also found that, for this sample, despite gelation occurring after 90 h of incubation, the decay rates for both inhomogeneities, 20–25 and 80–90 nm, exhibit a q^2 linear dependence that is characteristic for diffusive relaxation (Figure 2.4).

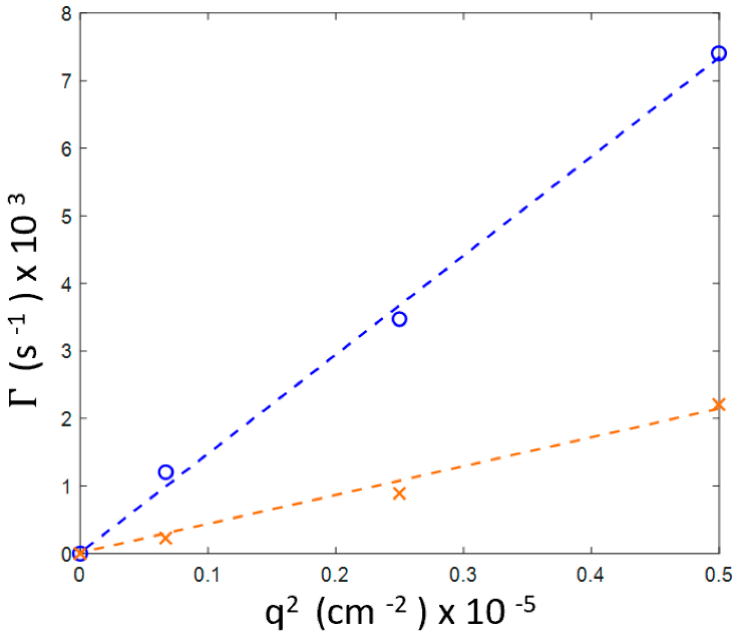

Figure 2.4. Wave number dependence for three scattering angles (30°, 60° and 90°, q∝sin(θ/2) of the two decay rates in the 20 mg/mL sample after 90 h of holding at 60 °C (see Figure 2.3b). Blue line: fast mode (smaller aggregates), orange line: slow mode (larger aggregates).

2.3.3 Preventing Gelation and Long-Time Monitoring

Our other heating experiments included the rapid heating of two lysozyme samples (18 mg/mL and 30 mg/mL) to the projected unfolding temperature, 80 °C. We explored the finding that the emergence and growth of aggregates is significantly faster

that the time of gelation. To prevent gelation, the sample was kept at this temperature for a short period of time (30 min) following fast cooling to room temperature. The samples were then kept at room temperature and monitored with DLS for over two weeks. The DLS results are shown in Figure 2.5 and Figure2.6.

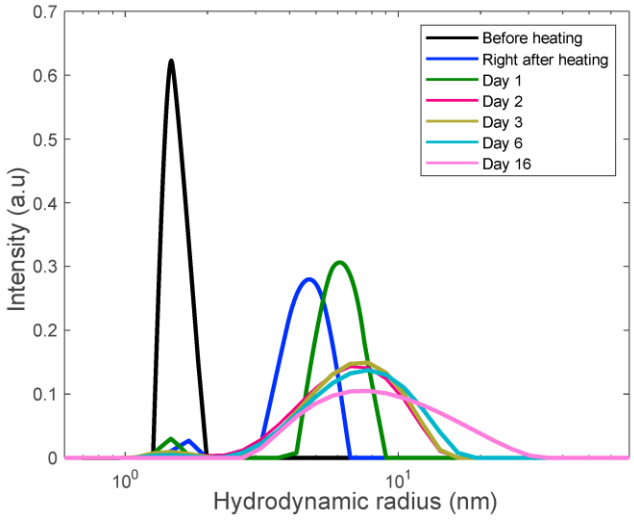

Figure2. 5. Long-term monitoring of the 18 mg/mL lysozyme solution via DLS. Solution was rapidly heated to the unfolding temperature of 80 °C and held there for 30 min at this temperature to trigger aggregation.

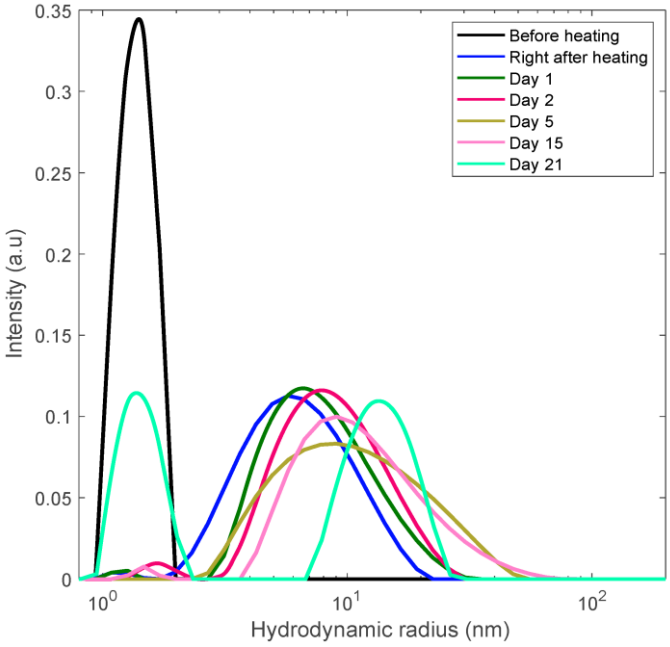

Figure 2.6. Long-term monitoring of the 30 mg/mL lysozyme solution via DLS. The solution rapidly heated to the unfolding temperature of 80 °C and held there for 30 min at this temperature to trigger aggregation.

In these figures the sequence of the line colors corresponds the sequence of monitoring days. One can see the formation of polydisperse nanoscale aggregates with gradual increase of the contribution of aggregates with the size of 10–15 nm. Note that this value is close to the length scale that we interpret as a mesh size of the gel network. The average size of aggregates for the 18 mg/mL (Sample 1) and 30 mg/mL (Sample 2) lysozyme solutions heated for 30 min in 80 °C, cooled down and monitored at room temperature as a function of the monitoring time is presented in Figure 2.7. The results are well described by the diffusion-limited aggregation law[175,176]:

$$R = R0 + At^{\frac{1}{df}}, \qquad (3)$$

where R0 is the initial radius of aggregates/monomers (1.6 and 1.5 nm, respectively), t is time, A is a constant and df is the fractal dimension of aggregates (Table 1). For both samples Equation (3) was fitted to the experimental data on the aggregate size as a function of time, with using the MATLAB Levenberg-Marquardt algorithm. The data are consistent with the maximum fractal dimension, df=3, indicating that the lysozyme aggregates can be viewed as relatively compact spherical objects[177]. We find it not surprising that the ratio A2/A1=1.65 is almost equal to the sample concentration ratio, namely 1.66.

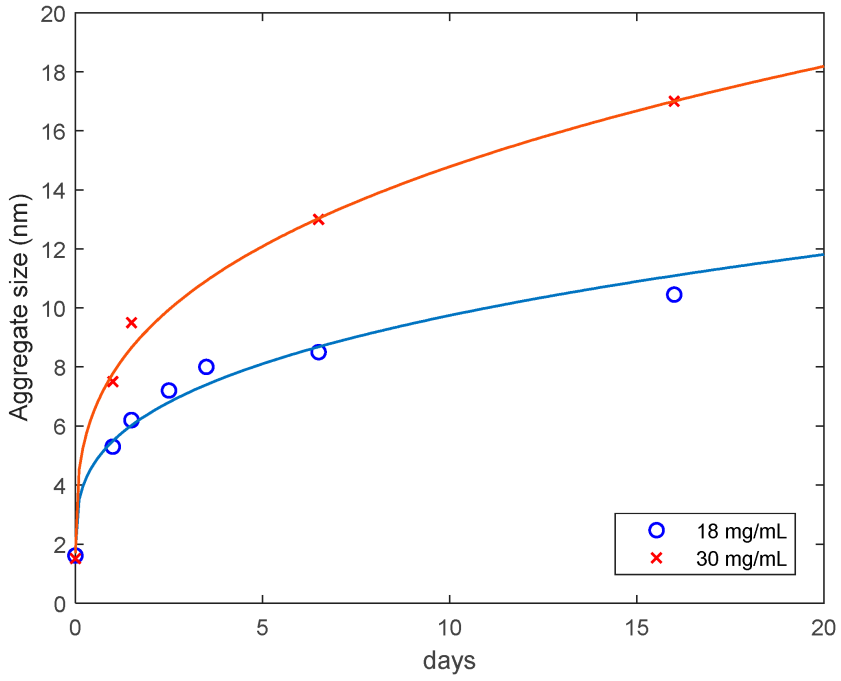

Figure 2.7. Average hydrodynamic radius of lysozyme aggregates in solutions of 18 mg/mL and 30 mg/mL samples, as a function of time. The solid curves are approximations with Equation (3).

Table 2.1. Fitting parameters in the diffusion-limited aggregation law, with $df = 3$.

Concentration (mg/mL)	Amplitude (A)	Standard Deviation
18	3.68	±0.37
30	6.07	±0.36

2.3.4 Formation of Polydisperse Aggregates

We used the same protocol of measurements for a more concentrated solution, 60 mg/mL but observed a different pattern of aggregation phenomena. In addition to monomeric-like and mesoscopic (~10 nm) inhomogeneities, the sample reveals of formation of a broader spectrum of large aggregates growing from 200 nm to almost a micron (Figure 2.8). However, these aggregates are so large that their growth is

accompanied by gradual sedimentation, thus, upon a time, resulting in decreasing their contribution in the DLS correlation function.

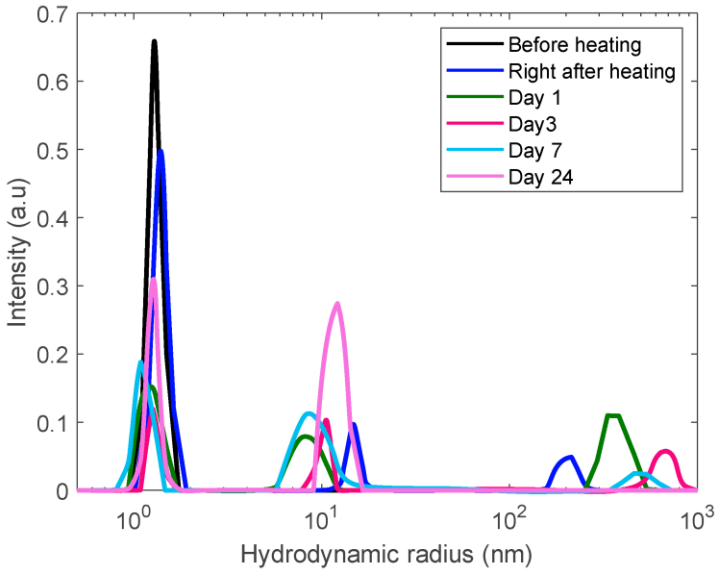

Figure 2. 8. DLS size distribution analysis of a 60 mg/mL lysozyme sample heated for 30 min at 80 °C to trigger aggregation and monitored for 24 days.

Proteins may undergo oxidative or enzymatic degradation over a long time of incubation. This is an important issue that we have considered seriously. Indeed, according to the work of Avanti et al.[178], a heat stressed lysozyme loses about 60% of its activity after 3 weeks of incubation due to degradation. While it is certainly probable that our samples undergo degradation, while being kept at room temperature during a long period of time, we tried to minimize this effect by filtering samples by a 20 nm pore size filter to remove any bacteria from the solution. Buffers were degassed prior to use, so the amount of oxygen in the solution was minimized. However, some degradation was still possible. Therefore, to test the effect of lysozyme's degradation on the aggregation, a 60 mg/mL sample was kept at 80 °C for 10 min, quickly cooled down to room temperature and was monitored over three weeks. The amount of

aggregates formed during that period, was so small that was hardly detectable (Figure 2.9). Additionally, an SDS-PAGE gel analysis (illustrated in Figure 2.10) on both heated and unheated 30 mg/mL samples confirmed the absence of protein's degradation during the experiments, as no lower molecular weight fragments was observed, while some protein dimers and trimers were detected in heated samples. We conclude that the aggregation mechanism in our study is insignificantly affected by lysozyme degradation.

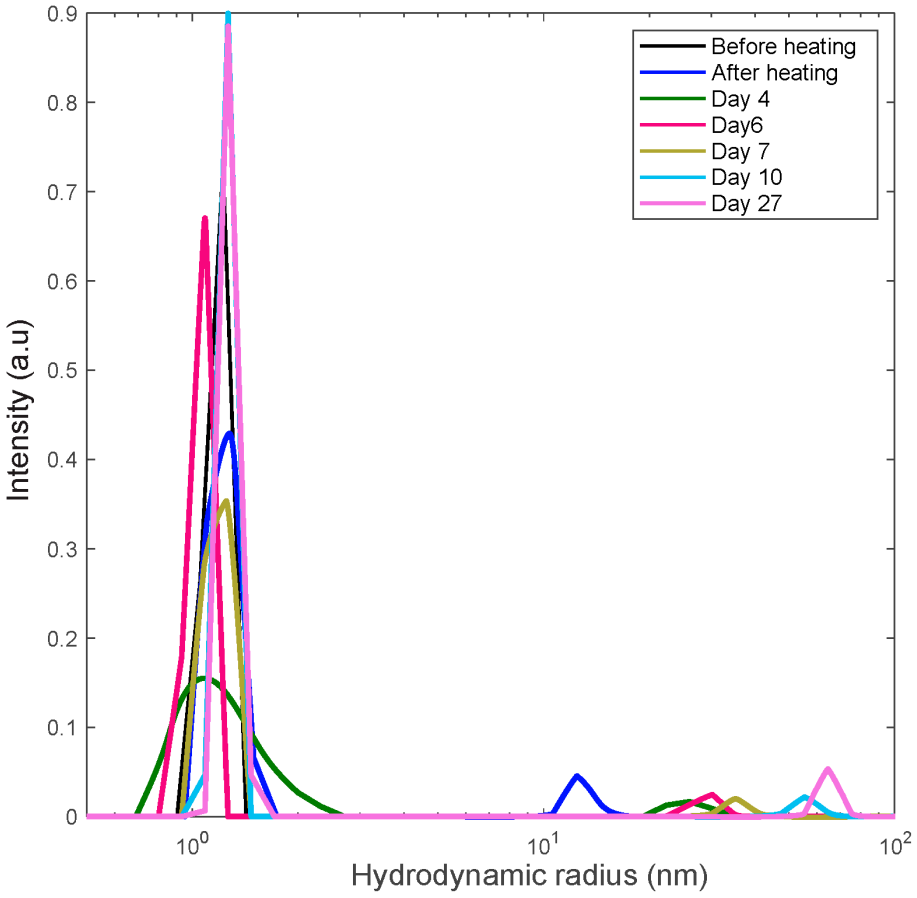

Figure 2.9. DLS distribution analysis of a 60 mg/mL lysozyme sample heated for 10 min at 80 °C to screen the effect of heating on the aggregation process.

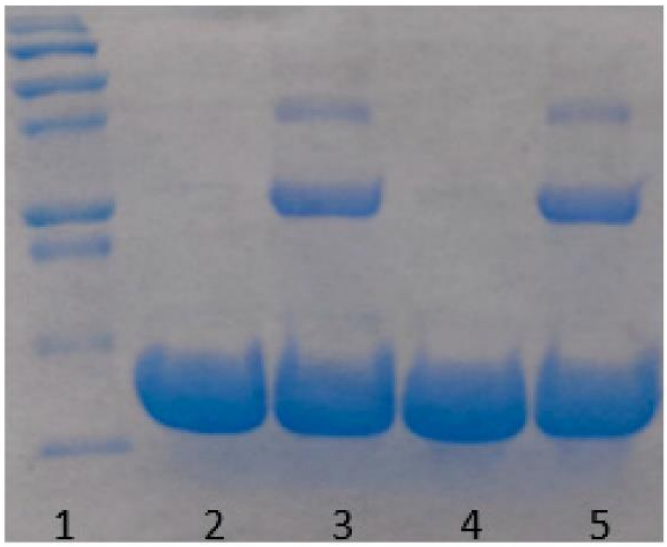

Figure 2.10. SDS-PAGE gel image for Lysozyme (30 mg/mL) incubated at room temperature for three weeks prior running the gel. Left to right: 1. Ladder (From the bottom 10, 15, 20, 25, 37, 50 kDa). 2. Sample unheated. 3. Sample heated to 80 °C. 4. Sample unheated, then incubated at 95 °C for 5 min prior running the gel. 5. Sample heated to 80 °C, then incubated at 95 °C for 5 min prior running the gel.

2.4 Discussion

Globular proteins may undergo structural changes due to partial unfolding when being exposed to a higher temperature, even below its true denaturation point. As a result, normally buried hydrophobic residues may act as a crosslinker for intermolecular beta-sheet structures and lead to formation of aggregates of different shapes, globular or amyloid like, depending on the solution conditions[164,179,180]. Continuous heating leads to association of aggregates and subsequent formation of a gel network[164,166,180–182].

Based on our findings, we can qualitatively suggest a mechanism of aggregation that we observed in lysozyme samples treated under different heating protocols.

Lysozyme at low ionic strength (20 mM) and nearly neutral pH unfolds at a temperature around 80 °C[170].

We estimate the fraction of unfolded lysozyme molecules, $\boldsymbol{\phi}$, as a function of temperature through the enthalpy of folding/unfolding, $\boldsymbol{\Delta H_0}$ (kJ/mol), at the "melting" temperature $\boldsymbol{T_0}$, defined to be the temperature at which the fraction of folded and unfolded lysozyme is equal. In the first approximation, we obtain:

$$\frac{\Delta H_0}{k_B}\left(\frac{1}{T}-\frac{1}{T_0}\right)=\ln\left(\frac{\phi}{1-\phi}\right). \quad (4)$$

According to References[170,183,184], the enthalpy of lysozyme unfolding varies between 200 and 600 kJ/mol, depending on experimental techniques and buffer conditions. In Figure 2.11 we present the fraction of unfolded lysozyme, calculated from Equation (4), with adopted values of $\Delta H_0 = 540\ kJ/mol$ and T0=80 ∘C [34]. In this adoption we neglect a dependence of ΔH0 and T0 on lysozyme concentration.

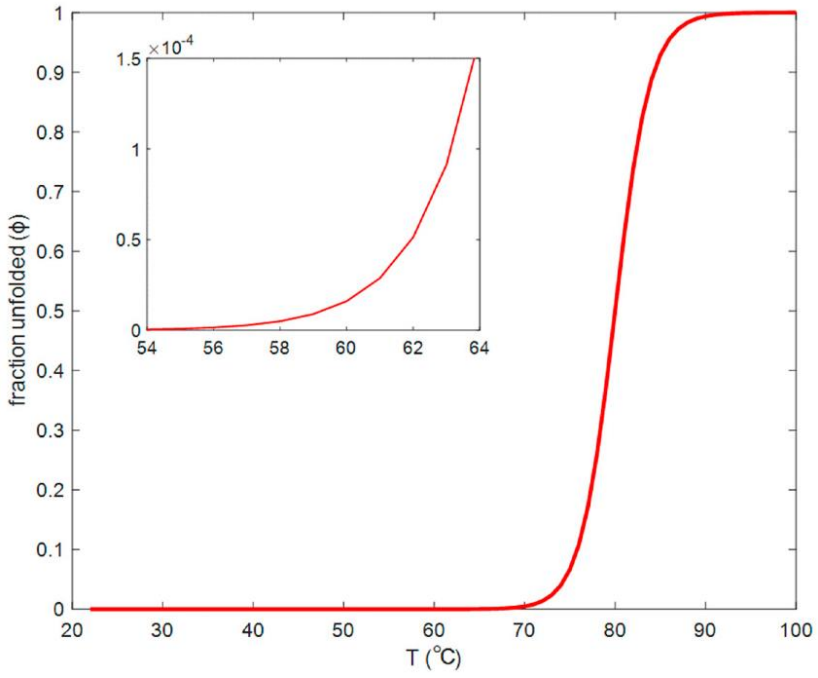

Figure 2.11. Fraction of unfolded lysozyme as a function of temperature.

In the hierarchy of times scales, the lysozyme interconversion rate is fastest (overall folding time is of the order of 1 s)[185,186], while characteristic times of the motion of molecular segments could be of the order of 1 μs[187]. Then a relatively lower rate of aggregation follows. The rate of gelation is the slowest and strongly depends on concentration and temperature. Our experiments on a 20 mg/mL sample showed that at 60 °C it took up to 90 h to observe a distinct gel state. The lower the temperature, the smaller the fraction of unfolded lysozyme molecules, the smaller the probability of aggregation and larger the time of gelation. As estimated with Equation (4), the fraction of the unfolded molecules at 60 °C could be as small as 2×10−3%. Nevertheless, these molecules serve as seeds of nucleation to form growing aggregates and eventually a gel network. We must note that even an extremely small number of mesoscopic aggregates could make a significant contribution to the DLS correlation function because light scattering intensity strongly depends on the size, especially at small scattering angles. The reaction coordinate, the fraction of unfolded protein molecules, exhibit thermal fluctuations around its "chemical reaction" equilibrium value. The average amplitude and lifetime of these fluctuations depend on the thermodynamic conditions and can be found by statistical thermodynamics. However, because the distribution of the fluctuations in space and time is Gaussian, occasionally, during a long observation time, the deviations in concentration of the unfolded protein from the equilibrium value, could become significant and hence initiate the gelation process.

The analysis of the correlation function of gel formed by heating lysozyme solutions ~20 °C below the melting temperature over a long period of time indicates the presence of diffusion relaxation in the gel. In this work we did not address the

interesting dynamic properties of gels, which would require a more detailed DLS experiments and analysis. We just note that the correlation function of density/concentration fluctuations in gel can exhibit a compressed exponential decay[164,182]. The observed relaxation modes can be attributed to concentration fluctuations of the aggregates which are not a part of gel network, branching points, segments and restructuring of the gel[179,180,188]. In case of the extremely fragile lysozyme gel, the diffusive inhomogeneities with the sizes ~15–20 and ~100 nm (Figure 2.2c, red curves), could be interpreted as a branch/mesh pattern forming the gel network (smaller size) and separate aggregates (larger size) diffusing across the network.

2.5 conclusions

In this work, the role of equilibrium unfolding as the main driving force for protein aggregation at elevated temperatures is clarified. While monomeric lysozyme molecules do not have a propensity to form detectable aggregates for a long period of time[172], increasing the temperature and shifting the equilibrium to marginally unfolded protein leads to the emergence of aggregate seeds. These seeds can either rapidly grow if heated continuously or undergo a slow diffusion limited aggregation over a long time of monitoring.

Our results resonate with the observations of previous investigators on aggregation phenomena in lysozyme solutions. The importance of driving forces for aggregation at physiological temperatures was emphasized in the work of Vekilov et al.[171], where the presence of transient dimers of lysozyme was found. Also, according to Strander et al.[158], at the same ionic strength and pH, the presence of short-range

attractions and long-range repulsions leads to the formation of dense liquid phases in lysozyme solutions. The reported clusters have an aggregation number between 2–7 monomers per cluster at the range of concentrations of 50–100 mg/mL. DLS was not able to detect the presence of such clusters. The lack of DLS ability for the detection of these clusters can be because of the short lifetime of the clusters and/or their small population. However, although these clusters have a very small population, they may be involved in the formation of larger observed aggregates.

According to References[189–191], amyloid aggregates can eventually form a viscoelastic gel solution. Since the time scale of gel formation is much longer than the folding/unfolding interconversion and aggregation, the aggregation is a required step for the gel formation. A fundamental, yet unexplored problem that could be addressed in further experimental and theoretical studies, would be a possible role of fluctuations of unfolded molecular states near the interconversion equilibrium. Protein molecules can fluctuate between their alternative states and eventually bind to each other and form aggregates. Fluctuation-induced aggregation[192] and, more recently, fluctuation-induced phase transitions[193] have been discussed with respect to the phase behavior of classical colloids. It would be interesting to investigate this effect with respect to aggregation of proteins.

Chapter 3: Chemically Fueled Dissipative Assembly of Protein Hydrogels Mediated by Protein Unfolding

3.1 Introduction

Cells maintain homeostasis far from thermodynamic equilibrium through constant consumption of chemical energy to regulate protein expression, cellular transport, osmotic pressure, and cell shape. The cytoskeleton consists of a complex network of biomacromolecular assemblies that dynamically crosslink and dissolve to enable cell motility and division, organelle transport, and responses to external mechanical signals[194–198]. For instance, microtubules are maintained in a state far from equilibrium by a process called dissipative assembly, in which continuous binding of adenosine triphosphate (ATP) to tubulin proteins causes microtubule growth while ATP hydrolysis causes microtubule shrinkage and collapse. The concentration of microtubules is dictated by reaction kinetics, such as reactant concentration and reaction rates, instead of thermodynamic equilibrium relationships (e.g., equilibrium constants). The far from equilibrium nature of the microtubules enables cell to rapidly respond to their environment and execute precisely timed processes[195–197,199,199].

Prior work on assembly of soft matter has mainly focused on near equilibrium self-assembly of structures like vesicles and micelles[200,201] and nanoparticle superlattices[202,203]. Here, molecular interactions between building blocks determines their equilibrium assembly state, akin to an equilibrium reaction. A key difference between dissipative assembly processes and near equilibrium self-assembly is that the assembled structure concentration is controlled by reaction kinetics instead of reduction in free energy of the system[204–206]. The dynamic structure of microtubules and

associated reactions has motivated design of synthetic soft materials that display dissipative assembly[207]. Seminal work by Boekhoven et al.[208] showed that small polar molecules in water rapidly react with chemical fuels to form transient hydrogels due to conversion of polar functional groups to non-polar groups. Simultaneous slow hydrolysis of the water reactive non-polar functional groups dissolves the hydrogel after several hours. A number of works have utilized similar reactions for dissipative assembly of hydrogels[209–211], colloids[212,213], nanoparticles[214–217], polymers[217–219], and emulsions[220–223]. These prior works have displayed a range of exotic behaviors, such as transient assembly, self-sorting, simultaneous growth and dissolution, and transient catalysis. While these synthetic systems have established a library of synthetic chemistries and building blocks for dissipative assembly, there are no prior reports using proteins as the building blocks for dissipative assembly. Prior works on static protein hydrogels have demonstrated rich effects of protein structure and protein-protein interactions on the hydrogel properties. For instance, Hughes et al. showed that protein folding state and hydrophobic interactions mediate microscopic network architecture and the mechanical properties of protein hydrogels[224–227]. Dissipative assembly of proteins and protein hydrogels could enable temporal control over protein function, such as enzymatic activity, or unlock new ways to control the dynamic properties of transient soft materials.

Here we demonstrate dissipative assembly of transient bovine serum albumin (BSA) hydrogels using a redox cycle involving a fast forward oxidation reaction that forms disulfide crosslinks and a slow simultaneous back reaction that reduces disulfide bonds to free thiols. The oxidation reaction forms disulfide crosslinks between solvent

exposed cysteine groups while the slow reduction reaction degrades the hydrogel once the oxidizing agent is depleted. In contrast to prior dissipative assembly studies that focused on how fuel concentration impacts hydrogel lifetime, this work utilizes a chemical denaturant to explore the effects of protein unfolding on hydrogel lifetime and mechanical properties. We present experiments demonstrating that stepwise unfolding of the multidomain BSA mediates fuel consumption kinetics, hydrogel lifetime, and mechanical properties via the concentration of solvent exposed cysteines on the proteins. This work highlights the effects of protein structure on fuel reaction kinetics and transient hydrogel lifetime during dissipative assembly that were not previously observed for small molecules or polymers. Aside from the well-established effects of fuel concentration, the results presented here establish molecular structure as an additional lever for controlling dissipative assembly.

3.2 Experimental Section

3.2.1 Reagents and Hydrogel Preparation

To prepare the protein hydrogels, 90 mg/ml of dry BSA (Millipore Sigma, lyophilized powder, essentially fatty acid free, 50 mM cysteine) and 200 mM of dithiothreitol (DTT, Thermofisher Scientific) were dissolved in denaturing buffer containing 4 – 6 M guanidine hydrochloride (Gdn-HCl, Thermo Scientific, purity > 99.5), 100 mM citric acid (Millipore Sigma, ACS reagent > 99.5), and 200 mM sodium phosphate dibasic. Type II DI water (18.2 MΩ) was used for all solutions in this study. The pH was adjusted to 5.4 with 10 M sodium hydroxide (NaOH). The mixture was stirred at a speed of 1000 rpm for 15 minutes prior to addition of chemical fuel. Hydrogen

peroxide (H2O2) at a final concentration of 150 mM was added to the samples unless otherwise noted and stirred for tens of seconds to uniformly mix the solution.

3.2.2 Dynamic Light Scattering (DLS)

A photon correlation spectrometer (Photocor Complex) equipped with a 650 nm diode laser and photomultiplier detector (PMT) was used to perform dynamic light scattering (DLS) to monitor the formation and melting kinetics of the hydrogels over time. Here the BSA monomers and aggregates in the solution scatter light due to their Brownian motion, causing fluctuations in the intensity of the total scattered light on the PMT. The normalized intensity autocorrelation function $g(\tau)$ is calculated from measurements of the scattered light intensity as a function of time using the following equation:

$$g_2(\tau) = \frac{\langle I(t)I(t+\tau)\rangle}{\langle I(t)\rangle^2}. \quad (1)$$

Here $I(t)$ is the time dependent scattered light intensity on the PMT and τ is the lag time between two time points. The carrot brackets indicate an average taken over the entire time course of the experiment. For a polydisperse system the characteristic decay time for each particle size in the solution can be extracted by fitting a sum of exponential decays to the autocorrelation function:

$$g_2(\tau) - 1 = \left[\sum A_i \exp\left(-\frac{t}{\tau_{D_i}}\right)\right]^2. \quad (2)$$

Here A_i are the amplitudes and $\tau_{D,i}$ are the decay times of each size of particle in solution. The latter is inversely proportional to the diffusion coefficient (D_i) of the particles as

$$\frac{1}{\tau_{D,i}} = D_i q^2, \quad (3)$$

where $q = (4\pi/\lambda)\sin(\theta/2)$ is the wave vector, n is refractive index, λ is the laser wavelength, and θ is the scattering angle. At a fixed scattering angle of $\theta = 90°$, scattering intensities were collected for 60 second durations repeatedly during the entire course of dissipative assembly. Data were processed using the DynaLs software, which uses the CONTIN algorithm to determine the corresponding decay times for polydisperse samples.[228]

3.2.3 Intrinsic Fluorescence and ANS Binding

A Jasco FP-8300(ST) spectrofluorometer was used for the BSA denaturation curve and ANS binding assay. The sample solutions for the denaturation curve contained 90 mg/ml Dextran 70 as a crowding agent and 1 mg/ml of BSA in a buffer containing 100 mM citric acid, 200 mM sodium phosphate dibasic, and various Gdn-HCl concentrations ranging from 0 – 6 M. Samples were incubated in a 25 °C water bath for 30 minutes prior to fluorescence measurements. The excitation wavelength was 280 nm (5 nm bandwidth) and the emission wavelength was measured at 340 nm (5 nm bandwidth). Ten emission scans with durations of 10 seconds (1 scan/sec) were recorded and averaged. The appropriate background was subtracted from each data point.

The 8-Anilononaphthalene-1-sulfonic acid (ANS, Sigma-Aldrich) binding measurements were performed on samples containing 30 μM BSA and 100 μM ANS in citric acid buffer with different Gdn-HCl concentrations. The excitation wavelength was 350 nm with a 5 nm bandwidth and the emission spectra were collected in the

range of 370 – 620 nm. The background was subtracted, and fluorescence intensity normalized to the protein concentration in each solution as measured by absorbance at 280 nm.

3.2.4 Free Cysteine Concentration and Crosslinking Density

Ellman's reagent (5,5-dithio-bis-(2-nitrobenzoic acid, DTNB, Thermo Fisher) was used to quantify the concentration of solvent accessible cysteine groups on the BSA as a function of denaturant concentration.[229] Briefly, lyophilized BSA was dissolved in citrate buffers containing 0 – 6 M Gdn-HCl. The BSA was incubated with a 4-fold molar excess of DTT for 60 minutes to reduce the solvent exposed disulfide bonds, followed by removal of DTT using a PD-10 desalting column. The DTT-free reduced BSA samples were mixed with the Ellman's reagent solution and reaction buffer (0.1 M sodium phosphate, pH 8.0, containing 1 mM EDTA) and the absorbance was measured at 412 nm using a UV-VIS spectrophotometer (Jasco V-730(ST)). The reaction between DTNB and a thiol group produces a molecule of 2-nitro-5-thiobenzoate (TNB) with a known molar extinction coefficient of 14,150 $M^{-1}cm^{-1}$ at 412 nm, enabling direct quantification of the solvent accessible cysteine concentration. The free cysteine concentration measured was not equal to that in the corresponding 90 mg/ml hydrogel precursor solution due to the need to dilute the protein to within the measurement range of Ellman's reagent (< 1 mM cysteine).

We utilized Ellman's reagent with a modified procedure to calculate the crosslinking density of the hydrogels. Transient hydrogel samples were prepared as described above and five minutes after gelation 300 mM N-ethylmaleimide (NEM, Sigma Aldrich) was added to block unreacted free thiol groups and consume unreacted

DTT. After a short incubation time sufficient to react all thiol groups and DTT an excess amount of 350 mM DTT was added to the samples to react the remaining NEM and reduce all the disulfide bonds. The melted hydrogel solutions were passed through PD-10 desalting columns equilibrated with the denaturing buffer to remove the excess DTT and NEM. The resulting liquid samples had free cysteine concentrations equal to half the concentration of disulfide bridges in the protein hydrogel. The samples were mixed with Ellman's reagent as described above, where two moles of TNB were produced for every mole of disulfide bonds.

3.2.5 Rheology Measurements

An AR2000 stress-controlled rheometer (TA Instruments) was used for the rheology measurements. Experiments were performed using a cone-and-plate geometry (40 mm diameter, 2° cone angle). A solvent trap was used during the measurement to prevent evaporation of water. The temperature was held constant at 25 °C by a Peltier assembly. Dynamic time sweep measurements of the storage (G`) and loss (G``) moduli were performed at a constant strain of 1% and angular frequency of 1 rad/sec.

3.2.6 Microscopy and fluorescence imaging and spectroscopy

Dark field optical microscopy was used to image protein aggregate tracers in the hydrogel. The inverted optical microscope (Zeiss, Axio Observer) was operated in reflection mode using a 20x dark field objective lens. Fluorescence macro imaging of the redox state of reacting hydrogels using the redox sensitive dye resorufin (Sigma Aldrich, ≥95.0% (HPLC)) was performed with a homebuilt fluorescence imaging setup. Resofurin was added to the protein solution at a concentration of 40 μM and a

columnated green LED source (555 nm) illuminated a 1 cm quartz cuvette filled with hydrogel in a dark enclosure. The fluorescence signal was captured 90 degrees to the light illumination pathway with a macro zoom lens and CCD camera covered by a 600 nm long pass filter.

Fluorescence spectroscopy for detection of H_2O_2 consumption rate was performed on a fluorometer (Jasco FP-8300(ST) spectrofluorometer). Resorufin was incubated at a final concentration of 40 μM with the DTT and BSA for 15 minutes in a quartz cuvette. H_2O_2 was added to the sample through a syringe port with stirring and the sample was excited continuously at a wavelength of 550 nm while measuring fluorescence emission intensity at a wavelength of 592 nm as a function of time.

3.3 Results and Discussion

3.3.1 Redox Cycle for Dissipative Assembly

BSA contains 35 cysteine residues per molecule that provide ample disulfide bond crosslinking sites for forming a hydrogel (Figure 3.1a). Prior to hydrogel formation, BSA was first stirred with an excess of DTT and Gdn-HCl to unfold the proteins, screen hydrophobic interactions that can cause irreversible aggregation, and expose free cysteines for crosslinking. We utilized a redox cycle previously discovered by Ogden *et al.*, which involves rapid oxidation of free thiol groups by H_2O_2 to form disulfide crosslinks between protein molecules, leading to a sol-to-gel transition. Slow concurrent reduction of the disulfide by DTT eventually severs all the crosslinks, inducing a gel-to-sol transition (Figure 3.1b).[211] Upon addition of H_2O_2, the solution initially became viscous and quickly formed a solid hydrogel after 1 – 10 minutes

depending on the DTT, H_2O_2, and denaturant concentrations (Figure 3.1c). The hydrogel self-degraded after 1 – 2 hours depending on the reagent concentrations. Here the emergence of transient hydrogel behavior occurs due to an oxidation reaction rate that is initially larger than the reduction reaction rate. We found that initial concentrations of 150 mM H_2O_2 and 200 mM DTT enabled reproducible dissipative assembly of the protein hydrogels with lifetimes that could be probed over reasonable experimental time scales.

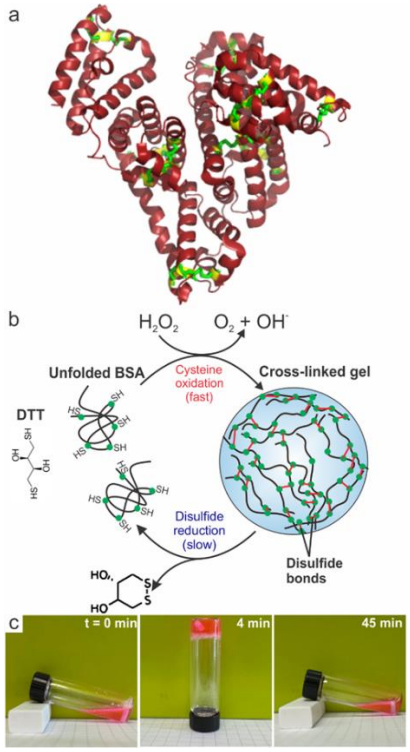

Figure 3.1. Formation of transient protein hydrogels using a redox cycle. (a) Crystal structure (PDB code: 3v03) of BSA with cysteine residues colored in yellow and disulfide bonds colored in green. (b) Schematic representation of the reactions involved in dissipative assembly of transient protein hydrogels. Black coils represent unfolded BSA, green dots are cysteine groups, and red lines are disulfide bonds. (c) Time-lapsed

images showing the formation and melting of a transient BSA hydrogel colored with rhodamine B.

3.3.2 Hydrogel lifetime measurements

DLS was used to probe hydrogel lifetime by tracking the diffusion rate of large aggregates (~1 μm) found to exist in the reduced BSA solution. Dark field optical microscopy imaging of a 90 mg/ml reduced, denatured BSA solution showed the presence of ~1 μm protein aggregates in solution prior to gel formation (Figure 3.2a). The nature and source of these protein aggregates is unclear, but could be due contaminant proteins in solution or proteins that misfolded and irreversible aggregated during lyophilization.[172,230] Imaging after gelation showed that the particles did not change size in the hydrogels. Figure 3.2b shows the DLS temporal autocorrelation curves for the BSA solution before addition of H_2O_2, 15 minutes after, and 30 minutes after. Species moving by Brownian motion in the liquid BSA solution (black curve) each present a unique exponential decay at a different time associated with their size and diffusion rate, where the characteristic decay time of a species increases with its size and the solution viscosity. The liquid BSA showed two exponential decays in the autocorrelation function near 10^{-1} ms and $10^{1.5}$ ms corresponding to BSA monomers and ~1 μm protein aggregates observed with microscopy, respectively. The decay time of the protein aggregates increased to $10^{4.5}$ ms 15 minutes after addition of H_2O_2, which corresponded to hydrogel formation and associated increase in solution viscosity. The hydrogel dissolved after 30 minutes and returned to the initial state as indicated by the autocorrelation function recovering the initial shape. Figure 3.2c plots the diffusion coefficients of each species before, during, and after hydrogel formation. Here, the

diffusion coefficient of the protein aggregates was ~10^{-9} cm^2/s prior to gelation, corresponding to a ~2 μm radius particle assuming spherical particles and the viscosity of water. After addition of H_2O_2 the diffusion coefficient of the protein aggregates decreased to ~$3*10^{-12}$ cm^2/s, which indicated solution viscosity increased nearly three orders of magnitude. After the hydrogel dissolved the diffusion coefficient distribution of the protein aggregates returned near the initial value. Taken together these measurements indicate DLS, and specifically the decay time of micron sized protein aggregates, can capture the hydrogel formation dynamics and lifetime. Here protein aggregates essentially serve as tracers of the sample viscosity over time. The time over which the protein aggregate decay time increased drastically corresponded well with visual observations of hydrogel lifetime. Rheology measurements are also presented below (Figure 3.3), allowing more precise identification of the gel-to-sol and sol-to-gel transitions and hydrogel mechanical properties.

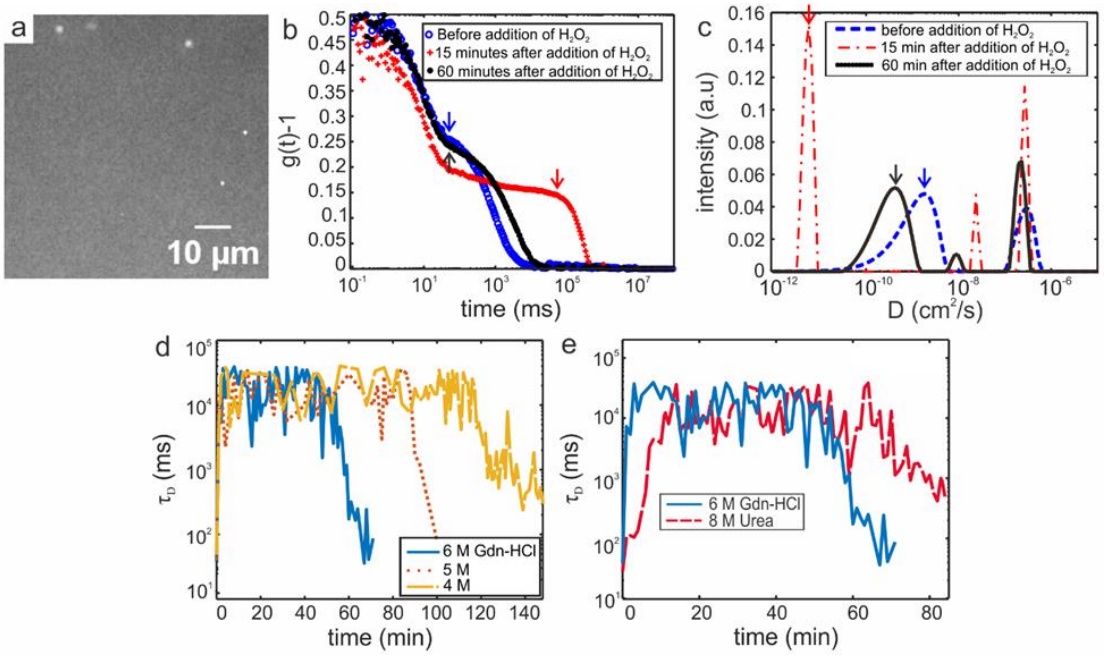

Figure 3.2. Measuring protein hydrogel lifetime using DLS and protein aggregate tracers. A) Dark field optical microscope image of micron sized protein aggregates in the BSA solution. B) DLS temporal autocorrelation curves of BSA solution in 6 M Gdn-HCl in liquid state (blue circles), 15 minutes after the addition of 150 mM H_2O_2 in gel state (red plus signs), and 60 minutes after addition of H_2O_2 in the liquid state (black stars). Arrows point to characteristic decay times (τ_D) for protein aggregates at each reaction time. C) Diffusion coefficient distribution of the BSA solution before gelation (blue dashed line), 15 minutes after gelation (red dashed line), and 60 minutes after addition of H_2O_2 in liquid state (black solid line). Arrows point to diffusion coefficients of protein aggregates at each reaction time. D) Decay time of protein aggregate tracers as a function of time for three different Gdn-HCl concentrations. e) Decay time of protein aggregate tracers as a function of time for 6 M Gdn-HCl and 8 M urea. Denaturants were included here at concentrations corresponding to full unfolding of the BSA.

We used DLS to measure the protein hydrogel lifetime as a function of Gdn-HCl concentration while holding H_2O_2 and DTT concentrations constant (Figure 3.2d). DLS measurements of the protein aggregate decay showed that each BSA solution rapidly formed a hydrogel within several minutes after which the decay time of the protein aggregates remained constant for the lifetime of the hydrogel. After a period of constant decay time corresponding to the hydrogel lifetime the decay time decreased over ~10 minutes to near the initial value, corresponding to melting of the hydrogel. Large fluctuations in the decay time were due to the short time over which the autocorrelation function was generated to enable time-dependent measurements of

decay time. Hydrogels formed with 6 M Gdn-HCl degraded the most rapidly and showed a precipitous decrease in decay time starting at ~60 minutes after fuel addition. As denaturant concentration was decreased, the lifetime of the protein hydrogel increased to ~80 minutes for 5 M Gdn-HCl and ~120 minutes for 4 M Gdn-HCl. We compared the hydrogel lifetime for two different denaturants, Gdn-HCl and urea, where urea is a less potent denaturant. Despite adding enough urea and Gdn-HCl to completely denature the BSA, Figure 3.2e shows that the hydrogel with urea formed more slowly compared to Gdn-HCl and had a longer lifetime of ~70 minutes compared to ~55 minutes for Gdn-HCl.

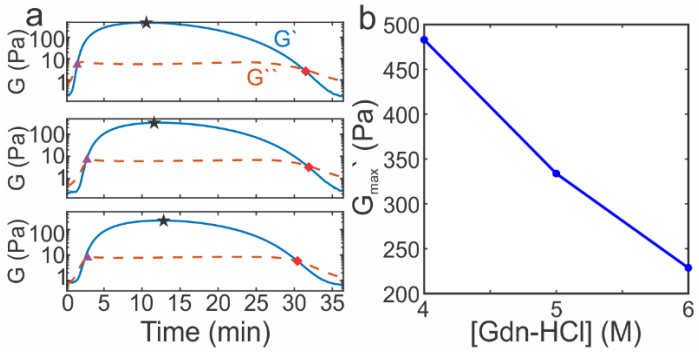

Figure 3.3. Time-dependent viscoelastic behavior of BSA hydrogels. a) The loss (G``) and storage (G`) moduli of the BSA solutions as a function of time after addition of 150 mM H_2O_2 at a constant shear rate of 1 rad/s and strain of 1%. The top plot is 6 M Gdn-HCl, the middle is 5 M Gdn-HCl, and the bottom is 4 M Gdn-HCl. Purple triangles mark the gelation time, black stars denote the maximum storage modulus reached by each hydrogel, and red diamonds mark the gel melting time. (b) The maximum storage modulus as a function of Gdn-HCl concentration.

3.3.3 Viscoelastic Properties of Hydrogels

Figure 3.3a shows the storage (G`, blue solid line) and loss (G``, dashed orange line) moduli of the hydrogels for 6 M (top), 5 M (middle), and 4 M (bottom) Gdn-HCl. Here the storage modulus measures the elastic, or solid, properties of the sample, while the loss modulus measures the viscous, or liquid properties, of the sample. A liquid sample has a larger loss modulus than storage modulus (G`` > G`) and vice versa for a solid sample. The crossover between these two regimes corresponds to a sol-to-gel transition. The storage and loss moduli were observed to initially increase monotonically over time with the gelation time increasing as a function of Gdn-HCl concentration. The 6 M Gdn-HCl sample formed a gel more rapidly than the other concentrations with the sol-to-gel transition occurring after 81 seconds, while it occurred at 147 seconds and 123 seconds for the 5 M and 4 M Gdn-HCl samples, respectively. After gelation the storage modulus reached a peak value, G_{max}`, and then decay until the gel dissolved. The 6 M Gdn-HCl hydrogel reached its maximum storage modulus most rapidly, followed by the 5 M and 4 M samples. In contrast to the DLS measurements each gel degraded at about the same time after ~30 minutes. The maximum achieved storage moduli of the hydrogels was observed to decrease by nearly 100% when decreasing the Gdn-HCl concentration from 6 M to 4 M (Figure 3.3b). The difference between the hydrogel lifetimes measured by DLS and rheology was due to the different sample geometries. DLS and visual observations were performed on samples in cuvettes open to atmosphere, which allowed oxygen exchange with the surrounding air while rheology was performed in an enclosed solvent trap to prevent evaporation. Atmospheric oxygen can extend the lifetime of the hydrogel by competing

with the disulfide reduction reaction, so the hermetically sealed solvent trap shorted hydrogel lifetimes and caused similar lifetimes for each denaturant concentration. We note that despite the shorter hydrogel lifetimes the rheology showed qualitative agreement with DLS and visual observations, as the 6 M Gdn-HCl gelled first and began to degrade prior to the lower concentrations.

3.3.4 Protein Unfolding and Solvent Exposed Cysteine

We used intrinsic tryptophan fluorescence to measure the unfolding of a 1 mg/ml BSA solution with 90 mg/ml dextran included as a crowding agent (Figure 3.4a, see location of tryptophan groups in the inset BSA crystal structure). Intrinsic fluorescence indicated the BSA was unfolded above a Gdn-HCl concentration of 3 M, but the intrinsic fluorescence emission continued to decrease approximately linearly over the range of 4 – 6 M (Figure 3.4a, see inset zoomed in plot). Prior work showed that chemical unfolding of human serum albumin occurred sequentially with increasing denaturant concentration because each secondary structure motif had different sensitivity to chemical denaturants.[231] Therefore, the decrease in intrinsic fluorescence above 4 M Gdn-HCl could be due to further unfolding of secondary structures that are less susceptible to chemical denaturation. Decreased fluorescence emission from the hydrophobic dye ANS was observed when increasing denaturant concentration from 4 – 6 M (Figure 3.4b). ANS binds hydrophobic residues, which increases its fluorescence emission, indicating that increasing the Gdn-HCl concentration screened hydrophobic interactions between ANS and buried hydrophobic residues. Ellman's assay measurements showed that increasing the Gdn-HCl concentration also increased the solvent accessible cysteine concentration and the percent of cysteines crosslinked in

the protein hydrogels (Figure 3.4c and inset). The increased crosslinking as a function of increasing denaturant concentration explains the increase in the maximum storage modulus of the hydrogels (*cf.* Figure 3.3b). Interestingly, the ~30% increase in free cysteine concentration when increasing the Gdn-HCl concentration from 4 M to 6 M was similar to the percent decrease in the intrinsic tryptophan fluorescence and the percent decrease in the ANS fluorescence emission over the same range. Taken together, these findings indicate that increasing the denaturant concentration above the main unfolding transition unfolds residual secondary structure, which exposes buried disulfide bonds that are converted to free cysteines in the starting protein solution.

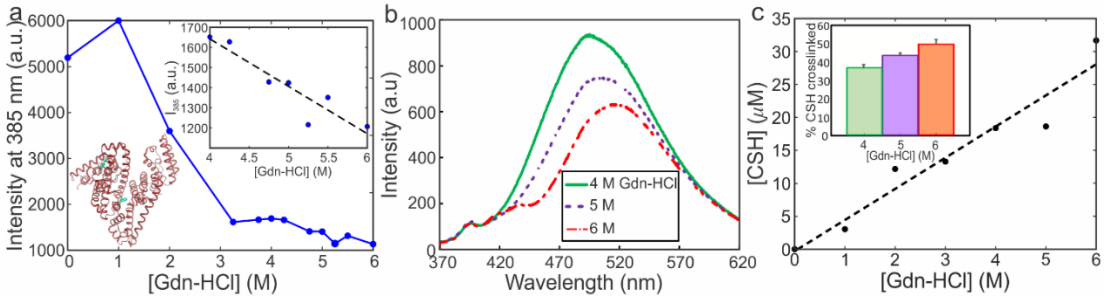

Figure 3.4. BSA unfolding increases the solvent accessible cysteine group concentration and the disulfide crosslinking density. (a) Intrinsic tryptophan fluorescence of a 1 mg/ml BSA, 90 mg/ml dextran 70, 200 mM DTT solution as a function of Gdn-HCl concentration. Top right inset: Zoomed in plot showing the linear decrease in the intrinsic fluorescence above 4 M Gdn-HCl. Bottom left inset: Crystal structure of BSA showing the location of the tryptophan residues in blue. (b) Fluorescence emission spectra of ANS from a 1 mg/ml BSA solution for three difference Gdn-HCl concentrations. (c) The concentration of solvent exposed cysteines ([CSH]) as a function of Gdn-HCl concentration. The inset shows the percent of free cysteines crosslinked in a hydrogel as a function of Gdn-HCl concentration.

3.3.5 H_2O_2 consumption rate

The exposure of additional cysteine groups with increasing Gdn-HCl concentration suggests a mechanism for the effect of protein denaturation on the hydrogel lifetime. At relatively high Gdn-HCl concentrations a larger concentration of cysteine groups are available to react with H_2O_2, which more rapidly depletes the fuel and shortens the hydrogel lifetime. To test this proposed mechanism, we utilized a redox-sensitive dye, resazurin, which exhibits strong fluorescence in its oxidized state (resofurin) and weak fluorescence in the reduced state (dihydroresofurin). In the presence of competing oxidation and reduction reactions, the fluorescence emission is an indicator of whether there is a net oxidizing or reducing environment in solution. Figure 3.5a shows time lapsed macroscopic fluorescence images acquired of a BSA/DTT solution in a cuvette containing resazurin with H_2O_2 added immediately prior to the first image. It can be clearly seen that the fluorescence emission was highest initially, indicating an oxidative environment. The fluorescence intensity decayed over time due to resofurin reduction by DTT, indicating a net reducing environment and depletion of H_2O_2. It is noteworthy that the fluorescence emission was not uniform throughout the sample and remained higher near the surface due the oxidation of dihydroresofurin to resofurin by atmospheric oxygen. Figure 3.5b shows the ensemble fluorescence emission from resofurin as a function of time after addition of H_2O_2 to BSA solutions with different Gdn-HCl concentrations. The fluorescence emission was observed to rapidly increase over ~10 seconds after addition of H_2O_2 followed by a maximum and then steady decay over hundreds of seconds. The peak in fluorescence intensity occurred at the shortest time after fuel addition for 6 M Gdn-HCl and

increased as the denaturant concentration was decreased. Likewise, the fluorescence of the 6 M Gdn-HCl sample decayed most rapidly, indicating that H_2O_2 was consumed most rapidly in this sample in support of the proposed mechanism.

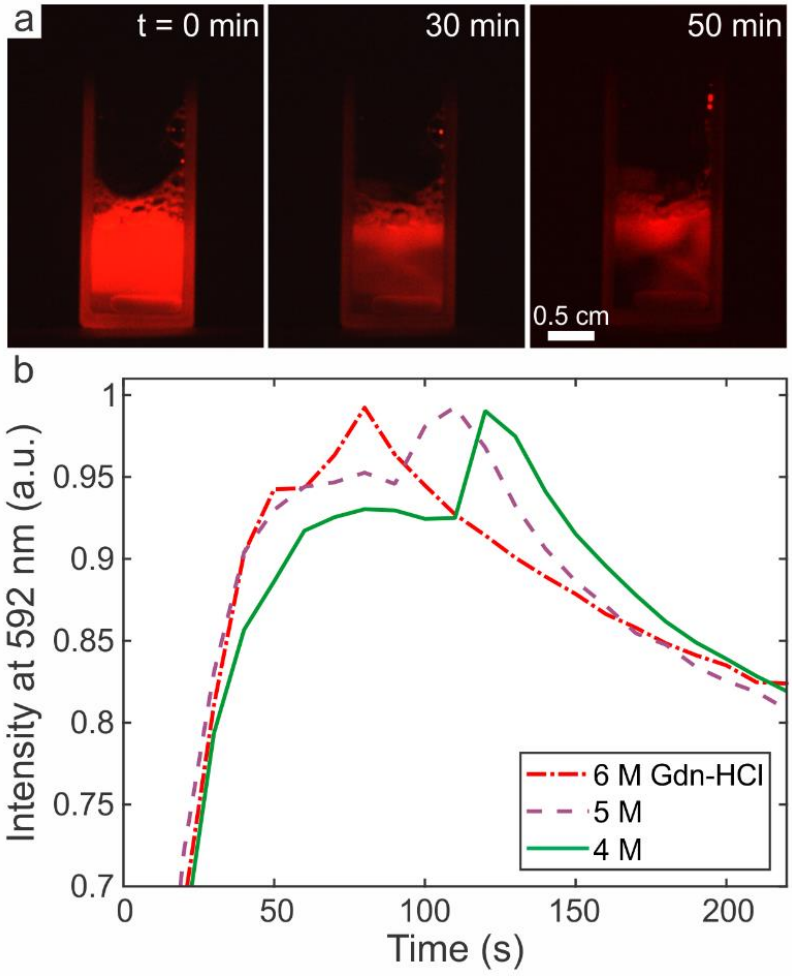

Figure 3.5. Fluorescence imaging and spectroscopy measurements of the redox environment in the transient hydrogels. a) Macroscale fluorescence images of a hydrogel in 6 M Gdn-HCl buffer upon addition of H_2O_2 at t = 0, 30 min after addition of H_2O_2 (gel state), and 50 minutes after the addition of H_2O_2 (liquid state). B) Time-lapsed fluorescence intensity measurements at 592 nm of BSA/DTT solutions of different Gdn-HCl concentration after addition of H_2O_2. The fluorescence intensities

for each sample was normalized to the maximum intensity in that data set. Noise in the fluorescence emission curves near the peak intensity of each time series was attributed to spatially fluctuating fluorescence in the hydrogel as shown in Figure 3.5a.

3.3.6 Varying the Redox Reaction Rates

Additional experiments varying the DTT and H_2O_2 concentrations during dissipative assembly further supported the idea that the H_2O_2 consumption was mediated by the unfolding state, cysteine group concentration, and the DTT concentration. Figure 3.6a shows time dependent DLS decay time measurements for two hydrogels formed with different DTT concentration. Increasing the DTT concentration at constant denaturant concentration from 200 mM to 260 mM, a 30% increase, increased the hydrogel lifetime by about 40%. In this case, the higher concentration of DTT, or larger DTT:H_2O_2 ratio, established a net reducing condition more quickly due to the increased reaction rate between DTT and disulfide bonds. Figure 3.6b shows that the hydrogel lifetime depended on the H_2O_2:cysteine concentration ratio. A hydrogel formed with 5 M Gdn-HCl and 150 mM H_2O_2 had a lifetime of ~70 minutes while a hydrogel with 6 M Gdn-HCl and the same fuel concentration had a lifetime of ~30 minutes, about 2.3 times shorter. The cysteine concentration decreased by a similar factor when decreasing the Gdn-HCl concentration from 6 M to 5 M (*c.f.*, Figure 3.4c). The lifetime of the 5 M Gdn-HCl hydrogel could be effectively decreased below the 6 M Gdn-HCl hydrogel by decreasing the H_2O_2 concentration. These results highlight that the DTT:H_2O_2 and H_2O_2:cysteine ratios dictated the lifetime of the hydrogel with Gdn-HCl concentration controlling the cysteine concentration.

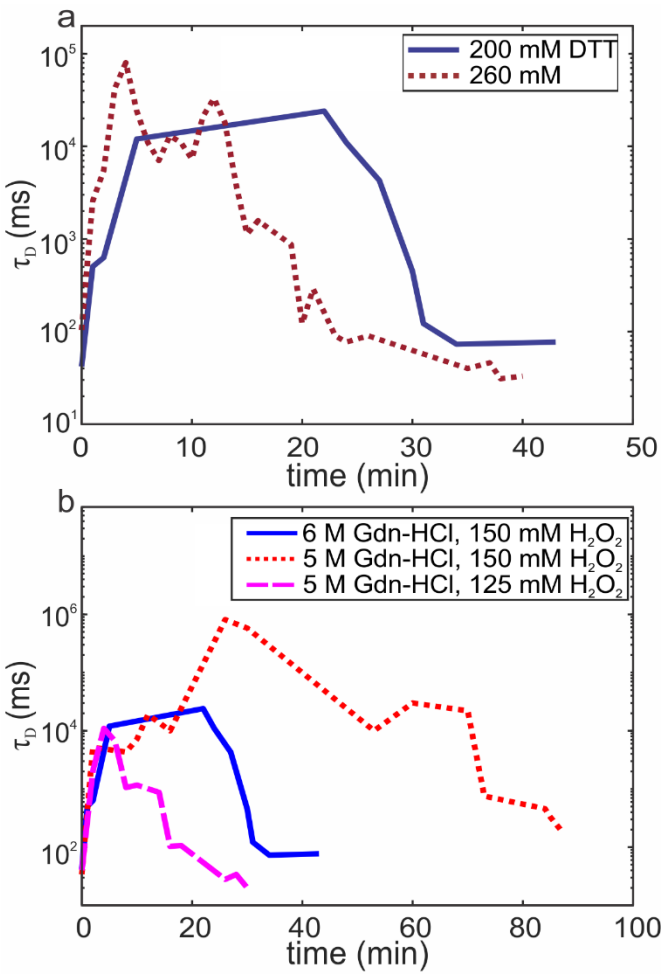

Figure 3.6. Impact of DTT and H_2O_2 concentrations on hydrogel lifetime. A) Decay time of protein aggregate tracers as a function of time for two different DTT concentrations. b) Decay time of protein aggregate tracers as a function of time for different H_2O_2 and Gdn-HCl concentrations.

3.3.7 Mechanism for The Effect of Protein Unfolding on Dissipative Assembly

To summarize our results, increasing the Gdn-HCl concentration in the BSA/DTT solutions decreased hydrogel lifetime and increased storage modulus. Fluorescence spectroscopy measurements showed increased solvent exposure of tryptophan groups in the BSA when increasing the Gdn-HCl concentration from 4 M to 6 M despite the main unfolding transition occurring between 2 M and 3 M Gdn-HCl.

ANS binding indicated that buried hydrophobic groups were screened when increasing Gdn-HCl from 4 M to 6 M, further indicating that additional unfolding and exposure of hydrophobic residue occurred over this concentration range. Unfolding of residual secondary structure was accompanied by an increase in solvent accessible cysteine concentration and an increased percentage of crosslinked cysteines in the hydrogels. The 3D structure of BSA with the cysteine groups denoted as blue spheres and hydrophobic surface patches overlaid in red illustrates that cysteine groups exist in regions with diverse hydrophobicity and thus variable susceptibility to chemical denaturation (Figure 3.7a)[232]. The relative solvent accessible surface area (RASA) of the BSA sequence quantifies the local sequence hydrophobicity, where hydrophobic amino acids have low RASA, and further illustrates that cysteines exist in a range of polar and non-polar regions within the amino acid sequence (Figure 3.7b)[233]. Cysteines in hydrophilic sequence regions were exposed to solvent at relatively low Gdn-HCl concentrations while those in buried hydrophobic regions were exposed to solvent at higher Gdn-HCl concentration. Increasing exposure of cysteine groups with increasing denaturation concentration created additional crosslinking reaction sites, leading to more rapid depletion of H_2O_2 during dissipative assembly and decreased the hydrogel lifetime. Increased concentrations of free cysteines at higher denaturant concentrations is also consistent with increased hydrogel stiffness and crosslinking density (Figure 3.7c). Overall, this work indicates that a general feature required for the emergence of unfolding dependent protein hydrogel lifetime is that disulfide bonds are located on regions of the folded protein with variable solvent accessibility. This feature provides

continuous supply of additional cysteine crosslinking sites as the denaturant concentration is increased.

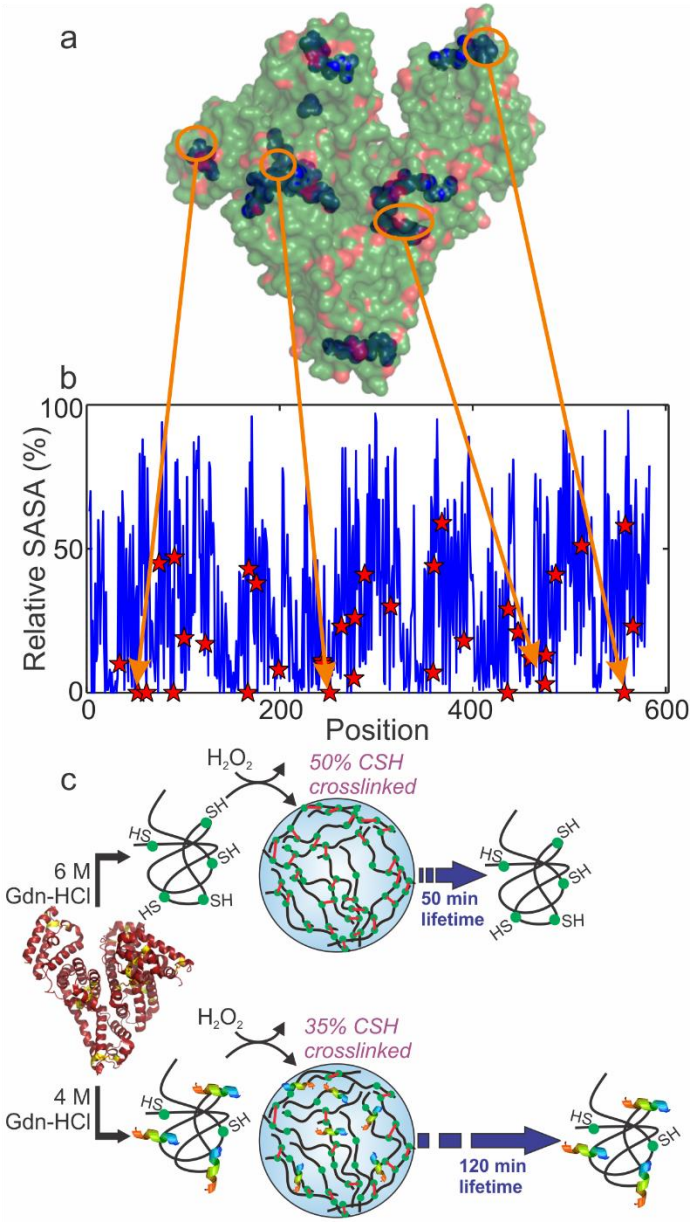

Figure 3.7. Location of cysteine groups in hydrophobic and hydrophilic regions and the impact on dissipative assembly. (a) Protein surface hydrophobicity map derived from the 3D crystal structure of BSA with the red color corresponding to hydrophobic surface regions, green color corresponding to hydrophilic surface regions, and blue

spheres corresponding to cysteine residues. (b) Relative solvent accessible surface area (SASA) of the BSA sequence. Orange arrows highlight a few cysteine groups in the 3D structure and amino acid sequence that exist in hydrophobic regions. (c) Schematic illustration of the overall mechanism explaining the effect of Gdn-HCl concentration and protein unfolding on dissipative assembly of protein hydrogels

3.4 Conclusions

Here we used BSA and a redox reaction cycle to form transient hydrogels that displayed lifetime and stiffness that were dependent on unfolding of the protein. This work demonstrates that biological macromolecules can be building blocks for synthetic dissipative assembly of transient hydrogels and that their hierarchical structure exerts control over the reaction kinetics. Experiments showed that denaturant concentration mediated exposure of cysteine crosslinking sites that in turn mediated crosslinking density, mechanical properties, and hydrogel lifetime. Increasing the denaturant concentration decreased hydrogel lifetime, increased stiffness, and increased crosslinking density. The underlying mechanism was identified to be denaturant concentration dependent solvent exposure of cysteine sites on the BSA. This study demonstrates overall the impact that protein structure, even in predominantly unfolded proteins, can exert on dissipative assembly kinetics and represents a first step in realizing synthetic dissipative assembly systems that take advantage of the incredible function and hierarchical structure of proteins. This work suggests that other biological molecules that display hierarchical structuring, such as DNA, protein fibrils, and enzymes, can be used as a building block for dissipative assembly.

Chapter 4: Enhanced Recombinant Production and Purification of Beta 2-microglobulin using SUMO as a Soluble Partner

Abstract

This chapter describes the results of expressing Beta 2-microglobulin in E. coli using conventional methods and using a soluble partner to enhance refolding. In the absence of a soluble folding particle, Beta 2-microglobulin aggregated into inclusion bodies during expression and refolding and purification led to the aggregation of a considerable proportion of the purified protein. The labeling efficiency of the protein for single molecule fluorescence resonance energy transfer (FRET) and fluorescence correlation spectroscopy (FCS) was relatively low. Although the two-step refolding process suggested by Geisbrecht et al.[234] prevented formation of visible aggregates, size exclusion chromatography (SEC) and analytical ultracentrifugation (AUC) indicated the presence of oligomeric aggregates of the MW about 70,000 Da and the size between 10 – 20 nm radius. To address this challenge, we generated fusion proteins of Beta-2 microglobulin and a refolding partner, small ubiquitin-related modifier (SUMO). Similar to the native protein, the resulting fusion protein was expressed primarily in exclusion bodies. However, the fusion protein showed little to no aggregates upon refolding and the fluorescence labeling. We expect that this expression and purification method will enable expressing higher concentrations of monomeric small proteins, which is critical for amyloid formation and single molecule fluorescence studies.

4.1 Introduction

Initial aggregate-free solutions of proteins are critical for studies of amyloid formation, protein conformation, oligomerization, and pharmaceutical applications of proteins. Special attention should be paid to enhancing the refolding of recombinant proteins to investigate their properties without oligomerization or aggregation. In particular, removing nucleation seeds consisting of small oligomers or aggregates is crucial for kinetic investigations of amyloid nucleation and growth.[235,236] Likewise, high concentrations of monomeric solutions of proteins are required for single molecular fluorescence measurements[237]. This dissertation research aims to investigate the conformational fluctuations in the structure of the amyloid-forming protein Beta 2-microglobulin (β_2M) using single-molecule Forster resonance energy transfer (smFRET) and fluorescence correlation spectroscopy (FCS). For these experiments, we require highly monomeric and relatively high concentrations of protein for efficient site-specific labeling of proteins and for reliably separating equilibrium oligomerization from the conformational motion of the protein structure.

4.2 Methods

4.2.1 Plasmid Construction

4.2.1.1 Construct 1 (6xHis-TEV-B_2M)

In the first attempt for recombinant production of our target protein, the DNA encoding with two cysteine mutants for fluorescent dye labeling on both ends was synthesized commercially at the Genewiz and cloned into the expression plasmid pET-42(a). The plasmid contains a 6x-Histidine tag (6xHis) on its C-terminus. The construct (Figure 4.1) had a 6x-Histidine tag and a Tobacco Etch Virus (TEV) proteolytic

cleavage site (Glu-Asn-Leu-Tyr-Phe-Gln-Gly) in addition to the gene encoding the β_2M. All constructs contain a kanamycin resistance selection marker. The gene encoding β_2M with cysteine mutations is:

AATGGCAAATCCAATTTTCTGAATTGCTATGTGTCCGGCTTTCATCCGTCC
GATATTGAAGTGGATCTGCTGAAAAATGGCGAACGTATTGAAAAAGTGG
AACATTCCGATCTGTCCTTTTCCAAAGATTGGTCCTTTTATCTGCTGTATTA
TACCGAATTTACCCCGACCGAAAAAGATGAATATGCGTGCCGTGTGAATC
ATGTGACCCTGTCCCAGCCGAAAATTGTGAAATGGGATCGTGATTGCTGA.

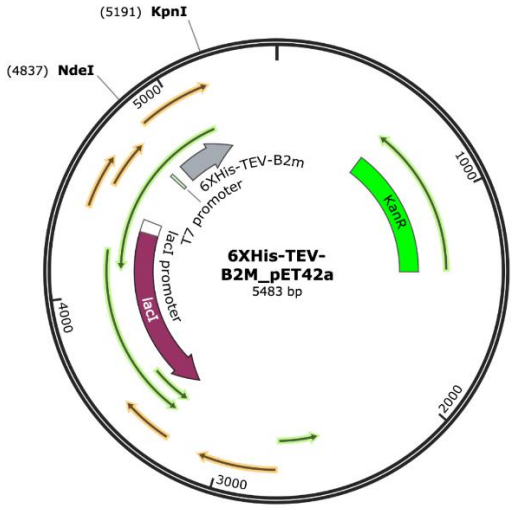

Figure 4.1. Plasmid map of 6xHis-TEV-B_2M**.** Plasmid was created with pET-42(a) as the backbone. NdeI and KpnI are cut sites.

4.2.1.2 Construct 2 (6xHis-SUMO-B_2M)

To enhance the efficiency and quality of the purified β_2M, SUMO was added to the construct and the TEV sequence was removed. The Gibson Assembly (GA) technique was used for the construction of this plasmid. The pEt23(a) vector containing the DNA encoding SUMO (From *Saccharomyces Cereviase*) was a gift from Professor

Jinwoo Lee's laboratory. The DNA fragment encoding SUMO with an overlapping end for GA was PCR amplified from the pET23(a) plasmid using primers 1&2 (P_1, P_2 in Table 4.1). The DNA encoding the pET42(a) vector with overlapping ends was amplified using primers 3&4 (P_3, P_4 in Table 4.1). After the PCR amplifications, the PCR products were cleaned and loaded on a DNA gel to confirm their amplification and correct length (Figure 4.2). The two amplified fragments were assembled in one single step using the New England Biolabs (NEB) GA kit. The resulting new vector containing the protein-encoding genes, the GA steps, and the DNA gel showing the success of the GA is presented in Figure 4.3. At the lower end of Figure 4.3 (a), the vector containing the $\beta_2 M$ encoding gene and the fragment containing the SUMO encoding genes, which were PCR-amplified are shown. The vector and fragment further assembled by the enzymes provided in the kit and the resulting plasmid is shown in the upper part of Figure 4.3 (a). Part b and c of the Figure 4.3 represent the DNA gel ran for the final GA product and the successful transformation of the plasmid into the expression *E. coli* strain (Nico 21(DE3)) respectively.

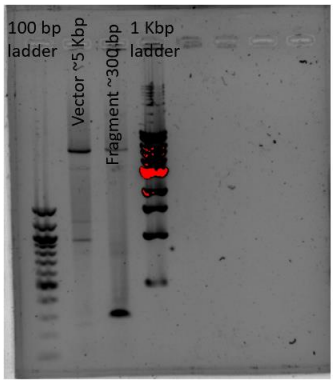

Figure 4.2. PCR product for GA loaded on DNA gel. The PCR products for the $\beta_2 M$ vector and the SUMO fragment shows the correct molecular weight when compared to the DNA ladders.

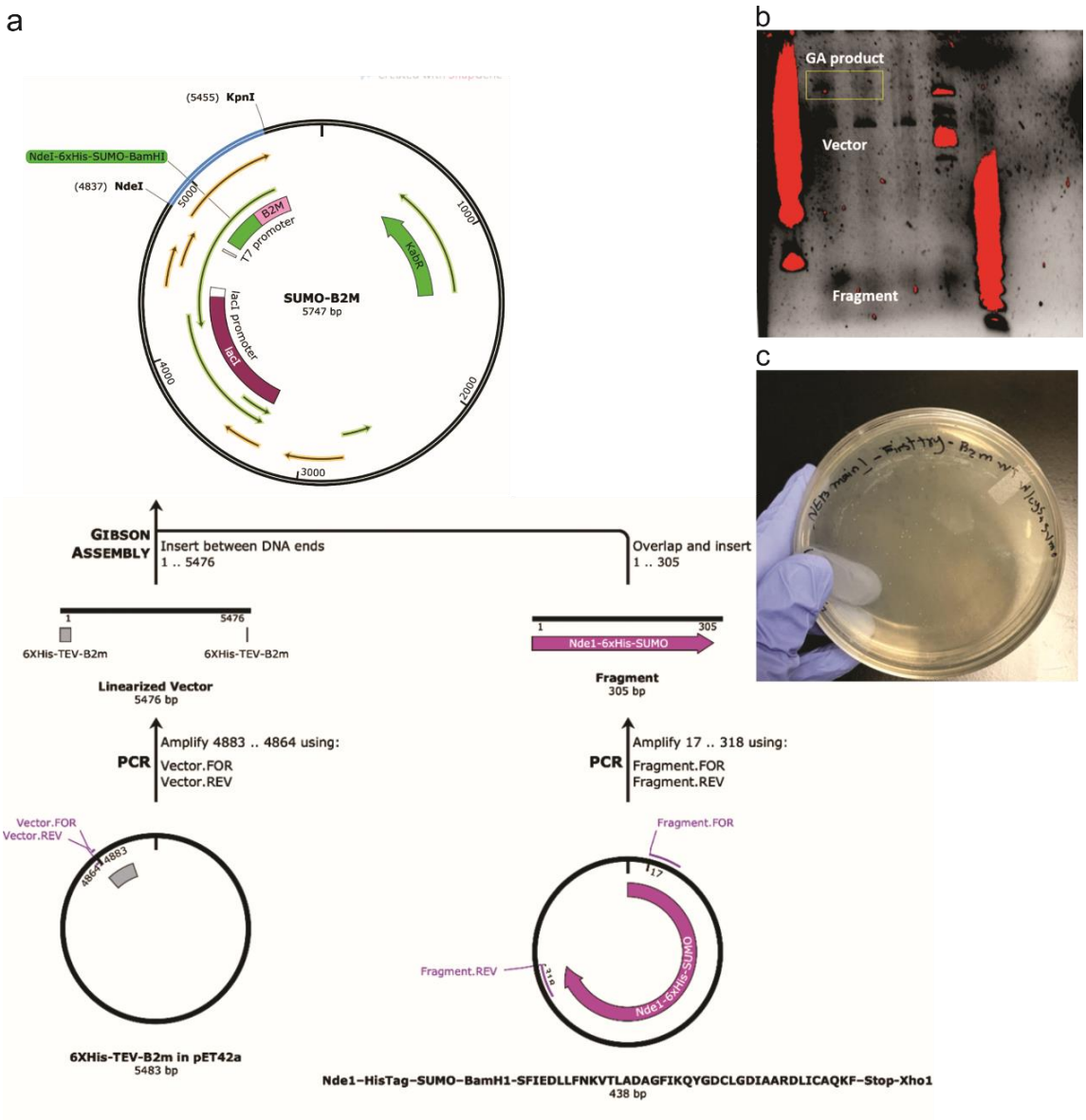

Figure 4.3. (a) Schematic description of the Gibson Assembly steps. (b) Final plasmid map of the modified vector containing SUMO as soluble partner. (c) DNA gel of Gibson assembly product. (d) plate containing the colonies of *E. coli* containing the SUMO-modified plasmid constructed by GA, the sequences were confirmed by the Sanger sequencing.

Table 4.1 List of synthesized oligonucleotides (primers) for the construction of 6xHis-SUMO_B2M used in this study

Name	sequence
Sumo fragment Forward_P1	ACCATCACAGCGATAGCGAGGT
Sumo fragment Reversed_P2	CTGAATGCAGGATCCACCGATTTGCTCACG
β_2M vector Forward_P3	GTGGATCCTGCATTCAGCGTACCCCG
β_2M vector Reversed_P4	GCTATCGCTGTGATGGTGATGGTGATGCATATGTATATCT

4.2.2 Site Directed Mutagenesis

The Thermofisher site directed mutagenesis kit was used for modification of β_2M encoding gene to produce D76N mutant using a forward primer (GACCGAAAAAAACGAATATGCGTGC) and reverse primers (GGGGTAAATTCGGTATAATACAGCAGATAAAAG). The $\Delta N6$ mutant and the original β_2M gene (without cysteine modification) was ordered to be synthesized by Genewiz. The nucleic acid sequences of wild-type and mutant β_2M is presented below.

1- Wild type β_2M:

CATATGCATCACCATCACCATCACAGCGATAGCGAGGTGAACCAGGAAG
CGAAGCCGGAAGTGAAACCGGAAGTTAAGCCGGAGACCCACATCCTGA
AAGTTAGCGACGGTAGCAGCGAAATCTTCTTTAAGATTAAGAAAACCACC
CCGCTGCGTCGTCTGATGGAAGCGTTCGCGAAACGTCAGGGCAAGGA
GATGGACAGCCTGCGTTTTCTGTACGATGGCATCCGTATTCAGGCGGACC
AAACCCCGGAAGACCTGGATATGGAGGACGATATCATTGAAGCGCAC
CGTGAGCAAATCGGTGGATCCATTCAGCGTACCCCGAAAATTCAGGTGTA
TTCCCGTCATCCGGCGGAAAATGGCAAATCCAATTTTCTGAATTGCT

ATGTGTCCGGCTTTCATCCGTCCGATATTGAAGTGGATCTGCTGAAAAATG
GCGAACGTATTGAAAAAGTGGAACATTCCGATCTGTCCTTTTCCAA
AGATTGGTCCTTTTATCTGCTGTATTATACCGAATTTACCCCGACCGAAAA
AGATGAATATGCGTGCCGTGTGAATCATGTGACCCTGTCCCAGCCG
AAAATTGTGAAATGGGATCGTGATTGAGGTACC.

2- $\Delta N6\ \beta_2 M$:

CATATGCATCACCATCACCATCACAGCGATAGCGAGGTGAACCAGGAAG
CGAAGCCGGAAGTGAAACCGGAAGTTAAGCCGGAGACCCACATCCTGA
AAGTTAGCGACGGTAGCAGCGAAATCTTCTTTAAGATTAAGAAAACCACC
CCGCTGCGTCGTCTGATGGAAGCGTTCGCGAAACGTCAGGGCAAGGA
GATGGACAGCCTGCGTTTTCTGTACGATGGCATCCGTATTCAGGCGGACC
AAACCCCGGAAGACCTGGATATGGAGGACGATATCATTGAAGCGCAC
CGTGAGCAAATCGGTGGATCCTGCATTCAGGTGTATTCCCGTCATCCGGC
GGAAAATGGCAAATCCAATTTTCTGAATTGCTATGTGTCCGGCTTTC
ATCCGTCCGATATTGAAGTGGATCTGCTGAAAAATGGCGAACGTATTGAA
AAAGTGGAACATTCCGATCTGTCCTTTTCCAAAGATTGGTCCTTTTA
TCTGCTGTATTATACCGAATTTACCCCGACCGAAAAAGATGAATATGCGT
GCCGTGTGAATCATGTGACCCTGTCCCAGCCGAAAATTGTGAAATGG
GATCGTGATTGCTGAGGTACC.

3- D76N $\beta_2 M$:

CATATGCATCACCATCACCATCACAGCGATAGCGAGGTGAACCAGGAAG
CGAAGCCGGAAGTGAAACCGGAAGTTAAGCCGGAGACCCACATCCTGA

AAGTTAGCGACGGTAGCAGCGAAATCTTCTTTAAGATTAAGAAAACCACC
CCGCTGCGTCGTCTGATGGAAGCGTTCGCGAAACGTCAGGGCAAGGA
GATGGACAGCCTGCGTTTTCTGTACGATGGCATCCGTATTCAGGCGGACC
AAACCCCGGAAGACCTGGATATGGAGGACGATATCATTGAAGCGCAC
CGTGAGCAAATCGGTGGATCCATTCAGCGTACCCCGAAAATTCAGGTGTA
TTCCCGTCATCCGGCGGAAAATGGCAAATCCAATTTTCTGAATTGCT
ATGTGTCCGGCTTTCATCCGTCCGATATTGAAGTGGATCTGCTGAAAAATG
GCGAACGTATTGAAAAAGTGGAACATTCCGATCTGTCCTTTTCCAA
AGATTGGTCCTTTTATCTGCTGTATTATACCGAATTTACCCC**AAT**CGAAAA
AGATGAATATGCGTGCCGTGTGAATCATGTGACCCTGTCCCAGCCG
AAAATTGTGAAATGGGATCGTGATTGAGGTACC.

4.2.3 Protein Expression in Bacterial Strains

We transformed the plasmids into Thermo Scientific DH10B chemically competent cells suitable for high-efficiency cloning. Three colonies were selected from the agar plate and were grown overnight in the presence of kanamycin. The DNA plasmids were extracted from the overnight grown cultures using GeneJET Plasmid Miniprep Kit (Thermofisher) and were sent to Genewiz for Sanger sequencing. After confirming the DNA sequences, the plasmids were transformed into NiCo21(DE3) Competent E. coli from NEB, which are engineered for an improved purity of target proteins isolated by immobilized metal affinity chromatography (IMAC).

For all the variants and constructs, 10 mL of overnight culture was subcultured into 1 liter of Luria-Bertani broth containing 30 ug/mL kanamycin. After incubation with shaking in 37 ◦C for 2.5 hours or when the optical density (OD) 600 reached 0.4-

0.8, Isopropyl β-D-1-thiogalactopyranoside (IPTG) was added to the cultures to a final concentration of 100 μM. After induction of protein expression, the cultures stayed overnight at 37 C in the shaker incubator.

4.2.4 Protein Extraction, Purification, and Refolding from Inclusion Bodies

Since the cytoplasm of *E. coli* is not a favorable environment for folding β_2M after its expression, β_2M aggregates into inclusion bodies upon expression. The cells were harvested by centrifugation at 4200 xg at 4 C. The harvested cells were then frozen and thawed to increase lysis efficiency. The thawed bacteria containing our target protein were resolubilized in the lysis buffer, which contained 50 mM tris-HCl pH 8, 25 mM NaCl, 2 mM EDTA, 0.1% TritonX-100, protease inhibitor cocktail (VWR), and 1 mg/mL lysozyme. The lysis solution was incubated in a 37 C water bath for 30 minutes. A French press homogenizer cell disruption system (Avestin) was used to further lyse the bacterial cell walls. 10 uL of benzonase nuclease (Sigma) was added to reduce the viscosity of the solution. Cells were further lysed with two passes through the French press operated at 18,000 to 20,000 psi. The cells were chilled by an ice water bath between each pass. The lysed cells were clarified by centrifuging 1 hr at 12500 x g (Beckman X30R centrifuge). The supernatant was decanted and the pelleted inclusion bodies and cell debris were collected. Pellets were suspended in 30 mL of pellet wash buffer containing 50 mM Tris-HCl pH 8, 5 mM EDTA, 2 M urea, 5 mM DTT, and 1% (w/v) Triton X-100 and homogenized using a probe sonicator. The homogenized pellets then were centrifuged at 12000 xg and the supernatant was decanted. The washing step was repeated three times, and for the one last wash, urea and Triton X-100 were excluded from the wash buffer.

For the purification using IMAC, the washed inclusion bodies were first re-suspended and incubated in denaturing buffer containing 6 M Guanidine-HCl, 100 mM Tris (pH 8.0), and 10 mM Imidazole overnight in 4 C with rotation. The re-suspended pellet was centrifuged at 12,500 x g to separate the remaining cell debris from the wash step. The re-suspended pellet was run over a nickel(II) nitriloacetate (Ni-NTA) liquid chromatography column under denaturing conditions. The denaturing equilibration and washing buffer contained 20 mM sodium phosphate (pH 6.5), 0.5 M NaCl, 10 mM Imidazole and 8 M Urea. Proteins were washed with 10 column volumes of washing buffer to separate the unwanted contaminating proteins. Purified β_2M was eluted with 2.5 column volumes of 20 mM sodium phosphate (pH 6.5), 0.5 M NaCl, 0.2 M Imidazole, 8 M Urea.

Three-step dialysis was used for refolding and cleavage of β_2M from either 6xHis-TEV or 6xHis-SUMO[234]. For the first step, the eluted fraction from the Ni-NTA column was dialyzed overnight in 2 L of 100 mM Tris (pH 8.6), 1 mM EDTA, 20 mM glycine, 2.5 M urea, and 1 mM L-cysteine. The second step was a 5-hour dialysis in 2 L of phosphate-buffered saline (PBS, pH 7.4). The third step was to dialyze the protein in 2 L of Ni-NTA binding buffer and add the TEV or SUMO protease plus DTT to provide a reducing condition for efficient cleavage. For separating cleaved β_2M from SUMO and 6xHis tag, the digested purified β_2M was added to a preequilibrated Ni-NTA column. The flow through of the column was collected and went through a final purification step over a HiLoad 16/600 Superdec 75 pg column (Cytiva life sciences).

4.3 Results and Discussion

4.3.1 Comparison of $\beta_2 M$ from the two constructs and challenges

There were numerous challenges in purifying $\beta_2 M$. The first challenge was the refolding process of $\beta_2 M$ from inclusion bodies. Most of the purified $\beta_2 M$ aggregated and precipitated upon dialysis in the native refolding buffer (40 mM Tris-HCl, pH 8) taken from a prior literature protocol[238]. We have tried several refolding methods, such as stepwise refolding and dilution. However, neither of the protocols resulted in a clear and aggregate-free solution of protein after refolding. Finally, on the advice of Dr. Jordan Woehl[234], we used his suggested three-step refolding protocol explained in section 4.2.4, which was a success. However, despite the clarity of the solution, mesoscale aggregates detected by AUC and SEC was presented along with monomers in the solution (Figures 4.5 and 4.6). The second construct containing a soluble partner fusion protein, SUMO, resolved the aggregation issue, which will be explained in detail in the following sections.

4.3.1.1 Comparison of expression level in soluble and insoluble fractions

Figure 4.4 presents the Western blot (before the purification) and the SDS-PAGE gel of the purified protein. As shown in Figure 4.4, the soluble fraction of the lysate contained no $\beta_2 M$. The most probable reason for the lack of $\beta_2 M$ presence in the soluble fraction E. coli lysate is the reducing environment in the cytoplasmic space of *E. coli*[239]. Since $\beta_2 M$ is disulfide bond-stabilized, the reducing environment in the cytoplasm prevents the formation of these bonds and makes it difficult for $\beta_2 M$ to fold correctly. Therefore, even in the presence of the folding enhancer SUMO, the lack of a

favorable folding environment for $\beta_2 M$ in the *E. coli* cytoplasm this protein does not refold upon expression, hence, together with its partner, SUMO, aggregates into inclusion bodies.

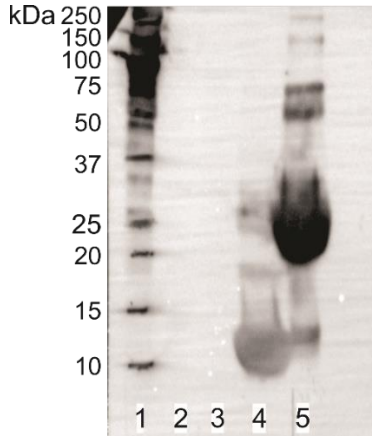

Figure 4.4. Western Blot comparing the soluble and insoluble expression of $\beta_2 M$ when expressed in isolation (rows 2 and 4) and when expressed with SUMO as a soluble expression partner (rows 3 and 5). As shown, none of the constructs were able to produce a protein in the soluble state (rows 2 and 3).

4.3.1.2 Comparison of Aggregation and Cleavage Efficiency

Even though the two-step refolding enhanced the refolding of $\beta_2 M$ when there was not any soluble partner fused to it, size exclusion chromatography (SEC) and analytical ultra-centrifugation (AUC) indicated the presence of soluble oligomers in purified and refolded $\beta_2 M$ solutions. In Figure 4.5, the AUC data collected from 6xHis-TEV-$\beta_2 M$ samples is shown. For this set of experiments, three different concentrations of $\beta_2 M$, low (7 μM), medium (14 μM), and high (20 μM), were loaded in sample cells and placed in the rotor. Each sample was scanned at three centrifugal speeds of 12000, 16000, and 22000 RPM. The measurements were analyzed using the HeteroAnalysis software. The samples with the low (7 μM) and middle (14 μM) concentrations were

analyzed either globally (fitting all speeds together) or individually (fitting each speed separately). In the sample at the highest concentration, all of the proteins were essentially sedimented to the bottom of the cell at even the slowest speed, so it did not provide us with any concentration gradient making us able to analyze that.

The analysis of sedimentation equilibrium measurements on $\beta_2 M$ samples confirmed the presence of oligomers in solutions in both concentrations. The samples used for these experiments, prepared from the purification of the protein expressed from the first construct (6xHis-TEV-$\beta_2 M$) which did not have SUMO, the solubilization partner. The observed oligomers were in the range of 70–- 140 kDa. For an ideal solution of single non-interacting species Equation 4.1 gives ©), the equilibrium radial concentration as[240]

$$c(r) = c_0 \exp\left[\frac{M_b \omega^2}{RT}\left(\frac{r^2 - r_0^2}{2}\right)\right] = c_0 \exp\left[\sigma\left(\frac{r^2 - r_0^2}{2}\right)\right] \quad (4.1)$$

where r_0 is an arbitrary distance and c_0 is the concentration at r_0. $\frac{M_b \omega^2}{RT}$ is the term referring to the reduced molecular weight, σ. The fit to the individual data sets collected from the 7 μM $\beta_2 M$ solution for the lowest speed indicated the presence of oligomers with a molecular weight of 90 kDa (~ 9-mers). The individual fit to the highest speed indicated 75 kDa (~7-mers) oligomers at the same concentration. The global fit of concentration gradients collected from all speeds at 7 μM, indicated the presence of oligomers of 77 kDa molecular weight. The results of individual fits to different speeds for 14 μM solution were not available. However, the global fit to the concentration gradients from all three speed indicated the presence of 142 kDa oligomers at this higher concentration.

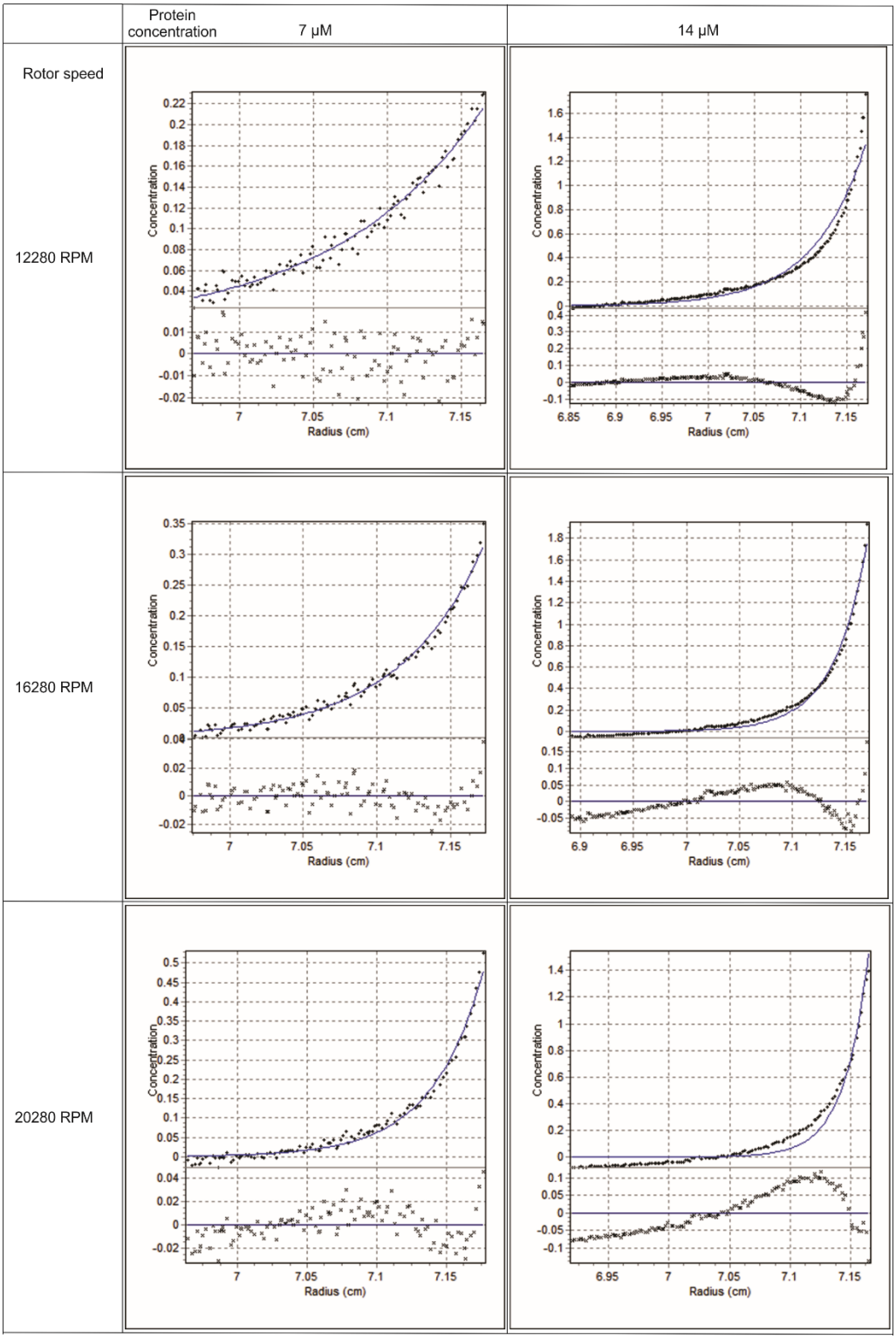

Figure 4.5. Sedimentation equilibrium data showing concentration gradients at three speeds for two concentrations of $\beta_2 M$.

Size exclusion chromatography (SEC) measurements on the purified and refolded $\beta_2 M$ which was expressed in isolation without any soluble partner (Figure 4.6), indicated the presence of high molecular weight aggregates (oligomers).

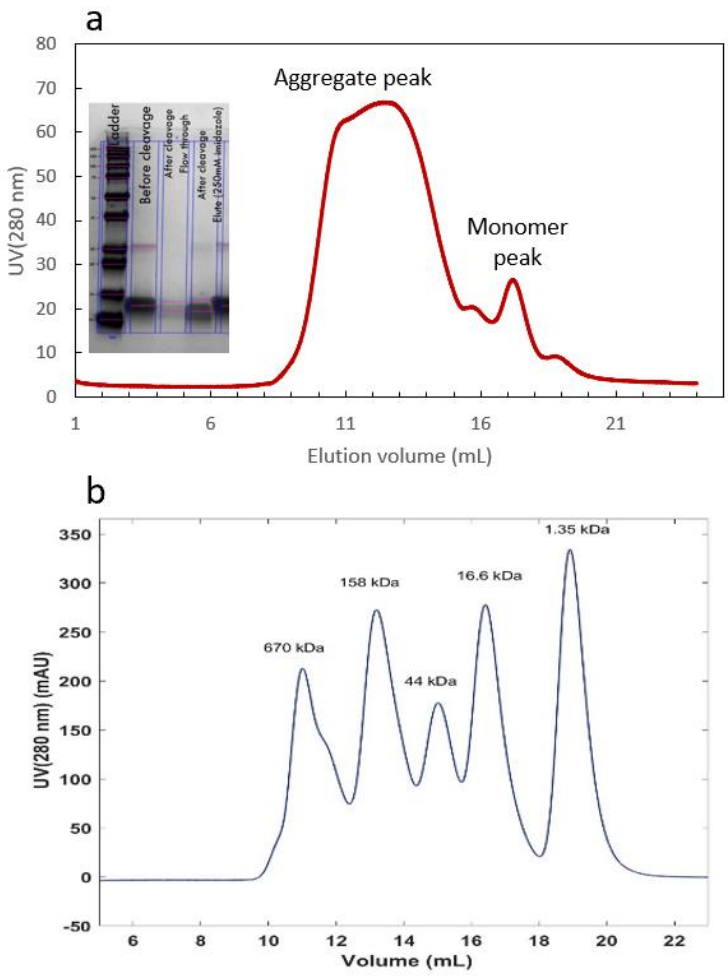

Figure 4.6. Size exclusion chromatography and SDS-PAGE gel on $\beta_2 M$ expressed and purified without soluble partner. (a) SEC chromatogram indicates the presence of a huge fraction of oligomeric species with a diverse range of MWs. The inlet image shows the SDS-PAGE gel of purified and cleaved $\beta_2 M$ which shows to be highly pure. The gel image ensures

that the observed high-molecular weight peak is made of $\beta_2 M$ and not other impurity proteins. (b) size exclusion standard calibration curve.

To increase the production of soluble $\beta_2 M$ and prevent it from forming inclusion bodies upon expression in E. coli. However, as shown in the Western blot in Figure 4.4 (lanes 3&5), the expression level in the soluble fraction of bacterial cell lysate was nothing compared to the insoluble fraction. However, we noticed two noticeable changes in the purified and refolded protein after purification and refolding. First, the cleavage efficiency of 6xHis from the SUMO site increases several folds compared to 6xHis-TEV. For 5 mL solutions with similar concentration of 2 mg/mL refolded $\beta_2 M$ from each of the constructs (with and without SUMO fusion), and with the addition of equivalent units of TEV protease (Sigma Aldrich) and SUMO protease (MCLab), the resulting cleaved protein solutions had distinctly different concentration yields. After separation of protease, uncleaved protein, and 6xHis-TEV (or SUMO) from the cleaved $\beta_2 M$, the resulting solutions of cleavage reaction had concentrations of approximately 0.07 mg/mL and 0.4 mg/mL $\beta_2 M$ for TEV and SUMO protease reactions respectively. Second, the oligomeric species previously observed by AUC and SEC disappeared (Figure 4.7). We conclude that the presence of the solubilization partner, SUMO, causes a substantial enhancement in refolding of $\beta_2 M$ and prevents aggregation and oligomerization during the purification and refolding process. This finding is significant for future amyloid and aggregation studies of $\beta_2 M$ and similar proteins because having an initial monomeric aggregate-free environment is crucial to protein aggregation studies for amyloid disease prevention and cure.

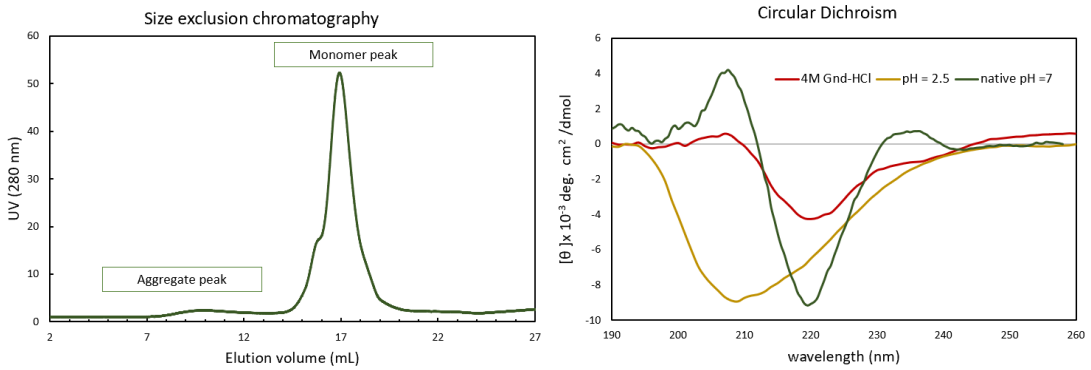

Figure 4.7. SEC and CD measurements on purified, refolded, and cleaved $\beta_2 M$ expressed as a fusion to SUMO protein.

4.4 GFP Expression and Purification

In order to visualize the amyloid fibrils, we used the technique discovered by Xu et al.[241] In this method, super folder green fluorescence protein (sf-GFP) was used for lighting up and visualization of amyloid fibrils due to its affinity to amyloid fibrils. Here, to similarly use sf-GFP for amyloid imaging, we used the GA technique to clone its gene into the pET42(a) plasmid. The sf-GFP encoding gene was a gift from Lei Young. The original plasmid and the schematic of the GA process are shown in Figure 4.8.

Table 4.2. List of synthesized oligonucleotides (primers) for the construction of 6xHis-sf-GFP used in this study

Name	sequence
GFP fragment Forward	CCATCACAGCAAGGGCGAGGAGC
GFP fragment Reversed	GGTACCTCACTTGTACAGCTCGTCCATGC
pET42a vector Forward	CTGTACAAGTGAGGTACCGGTGGTGGCT
pET42a vector Reversed	CCCTTGCTGTGATGGTGATGGTGATGCATATGTATATCTCC

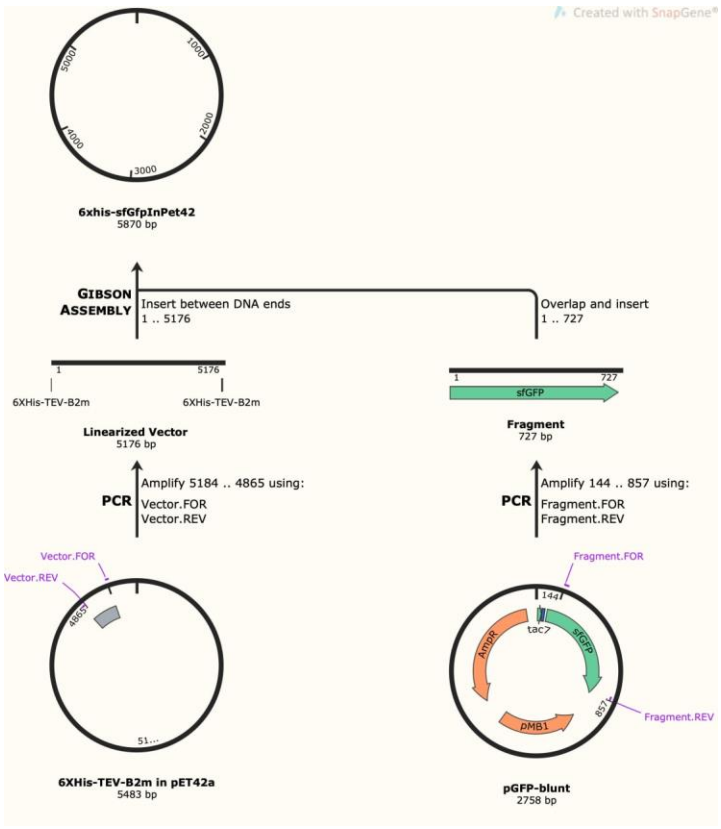

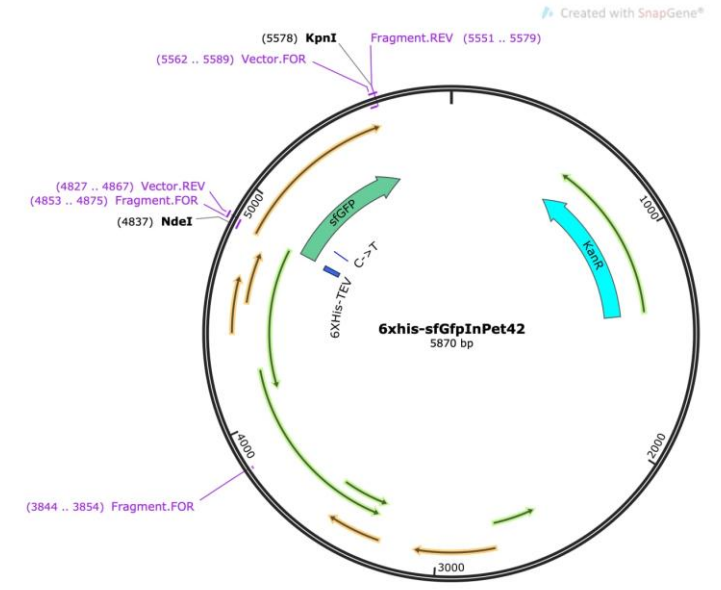

Figure 4.8. Sf-GFP plasmid map construction by GA.

4.5 Conclusion

During the efforts to purify $\beta_2 M$ and have monomeric aggregate-free samples for further biophysical studies, we noticed the vital role of a soluble partner in refolding of $\beta_2 M$. This finding can ease the future studies of amyloid-formation behavior and kinetics in $\beta_2 M$ and other amyloid-forming proteins.

Chapter 5: Probing Conformational Fluctuations in Beta 2-microglobulin Using Single-Molecule FRET and FCS

5.1 Introduction

Misfolding and aggregation of proteins, followed by the formation oligomer intermediates, growth of amyloid fibrils, and aggregation of fibrils into plaques, is involved in the pathogenesis of amyloid diseases[87,242]. About 50 known disease-causing proteins and peptides tend to self-assemble into amyloid fibrils[242]. These insoluble fibrillar structures are rigid, tens of microns in length, and formed by the aggregation of originally soluble proteins. The two constituent protofilaments twist and form fibrils with a diameter of approximately 10 nm. These fibrils have a cross-β diffraction pattern and can bind to dyes such as the Congo red and Thioflavin T (ThT) [243–246].

Amyloid diseases are divided into two groups. The group of amyloid diseases associated with the deposition of fibrils in the nervous system are neurodegenerative diseases[247]. Alzhe'mer's, Parkinson's, and Huntington's diseases are some examples of well-known diseases which, nearly a dozen others, belong to the family of neurodegenerative diseases. Amyloid-β and α-synuclein are two well-characterized neurodegenerative diseases-causing proteins[248,249]. Approximately 15 known diseases fall into the second category of amyloid diseases, called non-neuropathic amyloid diseases, which are divided into two subgroups, systemic and localized. Some examples of diseases in this category include Hemodialysis-related amyloidosis

(systemic), type-II diabetes (localized), cataract (localized), and lysozyme amyloidosis (systemic)[249–252].

The exact mechanism of amyloid formation is still not well-established. Although fibrils and plaques were the first hallmarks of amyloid diseases, the presence of similar fibrils in the body of healthy individuals, specifically in the case of amyloid disease, suggests the existence of other toxic forms of these disease-causing proteins[253,254]. For some amyloid diseases, proteins in the form of soluble oligomers are proven to be the toxic species in the process of amyloid deposition[255]. The toxicity of these intracellular soluble oligomers has been related to their interference with cellular physiology, such as preventing chaperons from functioning properly or disrupting RNA and transport proteins[256]. Figure 5.1 illustrates different pathways in protein aggregation.

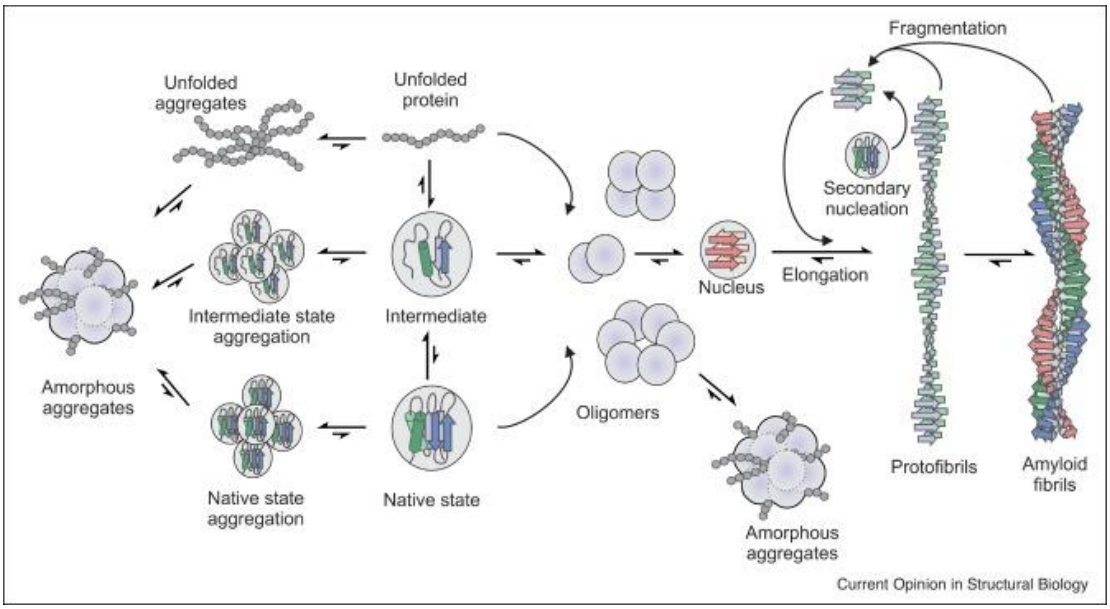

Figure 5.1. Schematic illustration of aggregation pathways. The aggregation can start from a folded, partially unfolded, or a fully unfolded protein. On the path to amyloid formation, the initial oligomer forming precursors could grow to a higher order oligomer which can act as the

nucleus of fibrils. Formed fibrils can undergo fragmentation and act as nucleus of new fibrils. Figure and caption reproduced with permission from reference[257].

The conversion of initially soluble globular or disordered proteins into insoluble amyloid structures have long been studied by researchers from a wide range of scientific areas[258]. The mechanism behind the formation mechanism of some amyloidogenic species of proteins is only partially known. The causes for amyloidogenicity of some protein species include but not limited to a genetic mutation, inability to properly fold due to errors in transcription or translation steps, failure in the proteostasis system (chaperons), and environmental changes[259–263]. During the last 20 years, a novel view of the aggregation nucleation mechanism was formed. In this current view, unfolded native-like states that rise from thermal fluctuations under physiological conditions or intermediate misfolded states are postulated to trigger aggregation[264]. As shown in Figure 5.1, it is known that some degree of reversible unfolding or misfolding and a reversible oligomerization is required (steps 1 and 2) to initiate irreversible conformational rearrangements that lead to formation of oligomers and fibril nuclei with the cross beta structure [161,265]. Both primary and secondary nucleation contribute to the kinetics of amyloid aggregation[266]. Figure 5.1 illustrates the primary nucleation step arising from native or intermediate state oligomers, which further convert into the protofilament nucleus. The protofilaments in some conditions can undergo fragmentation, most probably by cellular proteases[267,268], and become the secondary nucleation point for the growth of new protofilaments. The molecular mechanisms that change the structures of proteins before or during the initial stages of amyloid formation, and interactions associated with the misfolding of proteins and

peptides, remain unclear [265,269]. Despite the fact that the prevention of amyloid diseases are dependent on the understanding of the underlying mechanisms of fibril formation, the nucleation reaction and how it induces the pathogenic behavior is still deficiently understood[270,271]. In the case of familial diseases induced by a specific mutation, it is not still fully understood how a single mutation accelerates the nucleation step[272].

The protein we focus on in this work in chapter 4 and 5 is beta 2-microglobulin ($\beta_2 M$), which forms amyloid fibrils and deposits in the joints of patients suffering from dialysis-related amyloidosis (DRA)[273,274]. $\beta_2 M$ is the light chain of class I major histocompatibility complex. In the native state, $\beta_2 M$ adopts a structure including two β-sheets connected and stabilized through a single disulfide bond [275] (Figure 5.2).

Figure 5.2. Beta 2-microglobulin ($\beta_2 M$) crystal structure (PDB ID: 2d4f) with the disulfide bond marked in magenta.

$\beta_2 M$ and its amyloid-forming variants have been shown to have a flexible structure in its folded biologically active form[276,277]. Despite wild type $\beta_2 M$ ($WT - \beta_2 M$) comprising 70% of the protein content of in vivo amyloid plaques, in

physiological pH and temperature $WT-\beta_2M$ does not show a tendency for aggregation by itself[273]. It has been observed that additives like Cu^{2+}, detergents, and collagen induce partial unfolding of β_2M, which facilitates the Cis-Trans isomerization of Pro32, which is thought to be the beginning step for β_2M self-assembly[97,102,278,279]. $\Delta N6$ is a truncated variant of β_2M that is 30% of the total β_2M that forms amyloid plaques in DRA patients. The $\Delta N6$ variant more readily forms fibril compared to $WT-\beta_2M$, even near neutral pH (6-7)[102,280]. D76N is a second highly amyloidogenic variant of β_2M, which has an Asp substituted for a Asn in position 76 of the amino acid sequence. D76N is a naturally occurring variant causing systemic amyloidosis by depositing amyloid plaques in the internal organs of individuals who are heterozygous for the D76N mutated gene. The fibrils collected from the individuals affected by this hereditary disorder only contained the D76N variant of β_2M [281]. D76N can readily form fibrils *in vitro* at neutral pH withoutadditives[93,282].

As mentioned in the first chapter of this dissertation, highly ordered amyloid fibrils are not the only dangerous factor in protein self-assembly diseases. Amorphous aggregates and misfolded oligomers are thought to be a major source of toxicity to cells and play a role in the initiation of amyloid assembly[247,273]. It is challenging to obtain information experimentally or computationally on the poorly understood initial stages of amyloid assembly. For instance, it remains challenging to probe the aggregate intermediates and misfolded monomer states due to their transient nature and thermodynamic reversibility [283]. The folding intermediates and misfolded states create a collection of interconverting structures, each of which can be a possible aggregation precursor. These substates have dynamics ranging from nanoseconds to hours.

Numerous studies on transient oligomers and intermediate states of amyloidogenic proteins have focused on generating an ensemble of structures and distinguishing the aggregation-prone substates from benign ones[256,284,285] . However, few prior studies have focused on the interconversion dynamics between these substates as a driver for nucleation. It remains unclear why some amyloid forming proteins nucleate amyloid precursors and oligomers under 'stable' conditions where the protein is folded in its native state.

In this research work, we hypothesized that the driving force for the nucleation step in amyloid aggregation involves conformational fluctuations of interconverting folding intermediates in native $\beta_2 M$ and its mutants. According to this hypothesis, in an equilibrium state, if the Gibbs free energy of the aggregated state is lower than the free energy of the native folded state, conformational fluctuations driven by thermal forces are a driving force for aggregation via dynamic changes to the protein monomers that make them more susceptible to aggregation. In most proteins the high activation barrier between monomers and aggregates, and possibly small-scale structural fluctuations, lead to very long nucleation times and the protein monomers are effectively kinetically stabilized. In the case of proteins with a more dynamic structure, the interconversion between states can potentially expedite nucleation in two ways. The first route is by transiently exposing more of the hydrophobic content of the protein sequence to the surface, which increases the chance of oligomerization at higher protein concentrations. Secondly, the fluctuations themselves can promote nucleation, as described below[286–289]. The activation energy barrier to amyloid fibril formation is high, especially for the nucleation step. While fib'ils' low Gibbs free energy levels make their

formation thermodynamically favorable, the high nucleation energy barrier makes it kinetically unfavorable[67,285].

To clearly convey the concept of our hypothesis, we present a couple of simple diagrams. Figure 5.3 compares the reaction coordinate diagram of interconverting species with different rate of interconversion. Here, ΔG_a is the activation energy barrier for the interconversion between two states of a molecule, and ζ, the reaction coordinate (extent of reaction). Figure 5.3a shows a superfast interconversion (too fast to be detectable by available means), in which the activation barrier between the two states is almost negligible, which practically makes the two states indistinguishable. By contrast, in the case of an interconverting molecule for which the rate of interconversion is slow enough the system can thermodynamically be considered a binary fluid with the possibility of separation of states.

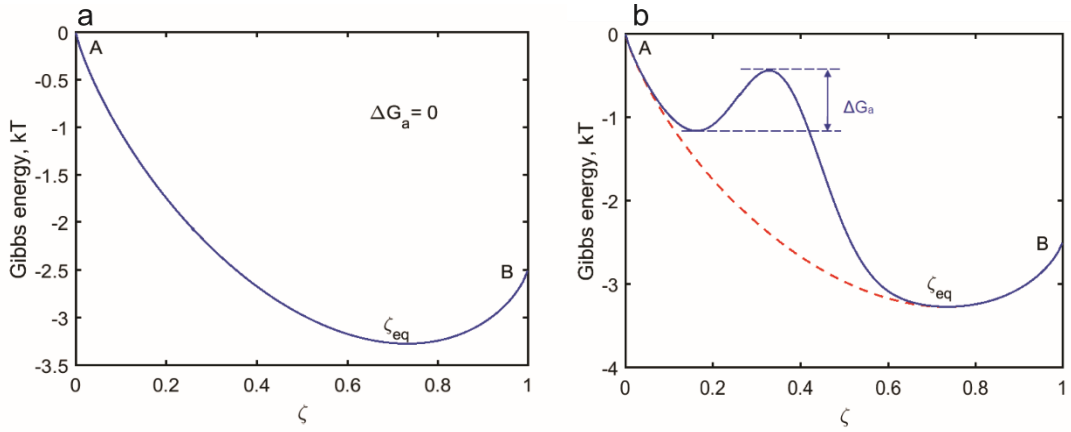

Figure 5.3. Reaction coordinate diagrams showing fast versus slow interconversion. (a) In a superfast interconversion, the activation barrier is negligible, making the two equilibrium states indistinguishable. (b) A real interconversion between states A and B in equilibrium with an activation barrier in order of kT.

Figure 5.4 encompasses a section of both the free energy surface of folding and the free energy of protein aggregates, which shows the protein interconversion reaction coordinate and aggregation reaction coordinate in a 3-dimensional diagram. An activation energy barrier exists between the pre-amyloid oligomers (nucleus) and each of the monomeric states in the pool of folded, partially unfolded, and folding intermediates. G_A and G_B are the free energies of proteins in each of the conformational states, A and B, and ΔG_I is the energy barrier height for the interconversion, which is different in part a and b of the figure. ζ_{eq} is the extent of reaction, which is the fraction of either of conformers A or B ($x_A = 1 - x_B$), ΔG_{AB} is the energy difference between conformer A and B, ΔG_{agg} is the energy barrier between monomer and pre-amyloid oligomers, $\Delta G_{fibrill}$ is the energy barrier between oligomers and amyloid fibrils. In our hypothesis, the interconverting protein monomers could pass the nucleation energy barrier through a random fluctuation while fluctuating between their substates. Figure 5.4a describes our first hypothesis that the lower Gibbs free energy of oligomers ($G_{oligomer}$) is the thermodynamic driving force for oligomerization. For the case of a protein with multiple folded/misfolded substates and depending on height and curvature of the energy barrier between two states, a random fluctuation helps circumventing the rate-limiting step, nucleation, and drives the monomers into the well of pre-amyloid oligomers with the free energy of $G_{oligomer}$. Depending on the ΔG_I value, and free energy difference between conformers the pre-amyloid oligomers might have a higher free energy. In this case the driving force for aggregation depends on kinetics ($\Delta G_I, \Delta G_{agg}$), which is shown in figure 5.4b demonstrating a smaller energy barrier between substates ($\Delta G_{I_1} > \Delta G_{I_2}$) facilitating the fluctuations.

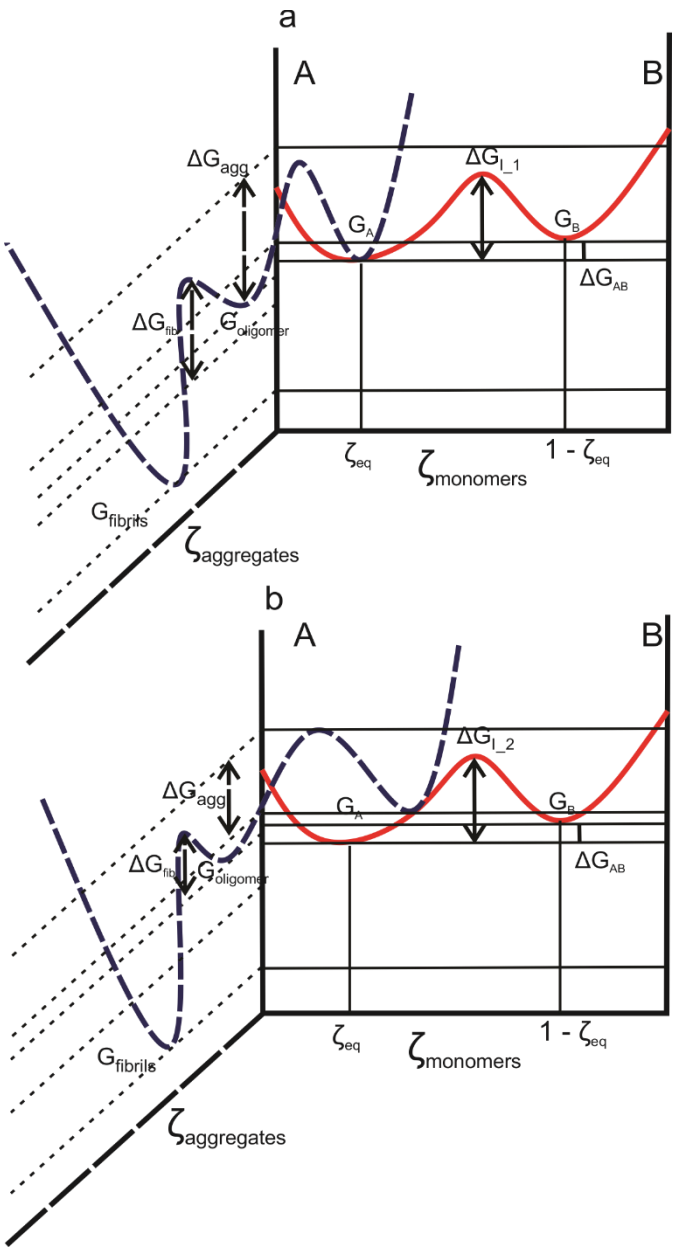

Figure 5.4. Three-dimensional illustration of the interconversion and aggregation reaction coordinates. (a) In this model, the driving force for nucleation is the lower free energy of oligomers. The fluctuations may or may not shorten the lag time for nucleation, depending on the size of the activation barrier. (b) The free energy of pre-amyloid oligomers (nucleation points) is not necessarily lower than the initial monomeric species; the interconversion fluctuations would play a role in overcoming the activation energy by placing the monomers in a higher energy state.

As it has been mentioned before, it is quite difficult experimentally to quantify the fraction of each conformational state of protein as they are transient and short-lived. However, as it will be described in upcoming sections, single molecule fluorescence techniques, make it possible to experimentally to measure the rate of interconversion

between the two or more states. According to the Kramers' theory, the rate of transition between two states of a molecule is given by[290,291],

$$\frac{1}{k_f} = \tau_f \sim \frac{1}{\beta(\omega^*)2\,\omega_u} \exp(\beta \Delta G_f^*) \tag{5.1}$$

where k_f is the rate coefficient, (ω^*) and ω_u are the curvatures of the free-energy surface at the barrier top and the unfolded well, ΔG_f^* is the free energy barrier height, $\beta = \frac{1}{k_B T}$, k_B is the Boltzmann constant, and T is the absolute temperature. By estimating the free energy barrier height, we can estimate ΔG_I values and thus the equilibrium fractions of intermediate folding states. According to Landau theory of phase transitions, the Gibbs energy of a system can be written as,

$$G = G_0(P,T) + f[m(T,P)] - hm, \tag{5.2}$$

in which $G_0(P,T)$ is the background part, $f[m(T,P)]$ is a function of order parameter (m), h is the ordering field, which can be a function of T and P or can be an independent variable. The equilibrium value of the order parameter can be found from $\left(\frac{\partial G}{\partial m}\right)_{P,T} = \left(\frac{\partial f}{\partial m}\right)_{p,T} - h = 0$. Having the interconverting states $A \rightleftarrows B$ (Figure 5.5),

$$G = G_A + (G_B - G_A)\zeta + G_{mix} \tag{5.3}$$

$$\frac{G_B - G_A}{kT} = -lnK(T,P) \tag{5.4}$$

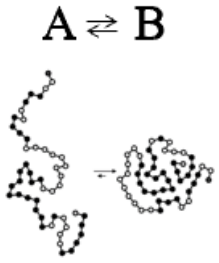

Figure 5.5. Representation of two interconverting state.

where the fraction of state B is the extent of reaction or the reaction coordinate (ζ) and K is the equilibrium constant, which is conjugated to the reaction coordinate, ζ.

Here we consider order parameter, m, to be the fraction of the interconverting states (ζ), which at equilibrium $\frac{\partial G}{\partial \zeta} = 0$. If the activation barrier is high enough to provide a relatively slow interconversion rate, then thermodynamically, the system can be considered a binary fluid with the possibility of the separation of states. If the states form a non-ideal mixture, the possibility of phase separation evolves. In a phase separated system, both liquid phases contain A and B states, but in different proportions.

Here, we investigated the interconversion fluctuations rates in $\beta_2 M$ using single-molecule FRET (smFRET) and FRET fluorescence correlation spectroscopy (FRET-FCS). smFRET probes the distribution of conformational states of $\beta_2 M$ by taking snapshots of individual protein molecules sampling the range of conformation states defined by the free energy surface. FRET-FCS measures the interconversion rates between these conformational states. $\beta_2 M$ labeled with donor and acceptor fluorescent molecules was prepared by overexpression in E. coli and purification from inclusion bodies using IMAC. Previous computational studies using Replica-averaged metadynamics (RAM) on $\beta_2 M$ conformational dynamics have detected the existence of an equilibrium between high and low energy conformations for WT-$\beta_2 M$ and D76N[292]. These conformers showed dynamics with an approximate timescale in the range of μs to ms[292]. However, quantitative data on the rate of interconversion and

equilibrium concentrations of these conformers has not been collected yet. By combining FRET and FCS in this study, we quantified the rates of fluctuations of interconverting states for WT-β_2M, D76N, and $\Delta N6$, which were then rationalized with the amyloidogenicity of each protein. FRET-FCS measurements showed that β_2M presents conformational fluctuations on order of μs – ms times scales with varying interconversion rates for different variants. smFRET measurements showed a broader distribution in the FRET efficiencies for $\Delta N6$ and D76N variants, indicating the presence of more populated intermediate states, compared to $WT-\beta_2M$. The FCS-FRET measurements showed a longer transition time on the order of 5 – 10 s for the main interconversion for the more aggregate-prone variants $\Delta N6$ and D76N, compared to less than a 1 s for the WT, which along with the wider distribution in FRET efficiency histograms of these variants, is indicative of the presence of longer-lived conformational substates. Also, the FCS-FRET fluctuations indicated a faster dynamic interconversion with rates on the order of tens of ms, which can be indicative of presence of smaller scale conformational fluctuations, such as in a single amino acid or small domain, in the more amyloidogenic variants. We show that the fluctuation rates can be used in equation 5.1 for estimating the interconversion free energies (ΔG_I) and further thermodynamic modeling on β_2M variants using equation 5.2.

5.2 Experimental Section

5.2.1 Protein Purification and Labeling

The purification procedure for β_2M has been explained in detail in Chapter 4. Briefly, the gene encoding the wild-type and mutants of β_2M with SUMO fused to the

N terminal as a soluble partner were cloned into the pET42(a) plasmid. For smFRET studies, two cysteine mutants were added to the N and C terminal of β_2M as labeling cites for maleimide reactive donor and acceptor pair of dyes Alexa 488 (A488) and Alexa 594 (A594). The protein was overexpressed in E. coli overnight after the addition of IPTG. β_2M in form of inclusion bodies were purified by a Ni-NTA column in denaturing conditions. β_2M went through refolding by a two-step process and was dialyzed in the appropriate buffer for cleavage by SUMO protease overnight. SUMO, uncleaved β_2M and the protease were separated again using the Ni-NTA column. The resulting cleaved variants of β_2M were more than 95% pure as shown in Figure 5.6 as an example.

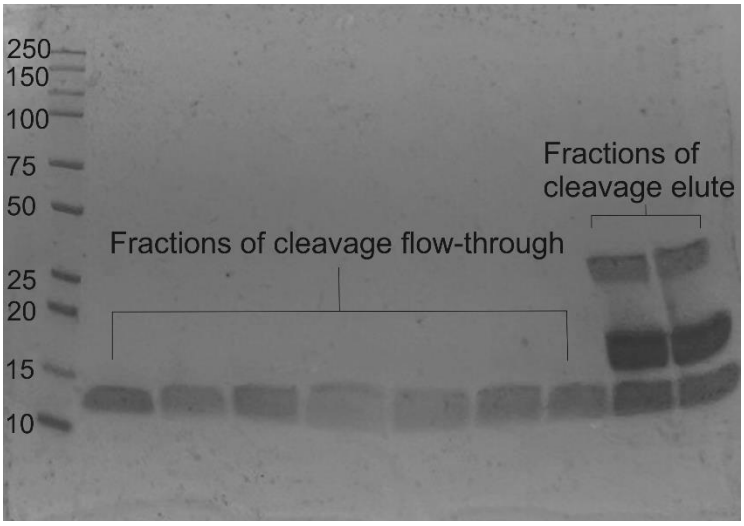

Figure 5.6. D76N-β_2M SDS-PAGE gel. Multiple washing fractions of flow through of cleavage reaction show >95% purity for monomeric protein. Last two lanes show the elute fractions after cleavage.

For the labeling reaction, cleaved variants of β_2M with cysteine mutations on both N and C termini were concentrated to 1.2 mg/mL (100 μM). In all labeling reactions TCEP (tris(2-carboxyethyl) phosphine, Thermofisher) was added in a 5:1

molar ratio to protein for 30 minutes to reduce disulfide bonds prior to the addition of dyes. The pH after the addition of the reducing agent was tested and if necessary, it was adjusted to be at 7.4. A488 and A594 dyes were added to the protein and TCEP mixture with a protein to A488 to A594 ratio of 1:1.3:3. The reaction was left to proceed at room temperature for 3 hours with gentle shaking on the orbital shaker. The unreacted dyes were separated from the reaction mixture using PD-10 desalting columns (Cytiva). The labeled protein underwent further dialysis against 2 liters of phosphate-buffered saline (PBS) overnight at $4°C$. The product of the labeling reactions after separating unreacted dyes was a mixture of double fluorescence labeled proteins containing donor-acceptor, acceptor-donor, donor-donor, and acceptor-acceptor pairs. After labeling, the ratio of donor to acceptor dyes was 1:2, similar to the initial dye ratio.

5.2.2 Single-molecule FRET and FCS

5.2.2.1 Single-molecule FRET (smFRET)

smFRET measurements were performed at room temperature in PBS (pH 7.4) with 0.005% Tween 20 to prevent surface adhesion. The concentration of labeled protein was approximately 50 pM, which gave an approximate average number of 0.5 molecules in the focal volume at any given time and a detector count rate of above 1000 counts/min. A FLUOVIEW FV3000 laser scanning confocal system equipped with time correlated single photon counting (TCSPC) electronics (PicoQuant) capable of performing time-resolved fluorescence techniques (FRET, FCS, FLIM). The donor dye was excited by focusing a 485 nm picosecond pulsed (40 MHz, 90% total diode laser power, Sepia PDL 828, PicoQuant) into the sample solution about a 1 μm distance above the glass surface of a No. 1.0 glass coverslip coated with polyethylene glycol.

The objective used in the smFRET and FCS experiments was a high numerical aperture (NA = 1.4) super corrected 60X Olympus oil immersion lens. The donor and acceptor fluorescence emission was separated from the excitation light using a dichroic mirror. Before being split by the other 560 long-pass dichroic mirror into the donor and acceptor channels, the collected fluorescence emission was spatially filtered using a 50 μM pinhole. The signal collected from the donor and acceptor was filtered using 525/35 and 600/50 filters before entering the hybrid photomultiplier detectors (PicoQuant PMA hybrid series). An illustrative representation of a typical FRET and FCS experimental setup is shown in Figure 5.7.

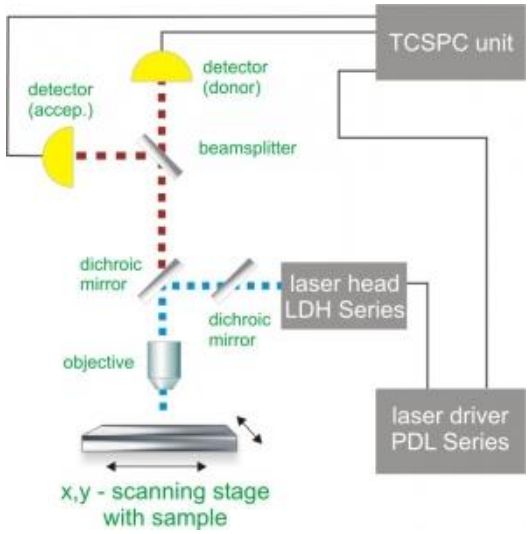

Figure 5.7. Schematics of the experimental setup. Figure and caption reproduced with permission from reference[293].

We utilized the SymphoTime 64 software to extract the FRET efficiency (E_{FRET}) histograms with 1 ms binning time according to equation 5.5 for the donor and acceptor signals collected from each channel as a function of time.

$$E_{FRET} = \frac{I_A}{I_A + \gamma I_D} \tag{5.5a}$$

$$\gamma = \frac{\eta_A \Phi_A}{\eta_D \Phi_D} \tag{5.5b}$$

In the equation 5.5a, I_D and I_A are donor an acceptor fluorescence intensity and γ is the correction factor which depends on the donor and acceptor quantum yields (Φ_A, Φ_B) in the proximity of adjacent amino acids. η_A and η_D are the acceptor and donor channel detection efficiencies, which in this study they are all assumed to be unity.

The spectral cross talk (leakage of donor emission to the acceptor channel) and direct excitation of the acceptor were estimated from separate experiments with singly labeled proteins to be about 4.7% and 7%, respectively. To filter the background noise from the FRET events coming from the fluorophores, a threshold of 25 counts was applied to the sum of the counts from each channel. The histograms of accepted FRET events calculated from equation 5.5 were plotted. FRET values close to zero stem from the photobleached fluorophores or proteins labeled with two donor molecules.

Since we were not attempting to measure exact intramolecular distances in this study, the distribution of FRET efficiencies was sufficient to provide information about the conformational states. We used unity for the value of the correction factor (γ) in equation 5.5[294]. An example of time traces of fluorescence intensities from each of the channels is shown in Figure 5.8.

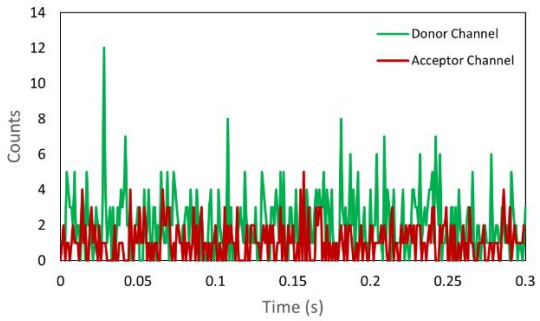

Figure 5.8. An example time trace of the fluorescence intensities collected from the donor and acceptor channels of our system.

5.2.2.2 FCS-FRET

The correlation spectroscopy experiments were carried out in the same setup described for the smFRET under identical buffer conditions, except with a higher protein concentration of 20 nM. To prevent artifacts from dye photophysics (triplet state), the laser intensity was reduced to 66% of maximum laser power for the FCS measurements, compared to the 90% value used in smFRET measurements. Using a pulsed excitation laser provided the benefit of utilizing fluorescence lifetime signal analysis, which eliminated the need to perform a pseudo-cross-correlation of donor signal analysis. The fluorescence lifetime signal correction eliminates the contribution of the detector after-pulsing in correlation measurements. By enabling fluorescence lifetime correlation spectroscopy (FLCS) background correction on the SymPhotime 64 software, we could successfully remove the contribution of after pulsing in the correlation function calculation[295]. The autocorrelation functions for the donor diffusion (G_{DD}) were calculated using formula 5.6 (x = y). The cross-correlation between the donor and acceptor signal (G_{DA}) was calculated using formula 5.6 (x ≠ y), by collecting the emitted fluorescence, which was spectrally separated using the same dichroic mirror used for the smFRET measurements.

$$G_{xy}(\tau) = \frac{<I_{x(t)I_y(t+\tau)}>}{<I_x(t)><I_y(t)>} \tag{5.6a}$$

$$< I_x(t)I_y(t+\tau) > = \lim_{T\to\infty} \frac{1}{T}\int_0^T I_x(t)I_y(t+\tau)dt \tag{5.6b}$$

The calculated correlation functions, G_{DD} and G_{DA}, are from the same molecules; therefore, the molecular translational diffusion contributes to both correlation functions identically. With that said, taking the ratio of the two correlation curves (G_{DD}/G_{DA}) provides us a correlation function with the contributions of intramolecular dynamics stemming from the FRET-fluctuations delineated from translational diffusion[146].

5.3 Results and Discussion

5.3.1 Visualization of Amyloid Fibrils by GFP Using Confocal Fluorescence Microscopy

Thioflavin T (ThT) is a fluorescence molecule whose fluorescence increases drastically upon binding to the amyloid fibrils of many different proteins and peptides. For this reason, this small molecule has been widely used to detect amyloid fibrils and studies of amyloid growth kinetics. Recently, Xu et al. have discovered that GFP and other fluorescent proteins (FPs) have a high affinity to bind to the amyloid fibrils and the small aggregates formed during the lag phase of fibril formation in a variety of proteins (Figure 5.9) [241].

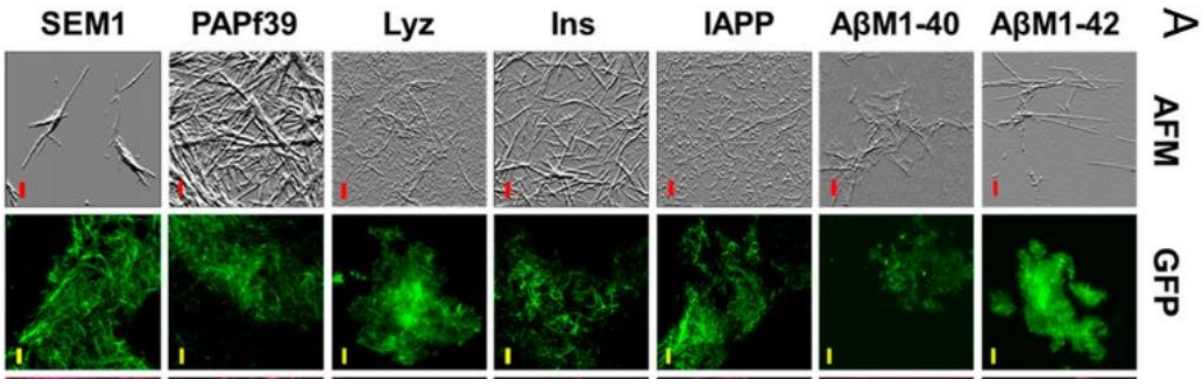

Figure 5.9 GFP bind various amyloid fibrils. (A) Biological amyloid fibrils: AFM images (column 1) show the presence of amyloid fibrils in all samples. CFM (column 2) images of 90 μg/mL amyloid fibrils in the presence of 5 μM GFP (column 2). Figure and caption reproduced with permission from[241].

Here we adopted the GFP imaging technique by Xu et al. to visualize the amyloid fibrils formed by the WT and mutants of $\beta_2 M$ we recombinantly produced and purified. As explained in the methods section, WT and mutant proteins were incubated in 50 mM phosphate buffer at pH 2.5 for 5 days with 600 rpm, and the resulting aggregates or fibrils were mixed with GFP right prior to confocal imaging. Figure 5.10 shows the success of GFP binding to the $\beta_2 M$ amyloids and lighting up the fibrils to visualize them. Comparing the images generated from a WT and D76N mutant, the higher propensity of amyloid formation for D76N can be observed.

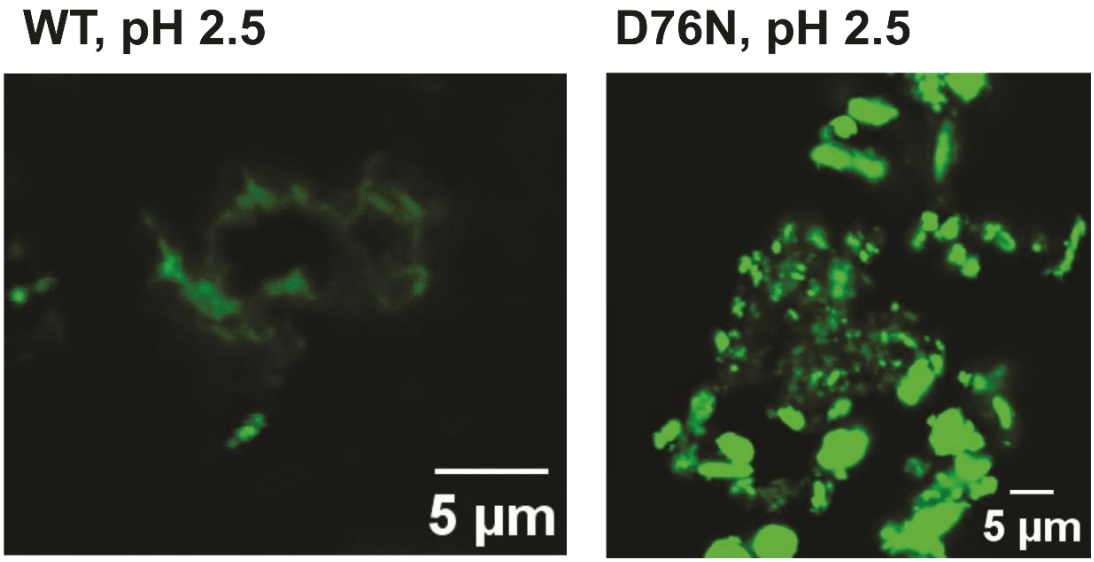

Figure 5.10. GFP binds $\beta_2 M$ amyloid fibrils. (Left 1) Confocal fluorescence imaging of 90 ug/mL of aggregated protein at pH 2.5 in presence of 5 μM GFP. (Right) Confocal fluorescence imaging of 90 ug/mL of D76N $\beta_2 M$ amyloid fibrils formed at pH 2.5

5.3.2 Single-molecule FRET

Single-molecule FRET allows us to detect the conformational state distribution of natively folded β_2M variants. Since FRET can measure distances up ~10 nm, this technique is suitable for observing different folding structures[296]. Free diffusion of single β_2M protein molecules labeled with the donor and acceptor dyes into the laser focal volume produces fluorescence emission bursts that are detected by sensitive photon counting detectors connected to the confocal microscope[297]. The recorded donor and acceptor bursts were used for calculating the FRET efficiencies of each dual-labeled protein molecule using equation 5.5. Because the FRET efficiency is directly proportional to the distance between the donor and acceptor, which changes with the folding state of the protein, the smFRET data resolves the equilibrium distribution of different spatial conformation of β_2M molecules[298,299]. Collecting smFRET data for a sufficiently long time enables forming a statistical distribution of protein conformations, where the most prevalent values of FRET efficiency correspond to the most thermodynamically stable conformations. The calculated FRET efficiency histograms contain information about the relative intramolecular distances and the distribution of folding subpopulations[135,300,301]. Figure 5.11 shows a schematic of the approximate distance between the C and N terminal cysteines of a folded β_2M molecule. The FRET efficiency peak of $WT-\beta_2M$ in its folded state as determined from the crystal structure, which is just one conformation, as shown in the Figure 5.12a is approximately at 50%. Although, the calculated FRET efficiencies are not corrected for the effects of dye quantum yields and the detection efficiencies of detectors, the

50% efficiency is close to what was expected to observe for a 99 amino acid protein using Alexa 488 and Alexa 594 FRET pairs.

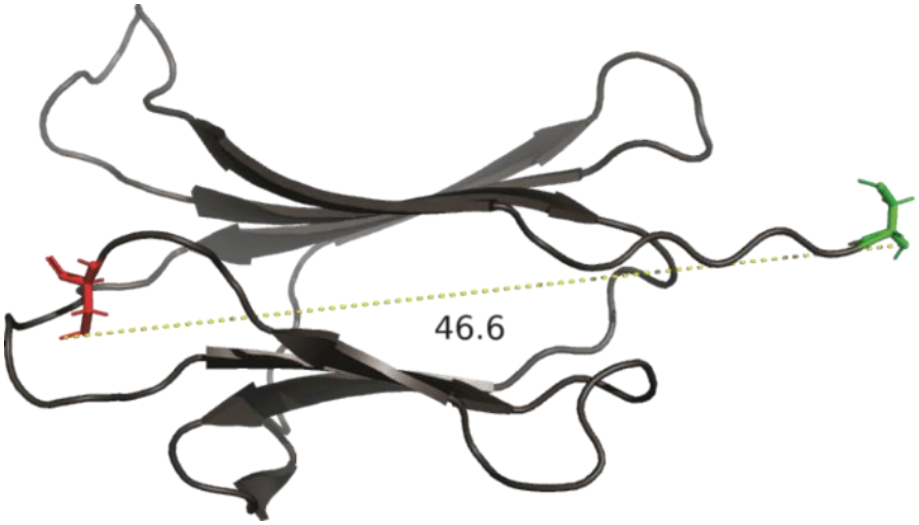

Figure 5.11. Cartoon representation of $WT-\beta_2M$ structure with cysteine mutants added at the N and C termini shown in red and green with a separation distance of 46.6 Å. (PDB ID: 2d4f).

The collected smFRET histograms of $WT-\beta_2M$, as shown in Figure 5.12, showed a relatively broad E_{fret} peak centered around a 45% efficiency. For the pair of donor and acceptor Alexa488 and Alexa594, the R_0 (the distance at which the efficiency is 50%) value is 60 Å. Considering a distance of about 47 Å between the N and C terminus as shown in Figure 5.11 and the size of the fluorescence dyes (0.5-1 nm), the center of the experimental E_{fret} histogram at 45%, or an approximate inter-dye distance of ~64 Å, is reasonable. We repeated smFRET measurements at similar experimental conditions for the mutants $\Delta N6$ and D76N. For the $\Delta N6$ mutant, smFRET measurements provided a E_{fret} histogram centered around a 25% FRET efficiency, indicating the most prevalent inter-dye distance between the donor and acceptor dyes increased to around 72 Å. Even though the value of the efficiency peak were not

corrected for the real value of γ, the broad efficiency distribution histogram showed there was a change in the distribution of intermediate folding states of the mutant compared to the wild type. A E_{fret} histogram centered around a peak near 35% efficiency (66 Å) was measured for the D76N variant. Based on the smFRET work, the broader distributions of FRET efficiencies compared to the wild type could be indicative of interconversions with fast relaxation rates. We note that both mutants showed an overall shift to smaller FRET efficiencies, and thus larger inter-dye distances, which suggests the overall size of the mutants was slightly larger than the wild type. Likewise, the mutants both showed a tail in the FRET efficiency distribution with values up to 80 – 100%. The tail could be associated with contraction of the protein structure, which is typically associated with enhanced hydrophobic interactions.

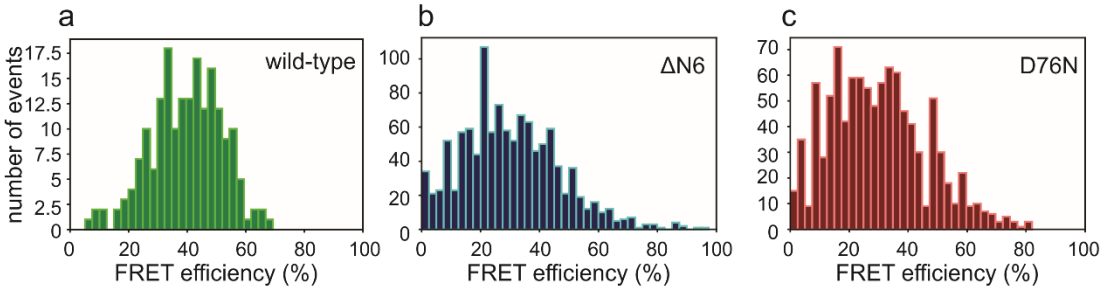

Figure 5. 12. sm-FRET histograms extracted from $\beta_2 M$ variants in native conditions, labeled with Alexa488/Alexa594 at both terminals. (a) FRET efficiency histogram of wild-type $\beta_2 M$. (b) FRET efficiency histogram of D76N $\beta_2 M$ variant labeled with Alexa488/Alexa594 at both terminals. (c) FRET efficiency histogram of $\Delta N6$ $\beta_2 M$ variant.

Information about the dynamics of a molecule can also be extracted from the shape of a FRET efficiency histogram. For molecules in these size scales, the typical residence time in the focal volume is ~1 ms; therefore, if the conformational transition of the molecule as it passes through the focal volume occurs at a rate faster than 1 ms,

then the observed FRET efficiency with be an average of the FRET efficiencies of each state weighted by the population of each state[302]. In essence, the frequent transitions at transition rates faster than the observation time make the subpopulations indistinguishable. Figure 5.13[302] shows the results published by Gopich and Szabo, which tests the Gaussian approximation model they developed against experimental FRET efficiency histograms of a two-state interconverting molecule. The bin time for calculations of these FRET efficiencies was 1 ms and the transition rates are noted in the plots. Comparison of the E_{fret} histogram for WT-$\beta_2 M$ with these model histograms suggests that this molecule undergoes very rapid interconversion, similar to a 2-state or 3-state model with conversion rates approaching 10 s^{-1}.

The FRET efficiency histograms generated from $\Delta N6$ and D76N variants of $\beta_2 M$ have an almost similar shape and broader than the wild type with notable tails at low and high FRET efficiency. The asymmetrical shape of their histograms is comparable to the experimental histograms of a two-state or three-state state model with longer lived subpopulations and slower interconversion dynamics. However, smFRET is limited in the amount of kinetic information it can provide, so further studies were performed with FCS-FRET, which provides information about the number of intermediate states and their interconversion rates.

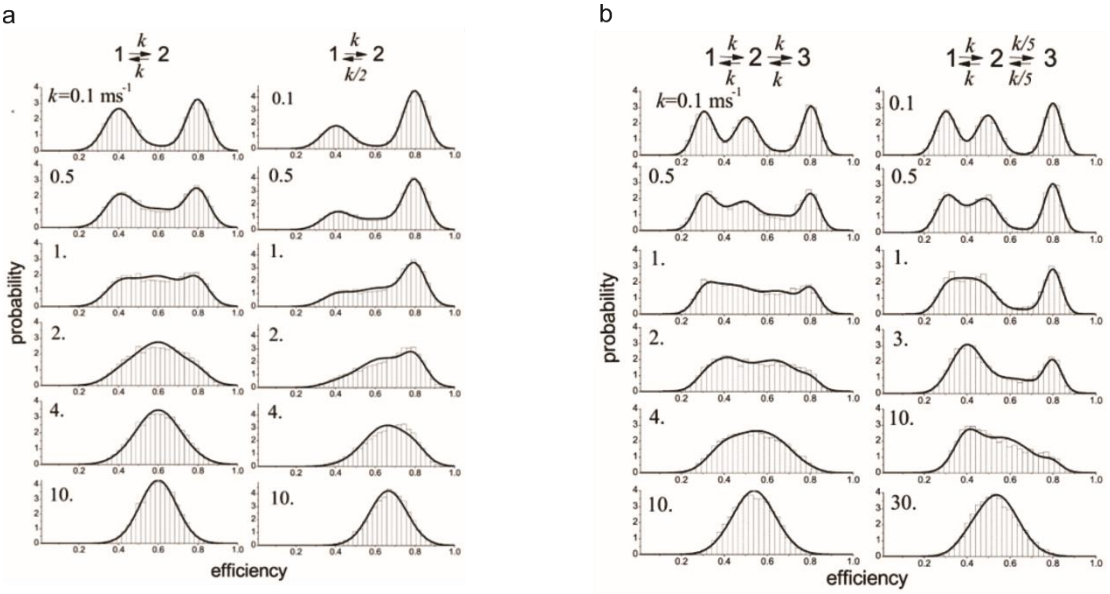

Figure 5.13. The Gaussian approximation (full curves) tested against exact FRET efficiency histograms (bars) for two conformational states with FRET efficiencies = 0.4 and = 0.8 and different values of the transition rate given in the upper left corner of each histogram. Left column: the equilibrium probabilities of the two states are the same. Right column: the probabilities differ by a factor of 2. The total count rate n = 50 ms−1, the bin time is T = 1ms, threshold value is N_T = 30, histogram step h = 1/41. (b) The Gaussian approximation (full curves) tested against simulated FRET efficiency histograms (bars) for a three-state model with FRET efficiencies = 0.3, = 0.5, = 0.8 and different values of the transition rate given in the upper left corner of each histogram. Left column: equal transition rates. Right column: the transitions between states 1 and 2 are faster than those between 2 and 3. The simulated histograms were obtained from 5000 bins of duration T = 1 ms, the total count rate is n = 100 ms−1, Figure and caption reproduced without any changes with permission from reference[302].

5.3.3 FRET-fluctuation spectroscopy indicates millisecond conformational fluctuations in $\beta_2 M$ and its mutants

FRET-FCS measures the relaxation times for the interconversion of $\beta_2 M$ between the different intermediate folding states identified by smFRET. Figure 5.14 show the FCS autocorrelation curves (Figure 5.14a-c) and the FRET-FCS autocorrelation curves for the wild-type (Figure 5.14d) ΔN6 (Figure 5.14e), and D76N (Figure 5.14f) mutants. FRET-FCS data represent conformational movements in orders of us – s. The decay rates associated with the conformational changes in the $\beta_2 M$ structure were calculated by fitting a third-degree exponential function to the FRET autocorrelation functions:

$$y = A_1 exp\,(-\frac{1}{t_1}\tau) + A_2 exp\,(-\frac{1}{t_2}\,\tau) + A_3 exp(-\frac{1}{t_3}\tau), \qquad (5.7)$$

In the equation 5.7, A_i are the amplitudes and t_i are the decay times for each interconversion detected by FRET-FCS.

For the wild-type protein, the fit to the autocorrelation curve showed three characteristic decay times, 0.07 ms (t_1), 1.94 ms (t_2), and 10.9 (t_3) ms. The long decay time of ~10 s is not related to conformational fluctuations and instead could be due to large irreversible aggregates that could have formed during the labeling step. SEC confirmed the lack of presence of these aggregates before the labeling step (Figure 4.7 a). In Table 5.1, the transition rates (inverse of decay time) for each variant are shown. The 14.4 ms^{-1} and 0.68 ms^{-1} interconversion rates suggest FRET-FCS is detecting conversion of $\beta_2 M$ between three major intermediate states[303].

Likewise, the smFRET data for the wild type shows resemblance to the three-state model with fast interconversion near a 4 ms^{-1} rate (Figure 5.13). Thus the 0.68 ms^{-1} interconversion rate is a sensible value to be attributed to the conformational fluctuations.

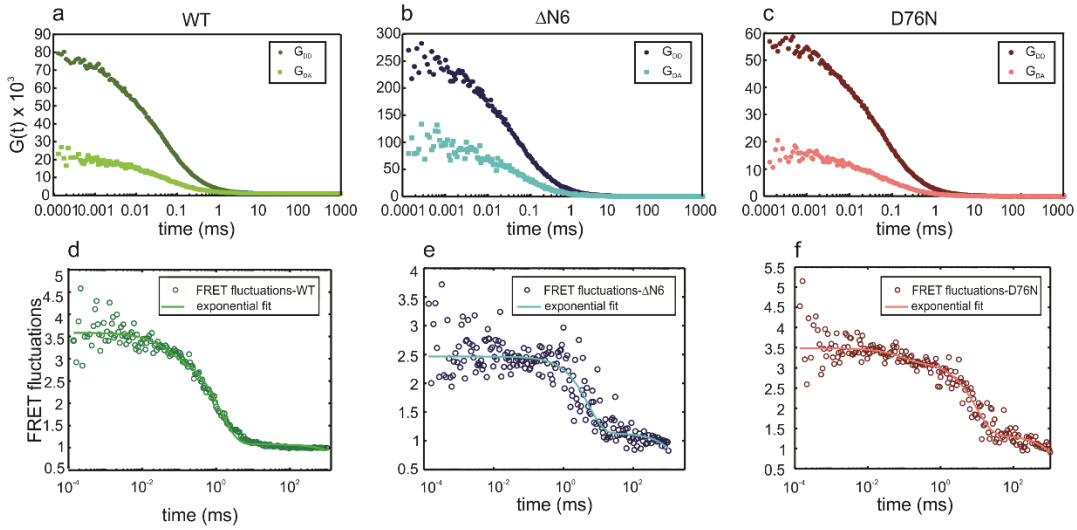

Figure 5.14. Correlation analysis demonstrating distinct FRET-fluctuation patterns for different $\beta_2 M$ variants. The upper row represents autocorrelation function of the donor channel G_{DD}, and the cross-correlation function between the signals from donor and acceptor channels (G_{DA}), The lower row represents each variant's corresponding FRET-fluctuation decay curves.

Table 5.1. Decay rates associate with each $\beta_2 M$ variant.

Fitting parameter	A_1	t_1 **(ms)**	k_1 (ms^{-1})	A_2	t_2 **(ms)**	k_2 (ms^{-1})	A_3	t_3 **(ms)**	k_3 (ms^{-1})
Variant									
WT	0.5434	0.07	14.4	1.943	1.476	0.6772	1.057	10989	9.1e-5
ΔN6	0.105	0.018	54.02	1.336	5.537	0.1739	1.11	6250	1.6e-4
D76N	0.3261	0.084	11.78	1.827	9.708	0.103	1.334	2635	3.7e-4

Figure 5.14e shows the FRET-Fluctuations data extracted from FCS-FRET measurements on $\Delta N6$. The exponential fit to the FRET-fluctuation data showed three decay times of 0.018 ms, 5.54 ms, and 6300 ms (Table 5.1). Here the smallest decay time was the same order of magnitude but 7 times smaller than the wild type protein, indicating a short-lived fluctuating substate. Previous studies on $\Delta N6$ predict a timescale of millisecond-microsecond for the cis-trans isomerization in this variant's conformation[32]. The slower 5.54 ms fluctuations (t_2) could correspond to the cis-trans isomerization of Pro34, which leads to existence of longer-lived isomerized subpopulations with a profound structural change in the $\Delta N6$[273]. As shown in Figure 5.13(b), the smFRET data for $\Delta N6$ demonstrates a histogram that can be interpreted as three interconverting species with a conversion rate near 4 ms^{-1} (Figure 5.13b). If one simultaneously look at the rates of conformational change extracted from FCS-FRET experiments and the shape of FRET efficiency histogram extracted from smFRET experiments, the value of $k_2 = 0.17\, ms^{-1}$ for $\Delta N6$ and its histogram can be most likely interpreted for a three-state interconversion with unequal rates for conversion between states (Figure 5.13b, right column $k = 4\, ms^{-1}$).

The FRET-FCS data collected from the D76N β_2M variant showed distinct features and characteristic decay times compared to $\Delta N6$ and the wild type protein. The FRET-fluctuations correlation curve showed a noticeable exponential decay (t_1) at 0.084 ms, of the same order of magnitude of as WT and $\Delta N6$ but closer to t_1 for WT. The second decay time (t_2) of 9.7 ms was longer than the second decay observed for the $\Delta N6$ variant. This interconversion rate for this fluctuation was the slowest among the three variants. The value of $k_2 = 10\, ms^{-1}$ for D76N, along with the shape of its

smFRET efficiency histogram can lead to the similar conclusion made for $\Delta N6$, which was a three-state interconverting model with a longer lived misfolded substate than that of $\Delta N6$ and WT.

The similarity between the smFRET efficiency histogram of D76N (Figure 5. 10 (b)) and $\Delta N6$ (Figure 5. 10 (c)), and the slower interconversion rate for t_2, which has the highest weight in equation 5.7, along with the fact that these two variants are the only more aggregate-prone natural variants of $\beta_2 M$[93,273] shows clearly that there is a correlation between fluctuations and aggregation propensity of $\beta_2 M$ variants.

Taken together, the FRET-FCS and smFRET data showed features consistent with their amyloid forming ability. We note that we do not have the molecular details about the intermediate states and instead rely on comparing the single molecule measurements to the known aggregation propensity of each protein, which follows the trend of WT < $\Delta N6$ < D76N. Each protein variant showed two conformational fluctuations consistent with three intermediate states. The faster decay time fluctuation showed a decay time on the order of 10^{-2} ms. Comparing the next largest decay time, the WT showed a decay time of ~2 ms compared to 5.3 and 9.7 ms for $\Delta N6$ and D76N. Here the decay time was observed to increase (decay rate decreased) as a function of the aggregation propensity of the mutant. This increase in decay time, indicating an increased residence time of the protein in a certain folding state, could be associated with a slower, and therefore larger spatial scale, conformational change with a slower interconversion rate. Here the decreasing decay rate with increasing aggregation propensity could reveal aggregation prone moieties for a longer time, leading to enhanced aggregation.

5.3.3.1 Control Experiments for Validation of FRET-FCS

To confirm that the fluctuations timescales extracted from the correlation analysis of the FRET-FCS data were a result of conformational dynamics, we performed control measurements at three different experimental conditions. The first measurement was taken in the presence of 4.5 M guanidine-HCl, which causes more than half of the protein molecules in the solution to unfold. As shown in Figure 5.15 a, the FRET fluctuation analysis does yield an exponential decay, indicating no conformational dynamics with a specific characteristic timescale existed. This was due to the complete lack of secondary and tertiary structure in most of the proteins. Secondly, to rule out the presence of aggregates or soluble oligomers as the source of the observed fluctuations donor and acceptor dyes were attached to separate β_2M molecules instead of being placed on the ends of one protein. Here FRET would only occur if aggregation was present in solution. Again, the FRET autocorrelation curve showed no exponential decays, confirming that aggregation was not the source of the observed fluctuations (Figure 5.15b). The last control measurement was a β_2M sample labeled only with the donor dye. As expected, no characteristic decay rate was observed in the FRET fluctuations analysis curve (Figure 5.15. c, brown curve).

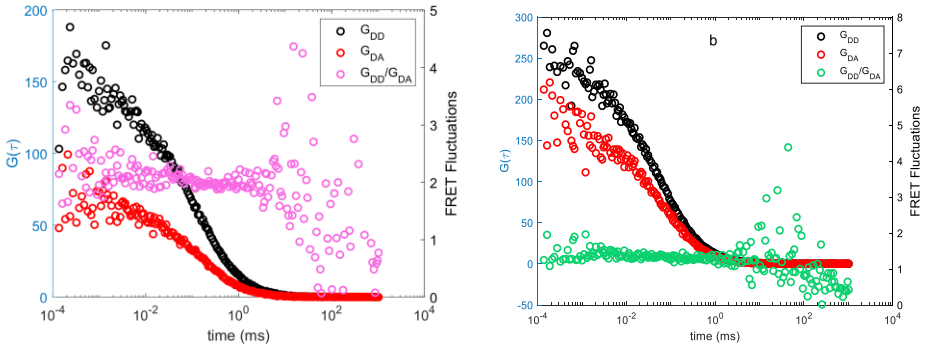

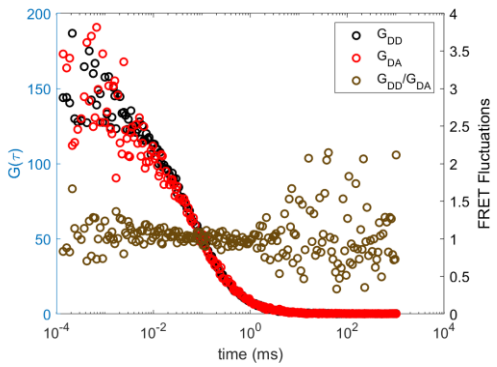

Figure 5.15. (a) denaturing conditions (pink curve). (b) A mixture of donor and acceptor covalently attached on separate β_2M molecules (green curve). (c) Donor-only labeled β_2M (brown curve).

5.4 Conclusions

The interconversion rates extracted from the FRET-FCS and the distributions of FRET efficiencies observed from smFRET showed qualitative trends that were consistent with the known aggregation propensity of $\beta_2 M$ and the mutants we studied. As such, these results were consistent with our hypothesis that conformational fluctuations underly, at least in part, the ability of $\beta_2 M$ and its variants to form amyloid fibrils. Previous extensive studies on aggregation of $\beta_2 M$ have attributed its amyloidogenicity to the presence of folding intermediates in equilibrium with the fully folded lowest energy state of $\beta_2 M$. Putting together the findings of our FRET-FCS study that quantified the rate of ms - μs interconversions between subpopulations of interconverting $\beta_2 M$ conformers, and the results of the smFRET data showing the presence of dynamic subpopulations for $\beta_2 M$ and its variants, we can conclude that the conformational changes and conformation fluctuation time scales of $\beta_2 M$ and its intermediate folding states show correlation with their aggregation propensity. In

particular fluctuations in the time scale of milliseconds was found to have a decreasing interconversion rate with increasing aggregation propensity of the mutant.

Chapter 6: Conclusions and Future Work

6.1 Conclusions

The scientific findings presented in this dissertation contributes new biophysical insights about the role of protein conformations on protein self-assembly; Specifically, the self-assembly due to external perturbation, chemically induced self-assembly, and disease-causing amyloid assembly.

Through the heat-induced lysozyme aggregation work, we showed that even at neutral pH and under sterile conditions, hen egg lysozyme does not aggregate even after being kept at room temperature for weeks. However, we showed that by perturbing lysozyme's structure using a 30-minute exposure to a high temperature of 80 °C, nanoscale aggregates start forming, which grow over several weeks. These results helped better understand the mechanism of aggregate initiation in the aggregate-prone proteins. In many cases of aggregate initiation, only with the emergence of a small fraction of unfolded or partially misfolded protein molecules will the aggregates start to appear and grow.

In the redox-driven hydrogel project made of bovine serum albumin, we could successfully implement a new parameter, degree of protein unfolding, to control the kinetics of dissipative self-assembly controlled gelation and degradation. The degree of unfolding not only indirectly affects the concentration of the crosslinking points (cysteines), but also it affects the mechanical properties and lifespan of the gel through thermodynamics. The hydrophobic interactions are less screened at lower denaturant concentrations which provides additional attractive forces effecting the lifetime of the

gel. This study demonstrates overall the impact that protein structure, even in predominantly unfolded proteins, can exert on dissipative assembly kinetics and represents a first step in realizing synthetic dissipative assembly systems that take advantage of the incredible function and hierarchical structure of proteins. This work suggests that other biological molecules that display hierarchical structuring, such as DNA, protein fibrils, and enzymes, can be used as a building block for dissipative assembly.

In our work on conformational fluctuations of $\beta_2 M$, we have directly observed a quantified rate of the conformational motion for the variants of this protein using the FCS-FRET technique, which separates the translational diffusion of molecules from the intramolecular motions with the same timescales of diffusion. We also demonstrated a correlation between these observed rates and the shape of FRET efficiency histogram distributions for the amyloidogenic variants of $\beta_2 M$. The more extended time of conformational dynamics for more aggregate prone $\Delta N6$ and D76N variants, along with the shape of the FRET efficiency histograms for these variants, leads us to the conclusion that longer-lived misfolded populations in equilibrium with the folded conformers are increasing the amyloidogenicity of these variants by exposing more of the hydrophobic residues to the surface.

On the ground our work, we have recommendations for the future studies related to each of the projects in the following sections.

6.2 Future Work

6.2.1 Improving the biocompatibility of the BSA hydrogels

Developing BSA hydrogels with a tunable lifetime and mechanical properties is a new addition to previously developed protein and polymer hydrogels. It improvises the previously discovered dissipative self-assembly reactions, primarily based on small molecules. However, the high concentration of salts used for the preparation of these hydrogels, as well as the use of relatively non-biocompatible fuel (DTT), prevents them from being used for medical applications. The concentration of chaotropic salts used for protein denaturation should be decreased to improve the biocompatibility of the hydrogels. For that purpose, either a different approach for perturbation of protein tertiary and secondary structure should be used, or the protein building blocks should be engineered and recombinantly produced. The recombinantly produced protein building block should be engineered to not adopt a fully folded structure and contain several cysteine sites. Several examples of such proteins have been previously engineered to be used as hydrogel building blocks with various chemical or physical crosslinking methods. However, recombinant production and purification of proteins are time-consuming and costly. So, it is more desirable to design new approaches to perturb the folding of commercially low-cost proteins as a building block for these hydrogels.

The first and most convenient method is to tune the reactions in a way that with the least amount of denaturant, preferably urea, the ratios of fuels make the dissipative self-assembly possible. For this purpose, quantitative kinetic studies should be done to

determine fuel ratios. Previously, quantitative studies on chemically-fueled dissipative assembly of small molecule cysteine derivatives that used HPLC have been published (Figure 6.1)[211], which can be used as a starting point for more detailed kinetic studies of these redox reactions.

The second approach is to use other forms of denaturants to perturb the proteins' structure. It is known that the addition of ionic surfactants to the protein solutions unfolds the proteins[304,304]. Depending on the charge of the surfactant and protein, the unfolding could or could not lead to the precipitation of the protein/surfactant complex[305]. Figure 6.2 illustrates an example of sodium dodecyl sulfate (SDS) induced unfolding of Beta-lactoglobulin, which does not lead to precipitation due to the overall negative charge of the complex. However, the use of surfactants for denaturation proteins is limited due to the lack of biocompatibility of most ionic surfactants.

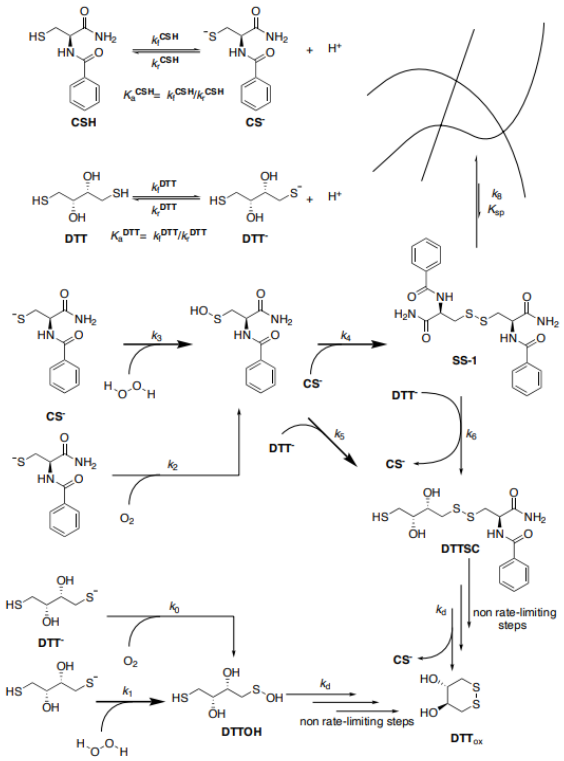

Figure 6.1. Kinetic scheme used for modeling the reactions. Figure and caption reproduced with permission from the supplementary material of the reference[211].

In recent years scientist have developed examples of biocompatible ionic liquid-based surfactants[306,307] and magnetite nanoparticles coated with ionic liquid-based surfactants[308] which can be utilized as a potential protein denaturants in such hydrogels.

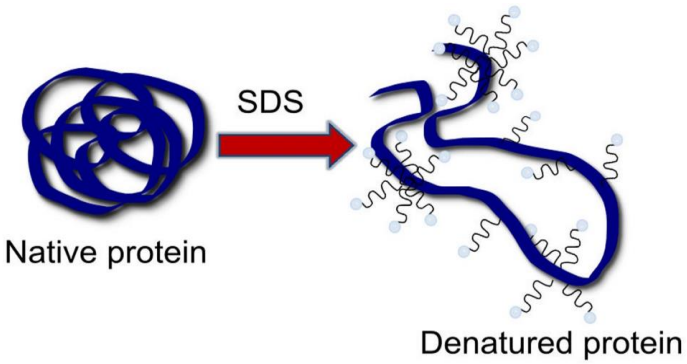

Figure 6.2. 1. Schematic description of denaturation of proteins by surfactant. Figure and caption reproduced with permission from reference[305]

6.2.2 FCS-FRET on a different globular amyloid-forming protein

The results of the FCS-FRET experiments were consistent with our hypothesis about the role of conformational fluctuations between substates of $\beta_2 M$ and its link to the higher amyloidogenicity of its variants. However, similar experiments need to be done to provide supporting results supplemental to what we generated on $\beta_2 M$. Table 6.1, from the work of Iadanza et al[242]., provides information regarding the number of amino acids and the structure of several disease-causing proteins. Repeating FCS-FRET measurements on at least one protein in each category of diseases with different molecular weights could provide additional support to our current results.

Table 6.1. Protein precursors associated with amyloid disease. Table reproduced with permission from reference [242]

Disease	Aggregating protein or peptide	Number of amino acids	Native structure of protein or peptide
Neurodegenerative diseases			
Alzheimer disease	Amyloid-β peptide	40 or 42	Natively unfolded
Familial encephalopathy with neuroserpin inclusion bodies	Neuroserpin	410	α+β
Various neurodegenerative disorders	Actin	~400	Mostly α, some β
Neuroferritinopathy	Ferritin	175 or 183	All α
Spongiform encephalopathies	Prion protein or fragments thereof	253	Natively unfolded (residues 1–120) and α-helical (residues 121–230)
Parkinson disease	α-Synuclein	140	Natively unfolded
Dementia with Lewy bodies	α-Synuclein	140	Natively unfolded
Frontotemporal dementia with Parkinsonism	Tau	352–441	Natively unfolded
Amyotrophic lateral sclerosis	Superoxide dismutase	153	All β, immunoglobulin-like
Huntington disease	Huntingtin with polyQ expansion	3,144	The polyQ-containing region is largely unstructured
Spinocerebellar ataxias	Ataxins with polyQ expansion	816	All β, AXH domain (residues 562–694); the rest are unknown
Spinocerebellar ataxia 17	TATA box-binding protein with polyQ expansion	339	α+β, TBP-like (residues 159–339); unknown (residues 1–158)
Spinal and bulbar muscular atrophy	Androgen receptor with polyQ expansion	919	All α, nuclear receptor ligand-binding domain (residues 669–919); the rest are unknown
Hereditary dentatorubral-pallidoluysian atrophy	Atrophin 1 with polyQ expansion	1,185	Unknown
Familial British dementia	ABri	23	Natively unfolded
Familial Danish dementia	ADan	23	Natively unfolded
Non-neuropathic systemic amyloidoses			
AL amyloidosis	Immunoglobulin light chains or fragments	~90	All β, immunoglobulin-like
AH amyloidosis	Immunoglobulin heavy chains or fragments	~220	All β, immunoglobulin-like
AA amyloidosis	Fragments of serum amyloid A protein	76–104	All α, unknown fold
Familial Mediterranean fever	Fragments of serum amyloid A protein	76–104	All α, unknown fold
Senile systemic amyloidosis	Wild-type transthyretin	127	All β, prealbumin-like
Familial amyloidotic polyneuropathy	Mutants of transthyretin	127	All β, prealbumin-like
Haemodialysis-related amyloidosis	β_2-Microglobulin	99	All β, immunoglobulin-like
ApoAI amyloidosis	N-terminal fragments of ApoAI	80–93	Natively unfolded
ApoAII amyloidosis	N-terminal fragment of ApoAII	98	Unknown
ApoAIV amyloidosis	N-terminal fragment of ApoAIV	~70	Unknown
ApoCII amyloidosis	ApoCII	79	α+unstructured
ApoCIII amyloidosis	ApoCIII	79	α+unstructured
Finnish hereditary amyloidosis	Fragments of gelsolin mutants	71	Natively unfolded
Lysozyme amyloidosis	Mutants of lysozyme	130	α+β, lysozyme fold
Fibrinogen amyloidosis	Variants of fibrinogen α-chain	27–81	Unknown
Icelandic hereditary cerebral amyloid angiopathy	Mutant of cystatin C	120	α+β, cystatin-like
Non-neuropathic localized diseases			
Type II diabetes	Islet amyloid polypeptide (also known as amylin)	37	Natively unfolded
Aortic media amyloidosis	Lactadherin C2-like domain	50	Unfolded
LECT2 amyloidosis	Leukocyte cell-derived chemotaxin 2	151	Unknown
Localized cutaneous amyloidosis	Gelactin 7	136	All β

6.2.3. Thermodynamic/kinetic modeling

The first recommended theoretical work is to use the Gaussian approximation equations developed by Gopich and Szabo [302] to analyze FRET efficiencies collected from multistate molecules. Due to the complexity of the models, the equations are not provided here. Please refer to the reference.

Second, the suggested thermodynamic model in section 5.1 can be used for developing thermodynamic predictions about fluctuation-induced nucleation and microphase separation. The recent and novel works published on phase transitions affected by molecular interconversion[309] and interconversion-controlled liquid-liquid phase separation for chiral molecules[310] provide compelling examples of phase separations affected by molecular interconversion. However, the presence of solvent makes the modeling more complicated for biological systems.

Appendices

Publications

Nikfarjam, S., Ghorbani, M., Adhikari, S., Karlsson, A., Jouravleva, E., Woehl T., Anisimov, M. Irreversible Nature of Mesoscopic Aggregates in Lysozyme Solutions. Colloid J 81, 546–554 (2019).

Nikfarjam, S., Jouravleva, E.V., Anisimov, M.A., Woehl, T. J. Effects of Protein Unfolding on Aggregation and Gelation in Lysozyme Solutions. Biomolecules 10, 1262 (2020).

Licausi, M.; Vervier, A.; Nikfarjam, S.; Woehl, T. J. Interferometric Scattering Microscopy of Albumin-Bound Paclitaxel Nanoparticles. Microscopy and Microanalysis 2022, 28 (S1), 1424–1426. https://doi.org/10.1017/S1431927622005797.

Nikfarjam, s., Gibbons, R., Burni, F., Raghavan, S., Anisimov, M., Woehl, T. "Chemically Fueled Dissipative Assembly of Protein Hydrogels Mediated by Protein Unfolding" Under review.

G. Chandel, J. Sun, S. Etha, B. Zhao, V.S. Sivasankar, S. Nikfarjam, M. Wang, D. Hines, A. Dasgupta, T.J. Woehl, S. Das, "Direct Visualization of Nanoparticle Morphology in Sintered Nanoparticle Ink Traces and the Relationship Between Nanoparticle Morphology, Incomplete Polymer Removal, and Trace Conductivity," Under review.

B. Zhao, V. S. Sivasankar, S. K. Subudhi, S. Sinha, S. Nikfarjam, T. J. Woehl, S. Das, "Three-Dimensional Deposits from Drying Particle-Laden Drops," Under review.

Presentations

Oral Presentation at XXII International Conference on Chemical Thermodynamics in Russia

Title: Nature of Mesoscopic aggregates in Solutions of Lysozyme (June 2019)

Poster Presentation at Chemistry and Physics of Liquids, Gordon Research Conference

Title: Nature of Mesoscopic aggregates in Solutions of Lysozyme (August 2019)

Oral Presentation at 95th ACS Colloid and Surface Science Symposium (Virtual)

Title: Chemically Fueled Assembly of Protein Hydrogels Driven by a Redox Cycle (June 2021)

Oral Presentation at 2022 Biophysical Society Annual Meeting (Will present)

Title: Chemically Fueled Assembly of Protein Hydrogels Driven by a Redox Cycle (February 2022)

Oral presentation at 96th ACS Colloid and Surface Science Symposium

Title: Chemically Fueled Dissipative Assembly of Protein Hydrogels Mediated by Folding State (July 2022)

Bibliography

(1) Campbell, N. A.; Reece, J. B. *Biology*; Benjamin Cummings, 2002.
(2) Hartl, F. U.; Bracher, A.; Hayer-Hartl, M. Molecular Chaperones in Protein Folding and Proteostasis. *Nature* **2011**, *475* (7356), 324–332. https://doi.org/10.1038/nature10317.
(3) Devkate, G. V.; Hardikar, S. R.; Patil, R. N. Protein Aggregation: A Review. *International Journal of Biochemistry Research & Review* **2016**, 1–14. https://doi.org/10.9734/IJBCRR/2016/29829.
(4) Deville, S. S.; Cordes, N. The Extracellular, Cellular, and Nuclear Stiffness, a Trinity in the Cancer Resistome—A Review. *Frontiers in Oncology* **2019**, *9*.
(5) Hess, H.; Clemmens, J.; Qin, D.; Howard, J.; Vogel, V. Light-Controlled Molecular Shuttles Made from Motor Proteins Carrying Cargo on Engineered Surfaces. *Nano Lett.* **2001**, *1* (5), 235–239. https://doi.org/10.1021/nl015521e.
(6) Cooper, G. M. The Central Role of Enzymes as Biological Catalysts. *The Cell: A Molecular Approach. 2nd edition* **2000**.
(7) Dill, K. A.; MacCallum, J. L. The Protein-Folding Problem, 50 Years On. *Science* **2012**, *338* (6110), 1042–1046. https://doi.org/10.1126/science.1219021.
(8) Dobson, C. M. Protein Folding and Misfolding. *Nature* **2003**, *426* (6968), 884–890. https://doi.org/10.1038/nature02261.
(9) Gruebele, M.; Dave, K.; Sukenik, S. Globular Protein Folding In Vitro and In Vivo. *Annual Review of Biophysics* **2016**, *45* (1), 233–251. https://doi.org/10.1146/annurev-biophys-062215-011236.
(10) Gromiha, M. M. Chapter 1 - Proteins. In *Protein Bioinformatics*; Gromiha, M. M., Ed.; Academic Press: Singapore, 2010; pp 1–27. https://doi.org/10.1016/B978-8-1312-2297-3.50001-1.
(11) Skipper, L. PROTEINS | Overview. In *Encyclopedia of Analytical Science (Second Edition)*; Worsfold, P., Townshend, A., Poole, C., Eds.; Elsevier: Oxford, 2005; pp 344–352. https://doi.org/10.1016/B0-12-369397-7/00493-3.
(12) Enciso, M. Hydrogen Bond Models for the Simulation of Protein Folding and Aggregation. **2012**.
(13) Dobson, C. M.; Šali, A.; Karplus, M. Protein Folding: A Perspective from Theory and Experiment. *Angew Chem Int Ed Engl* **1998**, *37* (7), 868–893. https://doi.org/10.1002/(SICI)1521-3773(19980420)37:7<868::AID-ANIE868>3.0.CO;2-H.
(14) Ouellette, R. J.; Rawn, J. D. 14 - Amino Acids, Peptides, and Proteins. In *Principles of Organic Chemistry*; Ouellette, R. J., Rawn, J. D., Eds.; Elsevier: Boston, 2015; pp 371–396. https://doi.org/10.1016/B978-0-12-802444-7.00014-8.
(15) Marians, K. J.; Hiasa, H.; Kim, D. R.; McHenry, C. S. Role of the Core DNA Polymerase III Subunits at the Replication Fork: α IS THE ONLY SUBUNIT REQUIRED FOR PROCESSIVE REPLICATION *. *Journal of Biological Chemistry* **1998**, *273* (4), 2452–2457. https://doi.org/10.1074/jbc.273.4.2452.
(16) Kendrew, J. C.; Bodo, G.; Dintzis, H. M.; Parrish, R. G.; Wyckoff, H.; Phillips, D. C. A Three-Dimensional Model of the Myoglobin Molecule Obtained by X-Ray Analysis. *Nature* **1958**, *181* (4610), 662–666. https://doi.org/10.1038/181662a0.

(17) Henzler-Wildman, K.; Kern, D. Dynamic Personalities of Proteins. *Nature* **2007**, *450* (7172), 964–972. https://doi.org/10.1038/nature06522.
(18) Lyle, N.; Das, R. K.; Pappu, R. V. A Quantitative Measure for Protein Conformational Heterogeneity. *J. Chem. Phys.* **2013**, *139* (12), 121907. https://doi.org/10.1063/1.4812791.
(19) Nagaraju, M.; McGowan, L. C.; Hamelberg, D. Cyclophilin A Inhibition: Targeting Transition-State-Bound Enzyme Conformations for Structure-Based Drug Design. *J. Chem. Inf. Model.* **2013**, *53* (2), 403–410. https://doi.org/10.1021/ci300432w.
(20) Závodszky, P.; Johansen, J. T.; Hvidt, A. Hydrogen-Exchange Study of the Conformational Stability of Human Carbonic-Anhydrase B and Its Metallocomplexes. *European Journal of Biochemistry* **1975**, *56* (1), 67–72. https://doi.org/10.1111/j.1432-1033.1975.tb02207.x.
(21) Venyaminov, S. Yu.; Rajnavölgyi, É.; Mfdgyesi, G. A.; Gergely, J.; Závodszky, P. The Role of Interchain Disulphide Bridges in the Conformational Stability of Human Immunoglobulin G1 Subclass. *European Journal of Biochemistry* **1976**, *67* (1), 81–86. https://doi.org/10.1111/j.1432-1033.1976.tb10635.x.
(22) Fenwick, R. B.; van den Bedem, H.; Fraser, J. S.; Wright, P. E. Integrated Description of Protein Dynamics from Room-Temperature X-Ray Crystallography and NMR. *Proceedings of the National Academy of Sciences* **2014**, *111* (4), E445–E454. https://doi.org/10.1073/pnas.1323440111.
(23) Fraser, J. S.; van den Bedem, H.; Samelson, A. J.; Lang, P. T.; Holton, J. M.; Echols, N.; Alber, T. Accessing Protein Conformational Ensembles Using Room-Temperature X-Ray Crystallography. *Proceedings of the National Academy of Sciences* **2011**, *108* (39), 16247–16252. https://doi.org/10.1073/pnas.1111325108.
(24) Fenwick, R. B.; van den Bedem, H.; Fraser, J. S.; Wright, P. E. Integrated Description of Protein Dynamics from Room-Temperature X-Ray Crystallography and NMR. *Proceedings of the National Academy of Sciences* **2014**, *111* (4), E445–E454. https://doi.org/10.1073/pnas.1323440111.
(25) Austin, R. H.; Beeson, K. W.; Eisenstein, L.; Frauenfelder, H.; Gunsalus, I. C. Dynamics of Ligand Binding to Myoglobin. *Biochemistry* **1975**, *14* (24), 5355–5373. https://doi.org/10.1021/bi00695a021.
(26) Jahn, T. R.; Radford, S. E. The Yin and Yang of Protein Folding. *The FEBS Journal* **2005**, *272* (23), 5962–5970. https://doi.org/10.1111/j.1742-4658.2005.05021.x.
(27) Brockwell, D. J.; Radford, S. E. Intermediates: Ubiquitous Species on Folding Energy Landscapes? *Curr Opin Struct Biol* **2007**, *17* (1), 30–37. https://doi.org/10.1016/j.sbi.2007.01.003.
(28) Bryngelson, J. D.; Onuchic, J. N.; Socci, N. D.; Wolynes, P. G. Funnels, Pathways, and the Energy Landscape of Protein Folding: A Synthesis. *Proteins* **1995**, *21* (3), 167–195. https://doi.org/10.1002/prot.340210302.
(29) Onuchic, J. N.; Wolynes, P. G. Theory of Protein Folding. *Curr Opin Struct Biol* **2004**, *14* (1), 70–75. https://doi.org/10.1016/j.sbi.2004.01.009.
(30) Bartlett, A. I.; Radford, S. E. An Expanding Arsenal of Experimental Methods Yields an Explosion of Insights into Protein Folding Mechanisms. *Nat Struct Mol Biol* **2009**, *16* (6), 582–588. https://doi.org/10.1038/nsmb.1592.

(31) Kerner, M. J.; Naylor, D. J.; Ishihama, Y.; Maier, T.; Chang, H.-C.; Stines, A. P.; Georgopoulos, C.; Frishman, D.; Hayer-Hartl, M.; Mann, M.; Hartl, F. U. Proteome-Wide Analysis of Chaperonin-Dependent Protein Folding in Escherichia Coli. *Cell* **2005**, *122* (2), 209–220. https://doi.org/10.1016/j.cell.2005.05.028.
(32) Eichner, T.; Kalverda, A. P.; Thompson, G. S.; Homans, S. W.; Radford, S. E. Conformational Conversion during Amyloid Formation at Atomic Resolution. *Mol Cell* **2011**, *41* (2), 161–172. https://doi.org/10.1016/j.molcel.2010.11.028.
(33) Jahn, T. R.; Radford, S. E. The Yin and Yang of Protein Folding. *FEBS J* **2005**, *272* (23), 5962–5970. https://doi.org/10.1111/j.1742-4658.2005.05021.x.
(34) Frauenfelder, H.; Petsko, G. A.; Tsernoglou, D. Temperature-Dependent X-Ray Diffraction as a Probe of Protein Structural Dynamics. *Nature* **1979**, *280* (5723), 558–563. https://doi.org/10.1038/280558a0.
(35) Bhatia, S.; Udgaonkar, J. B. Heterogeneity in Protein Folding and Unfolding Reactions. *Chem. Rev.* **2022**, *122* (9), 8911–8935. https://doi.org/10.1021/acs.chemrev.1c00704.
(36) Schmidpeter, P. A. M.; Koch, J. R.; Schmid, F. X. Control of Protein Function by Prolyl Isomerization. *Biochimica et Biophysica Acta (BBA) - General Subjects* **2015**, *1850* (10), 1973–1982. https://doi.org/10.1016/j.bbagen.2014.12.019.
(37) Brichkina, A.; Nguyen, N. T.; Baskar, R.; Wee, S.; Gunaratne, J.; Robinson, R. C.; Bulavin, D. V. Proline Isomerisation as a Novel Regulatory Mechanism for P38MAPK Activation and Functions. *Cell Death Differ* **2016**, *23* (10), 1592–1601. https://doi.org/10.1038/cdd.2016.45.
(38) Mukaiyama, A.; Nakamura, T.; Makabe, K.; Maki, K.; Goto, Y.; Kuwajima, K. Native-State Heterogeneity of B2-Microglobulin as Revealed by Kinetic Folding and Real-Time NMR Experiments. *Journal of Molecular Biology* **2013**, *425* (2), 257–272. https://doi.org/10.1016/j.jmb.2012.11.004.
(39) Chiti, F.; Lorenzi, E. D.; Grossi, S.; Mangione, P.; Giorgetti, S.; Caccialanza, G.; Dobson, C. M.; Merlini, G.; Ramponi, G.; Bellotti, V. A Partially Structured Species of B2-Microglobulin Is Significantly Populated under Physiological Conditions and Involved in Fibrillogenesis *. *Journal of Biological Chemistry* **2001**, *276* (50), 46714–46721. https://doi.org/10.1074/jbc.M107040200.
(40) Michiels, E.; Rousseau, F.; Schymkowitz, J. Mechanisms and Therapeutic Potential of Interactions between Human Amyloids and Viruses. *Cell Mol Life Sci* **2021**, *78* (6), 2485–2501. https://doi.org/10.1007/s00018-020-03711-8.
(41) Benilova, I.; Karran, E.; De Strooper, B. The Toxic Aβ Oligomer and Alzheimer's Disease: An Emperor in Need of Clothes. *Nat Neurosci* **2012**, *15* (3), 349–357. https://doi.org/10.1038/nn.3028.
(42) Silva, J. L.; Cino, E. A.; Soares, I. N.; Ferreira, V. F.; A P de Oliveira, G. Targeting the Prion-like Aggregation of Mutant P53 to Combat Cancer. *Acc Chem Res* **2018**, *51* (1), 181–190. https://doi.org/10.1021/acs.accounts.7b00473.
(43) Housmans, J. A. J.; Wu, G.; Schymkowitz, J.; Rousseau, F. A Guide to Studying Protein Aggregation. *FEBS J* **2021**. https://doi.org/10.1111/febs.16312.
(44) Dekel, Y.; Machluf, Y.; Gefen, T.; Eidelshtein, G.; Kotlyar, A.; Bram, Y.; Shahar, E.; Reslane, F.; Aizenshtein, E.; Pitcovski, J. Formation of Multimeric Antibodies for Self-Delivery of Active Monomers. *Drug Delivery* **2017**, *24* (1), 199–208. https://doi.org/10.1080/10717544.2016.1242179.

(45) Wang, W.; Roberts, C. J. Protein Aggregation – Mechanisms, Detection, and Control. *International Journal of Pharmaceutics* **2018**, *550* (1), 251–268. https://doi.org/10.1016/j.ijpharm.2018.08.043.
(46) Wang, W.; Nema, S.; Teagarden, D. Protein Aggregation--Pathways and Influencing Factors. *Int J Pharm* **2010**, *390* (2), 89–99. https://doi.org/10.1016/j.ijpharm.2010.02.025.
(47) Joubert, M. K.; Deshpande, M.; Yang, J.; Reynolds, H.; Bryson, C.; Fogg, M.; Baker, M. P.; Herskovitz, J.; Goletz, T. J.; Zhou, L.; Moxness, M.; Flynn, G. C.; Narhi, L. O.; Jawa, V. Use of In Vitro Assays to Assess Immunogenicity Risk of Antibody-Based Biotherapeutics. *PLOS ONE* **2016**, *11* (8), e0159328. https://doi.org/10.1371/journal.pone.0159328.
(48) Filipe, V.; Jiskoot, W.; Basmeleh, A. H.; Halim, A.; Schellekens, H.; Brinks, V. Immunogenicity of Different Stressed IgG Monoclonal Antibody Formulations in Immune Tolerant Transgenic Mice. *MAbs* **2012**, *4* (6), 740–752. https://doi.org/10.4161/mabs.22066.
(49) Freitag, A. J.; Shomali, M.; Michalakis, S.; Biel, M.; Siedler, M.; Kaymakcalan, Z.; Carpenter, J. F.; Randolph, T. W.; Winter, G.; Engert, J. Investigation of the Immunogenicity of Different Types of Aggregates of a Murine Monoclonal Antibody in Mice. *Pharm. Res.* **2015**, *32* (2), 430–444. https://doi.org/10.1007/s11095-014-1472-6.
(50) Uchino, T.; Miyazaki, Y.; Yamazaki, T.; Kagawa, Y. Immunogenicity of Protein Aggregates of a Monoclonal Antibody Generated by Forced Shaking Stress with Siliconized and Nonsiliconized Syringes in BALB/c Mice. *J. Pharm. Pharmacol.* **2017**, *69* (10), 1341–1351. https://doi.org/10.1111/jphp.12765.
(51) *Classification of Protein Aggregates - ScienceDirect*. https://www.sciencedirect.com/science/article/pii/S0022354915317184 (accessed 2022-11-09).
(52) *Protein aggregation and immunogenicity of biotherapeutics - ScienceDirect*. https://www.sciencedirect.com/science/article/pii/S037851732030507X (accessed 2022-11-09).
(53) Wang, W.; Singh, S. K.; Li, N.; Toler, M. R.; King, K. R.; Nema, S. Immunogenicity of Protein Aggregates--Concerns and Realities. *Int J Pharm* **2012**, *431* (1–2), 1–11. https://doi.org/10.1016/j.ijpharm.2012.04.040.
(54) Bruijn, L. I.; Becher, M. W.; Lee, M. K.; Anderson, K. L.; Jenkins, N. A.; Copeland, N. G.; Sisodia, S. S.; Rothstein, J. D.; Borchelt, D. R.; Price, D. L.; Cleveland, D. W. ALS-Linked SOD1 Mutant G85R Mediates Damage to Astrocytes and Promotes Rapidly Progressive Disease with SOD1-Containing Inclusions. *Neuron* **1997**, *18* (2), 327–338. https://doi.org/10.1016/S0896-6273(00)80272-X.
(55) *Formation of Neuronal Intranuclear Inclusions Underlies the Neurological Dysfunction in Mice Transgenic for the HD Mutation - ScienceDirect*. https://www.sciencedirect.com/science/article/pii/S009286740080513 9?via%3Dihub (accessed 2022-11-01).
(56) Chartier-Harlin, M.-C.; Crawford, F.; Houlden, H.; Warren, A.; Hughes, D.; Fidani, L.; Goate, A.; Rossor, M.; Roques, P.; Hardy, J.; Mullan, M. Early-Onset Alzheimer's Disease Caused by Mutations at Codon 717 of the β-Amyloid Precursor Protein Gene. *Nature* **1991**, *353* (6347), 844–846. https://doi.org/10.1038/353844a0.

(57) *Protein aggregation can inhibit clathrin-mediated endocytosis by chaperone competition | PNAS*. https://www.pnas.org/doi/10.1073/pnas.1321811111 (accessed 2022-11-01).
(58) Soto, C. Unfolding the Role of Protein Misfolding in Neurodegenerative Diseases. *Nat Rev Neurosci* **2003**, *4* (1), 49–60. https://doi.org/10.1038/nrn1007.
(59) Hetz, C.; Glimcher, L. H. Protein Homeostasis Networks in Physiology and Disease. *Current Opinion in Cell Biology* **2011**, *23* (2), 123–125. https://doi.org/10.1016/j.ceb.2011.01.004.
(60) Clausen, L.; Abildgaard, A. B.; Gersing, S. K.; Stein, A.; Lindorff-Larsen, K.; Hartmann-Petersen, R. Chapter Two - Protein Stability and Degradation in Health and Disease. In *Advances in Protein Chemistry and Structural Biology*; Donev, R., Ed.; Molecular Chaperones in Human Disorders; Academic Press, 2019; Vol. 114, pp 61–83. https://doi.org/10.1016/bs.apcsb.2018.09.002.
(61) Balch, W. E.; Morimoto, R. I.; Dillin, A.; Kelly, J. W. Adapting Proteostasis for Disease Intervention. *Science* **2008**, *319* (5865), 916–919. https://doi.org/10.1126/science.1141448.
(62) Hay, D. G. Progressive Decrease in Chaperone Protein Levels in a Mouse Model of Huntington's Disease and Induction of Stress Proteins as a Therapeutic Approach. *Human Molecular Genetics* **2004**, *13* (13), 1389–1405. https://doi.org/10.1093/hmg/ddh144.
(63) Gidalevitz, T.; Ben-Zvi, A.; Ho, K. H.; Brignull, H. R.; Morimoto, R. I. Progressive Disruption of Cellular Protein Folding in Models of Polyglutamine Diseases. *Science* **2006**, *311* (5766), 1471–1474. https://doi.org/10.1126/science.1124514.
(64) Ben-Zvi, A.; Miller, E. A.; Morimoto, R. I. Collapse of Proteostasis Represents an Early Molecular Event in Caenorhabditis Elegans Aging. *Proc Natl Acad Sci U S A* **2009**, *106* (35), 14914–14919. https://doi.org/10.1073/pnas.0902882106.
(65) Eisele, Y. S.; Monteiro, C.; Fearns, C.; Encalada, S. E.; Wiseman, R. L.; Powers, E. T.; Kelly, J. W. Targeting Protein Aggregation for the Treatment of Degenerative Diseases. *Nat Rev Drug Discov* **2015**, *14* (11), 759–780. https://doi.org/10.1038/nrd4593.
(66) Sipe, J. D.; Benson, M. D.; Buxbaum, J. N.; Ikeda, S.-I.; Merlini, G.; Saraiva, M. J. M.; Westermark, P. Amyloid Fibril Protein Nomenclature: 2010 Recommendations from the Nomenclature Committee of the International Society of Amyloidosis. *Amyloid* **2010**, *17* (3–4), 101–104. https://doi.org/10.3109/13506129.2010.526812.
(67) Willbold, D.; Strodel, B.; Schröder, G. F.; Hoyer, W.; Heise, H. Amyloid-Type Protein Aggregation and Prion-like Properties of Amyloids. *Chem. Rev.* **2021**, *121* (13), 8285–8307. https://doi.org/10.1021/acs.chemrev.1c00196.
(68) Chiti, F.; Webster, P.; Taddei, N.; Clark, A.; Stefani, M.; Ramponi, G.; Dobson, C. M. Designing Conditions for in Vitro Formation of Amyloid Protofilaments and Fibrils. *Proc Natl Acad Sci U S A* **1999**, *96* (7), 3590–3594.
(69) L, W.; Sk, M.; Mr, S.; D, E.; R, R. Bacterial Inclusion Bodies Contain Amyloid-like Structure. *PLoS biology* **2008**, *6* (8). https://doi.org/10.1371/journal.pbio.0060195.

(70) *Structure of the cross-β spine of amyloid-like fibrils | Nature*. https://www.nature.com/articles/nature03680 (accessed 2022-11-02).
(71) Eisenberg, D.; Jucker, M. The Amyloid State of Proteins in Human Diseases. *Cell* **2012**, *148* (6), 1188–1203. https://doi.org/10.1016/j.cell.2012.02.022.
(72) Chiti, F.; Dobson, C. M. Protein Misfolding, Functional Amyloid, and Human Disease. *Annual Review of Biochemistry* **2006**, *75* (1), 333–366. https://doi.org/10.1146/annurev.biochem.75.101304.123901.
(73) Bolognesi, B.; Kumita, J. R.; Barros, T. P.; Esbjorner, E. K.; Luheshi, L. M.; Crowther, D. C.; Wilson, M. R.; Dobson, C. M.; Favrin, G.; Yerbury, J. J. ANS Binding Reveals Common Features of Cytotoxic Amyloid Species. *ACS Chem Biol* **2010**, *5* (8), 735–740. https://doi.org/10.1021/cb1001203.
(74) Ferrone, F. Analysis of Protein Aggregation Kinetics. *Methods Enzymol* **1999**, *309*, 256–274. https://doi.org/10.1016/s0076-6879(99)09019-9.
(75) Powers, E. T.; Powers, D. L. The Kinetics of Nucleated Polymerizations at High Concentrations: Amyloid Fibril Formation near and above the "Supercritical Concentration." *Biophys J* **2006**, *91* (1), 122–132. https://doi.org/10.1529/biophysj.105.073767.
(76) Jarrett, J. T.; Lansbury, P. T. Seeding "One-Dimensional Crystallization" of Amyloid: A Pathogenic Mechanism in Alzheimer's Disease and Scrapie? *Cell* **1993**, *73* (6), 1055–1058. https://doi.org/10.1016/0092-8674(93)90635-4.
(77) Serio, T. R.; Cashikar, A. G.; Kowal, A. S.; Sawicki, G. J.; Moslehi, J. J.; Serpell, L.; Arnsdorf, M. F.; Lindquist, S. L. Nucleated Conformational Conversion and the Replication of Conformational Information by a Prion Determinant. *Science* **2000**, *289* (5483), 1317–1321. https://doi.org/10.1126/science.289.5483.1317.
(78) Hofrichter, J.; Ross, P. D.; Eaton, W. A. Kinetics and Mechanism of Deoxyhemoglobin S Gelation: A New Approach to Understanding Sickle Cell Disease. *Proc Natl Acad Sci U S A* **1974**, *71* (12), 4864–4868. https://doi.org/10.1073/pnas.71.12.4864.
(79) Ferrone, F. A.; Hofrichter, J.; Eaton, W. A. Kinetics of Sickle Hemoglobin Polymerization. II. A Double Nucleation Mechanism. *J Mol Biol* **1985**, *183* (4), 611–631. https://doi.org/10.1016/0022-2836(85)90175-5.
(80) Hurshman, A. R.; White, J. T.; Powers, E. T.; Kelly, J. W. Transthyretin Aggregation under Partially Denaturing Conditions Is a Downhill Polymerization. *Biochemistry* **2004**, *43* (23), 7365–7381. https://doi.org/10.1021/bi049621l.
(81) Eichner, T.; Radford, S. E. Understanding the Complex Mechanisms of B2-Microglobulin Amyloid Assembly. *FEBS J* **2011**, *278* (20), 3868–3883. https://doi.org/10.1111/j.1742-4658.2011.08186.x.
(82) Wieczorek, M.; Abualrous, E. T.; Sticht, J.; Álvaro-Benito, M.; Stolzenberg, S.; Noé, F.; Freund, C. Major Histocompatibility Complex (MHC) Class I and MHC Class II Proteins: Conformational Plasticity in Antigen Presentation. *Front Immunol* **2017**, *8*, 292. https://doi.org/10.3389/fimmu.2017.00292.
(83) Pashley, C. L.; Hewitt, E. W.; Radford, S. E. Comparison of the Aggregation of Homologous B2-Microglobulin Variants Reveals Protein Solubility as a Key Determinant of Amyloid Formation. *J Mol Biol* **2016**, *428* (3), 631–643. https://doi.org/10.1016/j.jmb.2016.01.009.

(84) Zhang, H.; Cui, B.; Zhou, Y.; Wang, X.; Wu, W.; Wang, Z.; Dai, Z.; Cheng, Q.; Yang, K. B2M Overexpression Correlates with Malignancy and Immune Signatures in Human Gliomas. *Sci Rep* **2021**, *11* (1), 5045. https://doi.org/10.1038/s41598-021-84465-6.
(85) Hoop, C. L.; Zhu, J.; Bhattacharya, S.; Tobita, C. A.; Radford, S. E.; Baum, J. Collagen I Weakly Interacts with the β-Sheets of β_2-Microglobulin and Enhances Conformational Exchange To Induce Amyloid Formation. *J. Am. Chem. Soc.* **2020**, *142* (3), 1321–1331. https://doi.org/10.1021/jacs.9b10421.
(86) *Amyloidosis & Kidney Disease | NIDDK*. National Institute of Diabetes and Digestive and Kidney Diseases. https://www.niddk.nih.gov/health-information/kidney-disease/amyloidosis (accessed 2021-08-16).
(87) Scarpioni, R.; Ricardi, M.; Albertazzi, V.; De Amicis, S.; Rastelli, F.; Zerbini, L. Dialysis-Related Amyloidosis: Challenges and Solutions. *Int J Nephrol Renovasc Dis* **2016**, *9*, 319–328. https://doi.org/10.2147/IJNRD.S84784.
(88) Muchtar, E.; Dispenzieri, A.; Magen, H.; Grogan, M.; Mauermann, M.; McPhail, E. D.; Kurtin, P. J.; Leung, N.; Buadi, F. K.; Dingli, D.; Kumar, S. K.; Gertz, M. A. Systemic Amyloidosis from A (AA) to T (ATTR): A Review. *Journal of Internal Medicine* **2021**, *289* (3), 268–292. https://doi.org/10.1111/joim.13169.
(89) Trinh, C. H.; Smith, D. P.; Kalverda, A. P.; Phillips, S. E. V.; Radford, S. E. Crystal Structure of Monomeric Human β-2-Microglobulin Reveals Clues to Its Amyloidogenic Properties. *Proceedings of the National Academy of Sciences* **2002**, *99* (15), 9771–9776. https://doi.org/10.1073/pnas.152337399.
(90) Hodkinson, J. P.; Jahn, T. R.; Radford, S. E.; Ashcroft, A. E. HDX-ESI-MS Reveals Enhanced Conformational Dynamics of the Amyloidogenic Protein Beta(2)-Microglobulin upon Release from the MHC-1. *J Am Soc Mass Spectrom* **2009**, *20* (2), 278–286. https://doi.org/10.1016/j.jasms.2008.10.005.
(91) Rennella, E.; Corazza, A.; Fogolari, F.; Viglino, P.; Giorgetti, S.; Stoppini, M.; Bellotti, V.; Esposito, G. Equilibrium Unfolding Thermodynamics of Beta2-Microglobulin Analyzed through Native-State H/D Exchange. *Biophys J* **2009**, *96* (1), 169–179. https://doi.org/10.1529/biophysj.108.142448.
(92) Morand, J.; Nunes, A.; Faísca, P. F. N. The Folding Space of Proteinβ2-Microglobulin Is Modulated by a Single Disulfide Bridge. *Phys Biol* **2021**, *18* (5). https://doi.org/10.1088/1478-3975/ac08ec.
(93) Smith, H. I.; Guthertz, N.; Cawood, E. E.; Maya-Martinez, R.; Breeze, A. L.; Radford, S. E. The Role of the IT-State in D76N B2-Microglobulin Amyloid Assembly: A Crucial Intermediate or an Innocuous Bystander? *Journal of Biological Chemistry* **2020**, *295* (35), 12474–12484. https://doi.org/10.1074/jbc.RA120.014901.
(94) Armen, R. S.; Daggett, V. Characterization of Two Distinct Beta2-Microglobulin Unfolding Intermediates That May Lead to Amyloid Fibrils of Different Morphology. *Biochemistry* **2005**, *44* (49), 16098–16107. https://doi.org/10.1021/bi050731h.
(95) Corazza, A.; Rennella, E.; Schanda, P.; Mimmi, M. C.; Cutuil, T.; Raimondi, S.; Giorgetti, S.; Fogolari, F.; Viglino, P.; Frydman, L.; Gal, M.; Bellotti, V.; Brutscher, B.; Esposito, G. Native-Unlike Long-Lived Intermediates along the Folding Pathway of the Amyloidogenic Protein B2-Microglobulin Revealed by Real-

Time Two-Dimensional NMR. *Journal of Biological Chemistry* **2010**, *285* (8), 5827–5835. https://doi.org/10.1074/jbc.M109.061168.
(96) Jahn, T. R.; Parker, M. J.; Homans, S. W.; Radford, S. E. Amyloid Formation under Physiological Conditions Proceeds via a Native-like Folding Intermediate. *Nat Struct Mol Biol* **2006**, *13* (3), 195–201. https://doi.org/10.1038/nsmb1058.
(97) Benseny-Cases, N.; Karamanos, T. K.; Hoop, C. L.; Baum, J.; Radford, S. E. Extracellular Matrix Components Modulate Different Stages in B2-Microglobulin Amyloid Formation. *Journal of Biological Chemistry* **2019**, *294* (24), 9392–9401. https://doi.org/10.1074/jbc.RA119.008300.
(98) Smith, D. P.; Jones, S.; Serpell, L. C.; Sunde, M.; Radford, S. E. A Systematic Investigation into the Effect of Protein Destabilisation on Beta 2-Microglobulin Amyloid Formation. *J Mol Biol* **2003**, *330* (5), 943–954. https://doi.org/10.1016/s0022-2836(03)00687-9.
(99) Iadanza, M. G.; Silvers, R.; Boardman, J.; Smith, H. I.; Karamanos, T. K.; Debelouchina, G. T.; Su, Y.; Griffin, R. G.; Ranson, N. A.; Radford, S. E. The Structure of a B2-Microglobulin Fibril Suggests a Molecular Basis for Its Amyloid Polymorphism. *Nat Commun* **2018**, *9* (1), 4517. https://doi.org/10.1038/s41467-018-06761-6.
(100) Marcinko, T. M.; Dong, J.; LeBlanc, R.; Daborowski, K. V.; Vachet, R. W. Small Molecule-Mediated Inhibition of β-2-Microglobulin-Based Amyloid Fibril Formation. *J Biol Chem* **2017**, *292* (25), 10630–10638. https://doi.org/10.1074/jbc.M116.774083.
(101) Armen, R. S.; DeMarco, M. L.; Alonso, D. O. V.; Daggett, V. Pauling and Corey's Alpha-Pleated Sheet Structure May Define the Prefibrillar Amyloidogenic Intermediate in Amyloid Disease. *Proc Natl Acad Sci U S A* **2004**, *101* (32), 11622–11627. https://doi.org/10.1073/pnas.0401781101.
(102) Stoppini, M.; Bellotti, V. Systemic Amyloidosis: Lessons from B2-Microglobulin *. *Journal of Biological Chemistry* **2015**, *290* (16), 9951–9958. https://doi.org/10.1074/jbc.R115.639799.
(103) Russel, W. B.; Russel, W. B.; Saville, D. A.; Schowalter, W. R. *Colloidal Dispersions*; Cambridge University Press, 1991.
(104) Stetefeld, J.; McKenna, S. A.; Patel, T. R. Dynamic Light Scattering: A Practical Guide and Applications in Biomedical Sciences. *Biophys Rev* **2016**, *8* (4), 409–427. https://doi.org/10.1007/s12551-016-0218-6.
(105) Weiss, J. N. Dynamic Light Scattering (DLS) Spectroscopy. In *Dynamic Light Scattering Spectroscopy of the Human Eye*; Weiss, J. N., Ed.; Springer International Publishing: Cham, 2022; pp 13–17. https://doi.org/10.1007/978-3-031-06624-5_3.
(106) Pecora, R. Introduction. In *Dynamic Light Scattering: Applications of Photon Correlation Spectroscopy*; Pecora, R., Ed.; Springer US: Boston, MA, 1985; pp 1–6. https://doi.org/10.1007/978-1-4613-2389-1_1.
(107) Carpenter, D. K. Dynamic Light Scattering with Applications to Chemistry, Biology, and Physics (Berne, Bruce J.; Pecora, Robert). *J. Chem. Educ.* **1977**, *54* (10), A430. https://doi.org/10.1021/ed054pA430.1.
(108) *Protein: A Comprehensive Treatise. Vol. 2*; Allen, G., Ed.; JAI Press: Greenwich, Conn. London, 1999; Vol. 2.

(109) Burchard, W. Static and Dynamic Light Scattering from Branched Polymers and Biopolymers. In *Light Scattering from Polymers*; Advances in Polymer Science; Springer Berlin Heidelberg: Berlin, Heidelberg, 1983; Vol. 48, pp 1–124. https://doi.org/10.1007/3-540-12030-0_1.
(110) Yudin, I. K.; Nikolaenko, G. L.; Kosov, V. I.; Agayan, V. A.; Anisimov, M. A.; Sengers, J. V. A Compact Photon-Correlation Spectrometer for Research and Education. *Int J Thermophys* **1997**, *18* (5), 1237–1248. https://doi.org/10.1007/BF02575258.
(111) *Fluorescence spectroscopy - Latest research and news | Nature*. https://www.nature.com/subjects/fluorescence-spectrometry (accessed 2022-11-04).
(112) *Principles of Fluorescence Spectroscopy*; Lakowicz, J. R., Ed.; Springer US: Boston, MA, 2006. https://doi.org/10.1007/978-0-387-46312-4.
(113) *Fluorescence Microscopy - Basic Concepts in Fluorescence | Olympus LS*. https://www.olympus-lifescience.com/en/microscope-resource/primer/techniques/fluorescence/fluorescenceintro/ (accessed 2022-11-05).
(114) *Fluorescence Process - US*. https://www.thermofisher.com/us/en/home/life-science/cell-analysis/cell-analysis-learning-center/molecular-probes-school-of-fluorescence/fluorescence-basics/fluorescence-fundamentals/process-fluorescence.html (accessed 2022-11-05).
(115) Matuszewska, A.; Czaja, M.; Matuszewska, A.; Czaja, M. *The Use of Synchronous Fluorescence Technique in Environmental Investigations of Polycyclic Aromatic Hydrocarbons in Airborne Particulate Matter from an Industrial Region in Poland*; IntechOpen, 2020. https://doi.org/10.5772/intechopen.92402.
(116) Jabłoński, A. Über Den Mechanismus Der Photolumineszenz von Farbstoffphosphoren. *Zeitschrift fur Physik* **1935**, *94*, 38–46. https://doi.org/10.1007/BF01330795.
(117) Lakowicz, J. R. Radiative Decay Engineering: Biophysical and Biomedical Applications. *Anal Biochem* **2001**, *298* (1), 1–24. https://doi.org/10.1006/abio.2001.5377.
(118) Pham, H.; Miller, L. W. Chapter Nine - Lanthanide-Based Resonance Energy Transfer Biosensors for Live-Cell Applications. In *Methods in Enzymology*; Cotruvo, J. A., Ed.; Rare-Earth Element Biochemistry: Characterization and Applications of Lanthanide-Binding Biomolecules; Academic Press, 2021; Vol. 651, pp 291–311. https://doi.org/10.1016/bs.mie.2021.01.010.
(119) Mallia, R.; Narayanan, S. Photodiagnosis of Oral Malignancy Using Laser-Induced Fluorescence and Diffuse Reflectance Spectroscopy. **2010**.
(120) Stokes, G. G. XXX. On the Change of Refrangibility of Light. *Philosophical Transactions of the Royal Society of London* **1852**, *142*, 463–562. https://doi.org/10.1098/rstl.1852.0022.
(121) Sharma, A.; Schulman, S. G. *Introduction to Fluorescence Spectroscopy*; Wiley, 1999.
(122) Stokes Shift. *Wikipedia*; 2022.
(123) Mukherjee, M.; Ghosh, R.; Chattopadhyay, K.; Ghosh, S. Stepwise Unfolding of a Multi-Tryptophan Protein MPT63 with Immunoglobulin-like Fold: Detection of Zone-Wise Perturbation during Guanidine Hydrochloride-Induced Unfolding Using

Phosphorescence Spectroscopy. *RSC Adv.* **2016**, *6* (66), 61077–61087. https://doi.org/10.1039/C6RA06545G.
(124) Niehaus, J. *Fluorescent Proteins 101: Introduction to FRET*. https://blog.addgene.org/introduction-to-fret (accessed 2022-11-07).
(125) Broussard, J. A.; Green, K. J. Research Techniques Made Simple: Methodology and Applications of Förster Resonance Energy Transfer (FRET) Microscopy. *Journal of Investigative Dermatology* **2017**, *137* (11), e185–e191. https://doi.org/10.1016/j.jid.2017.09.006.
(126) Skruzny, M.; Pohl, E.; Abella, M. FRET Microscopy in Yeast. *Biosensors* **2019**, *9* (4), 122. https://doi.org/10.3390/bios9040122.
(127) Suddala, K. C.; Walter, N. G. Chapter Fifteen - Riboswitch Structure and Dynamics by SmFRET Microscopy. In *Methods in Enzymology*; Burke-Aguero, D. H., Ed.; Riboswitch Discovery, Structure and Function; Academic Press, 2014; Vol. 549, pp 343–373. https://doi.org/10.1016/B978-0-12-801122-5.00015-5.
(128) Mukhopadhyay, S.; Krishnan, R.; Lemke, E. A.; Lindquist, S.; Deniz, A. A. A Natively Unfolded Yeast Prion Monomer Adopts an Ensemble of Collapsed and Rapidly Fluctuating Structures. *Proceedings of the National Academy of Sciences* **2007**, *104* (8), 2649–2654. https://doi.org/10.1073/pnas.0611503104.
(129) Weiss, S. Fluorescence Spectroscopy of Single Biomolecules. *Science* **1999**, *283* (5408), 1676–1683. https://doi.org/10.1126/science.283.5408.1676.
(130) Kapanidis, A. N.; Laurence, T. A.; Lee, N. K.; Margeat, E.; Kong, X.; Weiss, S. Alternating-Laser Excitation of Single Molecules. *Acc Chem Res* **2005**, *38* (7), 523–533. https://doi.org/10.1021/ar0401348.
(131) Michalet, X.; Weiss, S.; Jäger, M. Single-Molecule Fluorescence Studies of Protein Folding and Conformational Dynamics. *Chem Rev* **2006**, *106* (5), 1785–1813. https://doi.org/10.1021/cr0404343.
(132) Seidel, R.; Dekker, C. Single-Molecule Studies of Nucleic Acid Motors. *Current Opinion in Structural Biology* **2007**, *17* (1), 80–86. https://doi.org/10.1016/j.sbi.2006.12.003.
(133) Deniz, A. A.; Dahan, M.; Grunwell, J. R.; Ha, T.; Faulhaber, A. E.; Chemla, D. S.; Weiss, S.; Schultz, P. G. Single-Pair Fluorescence Resonance Energy Transfer on Freely Diffusing Molecules: Observation of Förster Distance Dependence and Subpopulations. *Proceedings of the National Academy of Sciences* **1999**, *96* (7), 3670–3675. https://doi.org/10.1073/pnas.96.7.3670.
(134) Ka, M.; Rb, B.; Jm, L.; Iv, G.; Wa, E. Characterizing the Unfolded States of Proteins Using Single-Molecule FRET Spectroscopy and Molecular Simulations. *Proceedings of the National Academy of Sciences of the United States of America* **2007**, *104* (5). https://doi.org/10.1073/pnas.0607097104.
(135) Schuler, B.; Eaton, W. A. Protein Folding Studied by Single-Molecule FRET. *Curr Opin Struct Biol* **2008**, *18* (1), 16–26. https://doi.org/10.1016/j.sbi.2007.12.003.
(136) Lerner, E.; Cordes, T.; Ingargiola, A.; Alhadid, Y.; Chung, S.; Michalet, X.; Weiss, S. Toward Dynamic Structural Biology: Two Decades of Single-Molecule Förster Resonance Energy Transfer. *Science* **2018**, *359* (6373), eaan1133. https://doi.org/10.1126/science.aan1133.
(137) Ha, T.; Ting, A. Y.; Liang, J.; Caldwell, W. B.; Deniz, A. A.; Chemla, D. S.; Schultz, P. G.; Weiss, S. Single-Molecule Fluorescence Spectroscopy of Enzyme

Conformational Dynamics and Cleavage Mechanism. *Proceedings of the National Academy of Sciences* **1999**, *96* (3), 893–898. https://doi.org/10.1073/pnas.96.3.893.
(138) Yu, L.; Lei, Y.; Ma, Y.; Liu, M.; Zheng, J.; Dan, D.; Gao, P. A Comprehensive Review of Fluorescence Correlation Spectroscopy. *Frontiers in Physics* **2021**, *9*.
(139) Banachowicz, E.; Patkowski, A.; Meier, G.; Klamecka, K.; Gapiński, J. Successful FCS Experiment in Nonstandard Conditions. *Langmuir* **2014**, *30* (29), 8945–8955. https://doi.org/10.1021/la5015708.
(140) Rigler, R.; Mets, U. Diffusion of Single Molecules through a Gaussian Laser Beam. In *Laser Spectroscopy of Biomolecules*; SPIE, 1993; Vol. 1921, pp 239–248. https://doi.org/10.1117/12.146154.
(141) Kapusta, P.; Wahl, M.; GmbH, P.; Benda, A.; Hof, M.; Enderlein, J. FLCS – Fluorescence Lifetime Correlation Spectroscopy. **2006**, 5.
(142) Ohrt, T.; Mütze, J.; Staroske, W.; Weinmann, L.; Höck, J.; Crell, K.; Meister, G.; Schwille, P. Fluorescence Correlation Spectroscopy and Fluorescence Cross-Correlation Spectroscopy Reveal the Cytoplasmic Origination of Loaded Nuclear RISC in Vivo in Human Cells. *Nucleic Acids Research* **2008**, *36* (20), 6439–6449. https://doi.org/10.1093/nar/gkn693.
(143) Sahoo, B.; Drombosky, K.; Wetzel, R. Fluorescence Correlation Spectroscopy: A Tool to Study Protein Oligomerization and Aggregation In Vitro and In Vivo. *Methods Mol. Biol.* **2015**, *1345*, 67–87. https://doi.org/10.1007/978-1-4939-2978-8_5.
(144) Ohrt, T.; Mütze, J.; Staroske, W.; Weinmann, L.; Höck, J.; Crell, K.; Meister, G.; Schwille, P. Fluorescence Correlation Spectroscopy and Fluorescence Cross-Correlation Spectroscopy Reveal the Cytoplasmic Origination of Loaded Nuclear RISC in Vivo in Human Cells. *Nucleic Acids Research* **2008**, *36* (20), 6439–6449. https://doi.org/10.1093/nar/gkn693.
(145) Gurunathan, K.; Levitus, M. FRET Fluctuation Spectroscopy of Diffusing Biopolymers: Contributions of Conformational Dynamics and Translational Diffusion. *J. Phys. Chem. B* **2010**, *114* (2), 980–986. https://doi.org/10.1021/jp907390n.
(146) Torres, T.; Levitus, M. Measuring Conformational Dynamics: A New FCS-FRET Approach. *J. Phys. Chem. B* **2007**, *111* (25), 7392–7400. https://doi.org/10.1021/jp070659s.
(147) Ferreon, A. C. M.; Gambin, Y.; Lemke, E. A.; Deniz, A. A. Interplay of -Synuclein Binding and Conformational Switching Probed by Single-Molecule Fluorescence. *Proceedings of the National Academy of Sciences* **2009**, *106* (14), 5645–5650. https://doi.org/10.1073/pnas.0809232106.
(148) Santoso, Y.; Joyce, C. M.; Potapova, O.; Le Reste, L.; Hohlbein, J.; Torella, J. P.; Grindley, N. D. F.; Kapanidis, A. N. Conformational Transitions in DNA Polymerase I Revealed by Single-Molecule FRET. *Proceedings of the National Academy of Sciences* **2010**, *107* (2), 715–720. https://doi.org/10.1073/pnas.0910909107.
(149) Narhi, L. O.; Schmit, J.; Bechtold-Peters, K.; Sharma, D. Classification of Protein Aggregates. *Journal of Pharmaceutical Sciences* **2012**, *101* (2), 493–498. https://doi.org/10.1002/jps.22790.

(150) Ross, C. A.; Poirier, M. A. What Is the Role of Protein Aggregation in Neurodegeneration? *Nature Reviews Molecular Cell Biology* **2005**, *6* (11), 891–898. https://doi.org/10.1038/nrm1742.
(151) Majhi, P. R.; Ganta, R. R.; Vanam, R. P.; Seyrek, E.; Giger, K.; Dubin, P. L. Electrostatically Driven Protein Aggregation: β-Lactoglobulin at Low Ionic Strength. *Langmuir* **2006**, *22* (22), 9150–9159. https://doi.org/10.1021/la053528w.
(152) Eisele, Y. S.; Monteiro, C.; Fearns, C.; Encalada, S. E.; Wiseman, R. L.; Powers, E. T.; Kelly, J. W. Targeting Protein Aggregation for the Treatment of Degenerative Diseases. *Nature Reviews Drug Discovery* **2015**, *14* (11), 759–780. https://doi.org/10.1038/nrd4593.
(153) Wang, W.; Roberts, C. J. Protein Aggregation – Mechanisms, Detection, and Control. *International Journal of Pharmaceutics* **2018**, *550* (1–2), 251–268. https://doi.org/10.1016/j.ijpharm.2018.08.043.
(154) Philo, J. S.; Arakawa, T. Mechanisms of Protein Aggregation. *Curr Pharm Biotechnol* **2009**, *10* (4), 348–351. https://doi.org/10.2174/138920109788488932.
(155) Gu, L. C.; Erdös, E. A.; Chiang, H. S.; Calderwood, T.; Tsai, K.; Visor, G. C.; Duffy, J.; Hsu, W. C.; Foster, L. C. Stability of Interleukin 1 Beta (IL-1 Beta) in Aqueous Solution: Analytical Methods, Kinetics, Products, and Solution Formulation Implications. *Pharm. Res.* **1991**, *8* (4), 485–490. https://doi.org/10.1023/a:1015851228163.
(156) Tsai, A. M.; van Zanten, J. H.; Betenbaugh, M. J. II. Electrostatic Effect in the Aggregation of Heat-Denatured RNase A and Implications for Protein Additive Design. *Biotechnol. Bioeng.* **1998**, *59* (3), 281–285.
(157) Maa, Y. F.; Hsu, C. C. Protein Denaturation by Combined Effect of Shear and Air-Liquid Interface. *Biotechnol. Bioeng.* **1997**, *54* (6), 503–512. https://doi.org/10.1002/(SICI)1097-0290(19970620)54:6<503::AID-BIT1>3.0.CO;2-N.
(158) Stradner, A.; Sedgwick, H.; Cardinaux, F.; Poon, W. C. K.; Egelhaaf, S. U.; Schurtenberger, P. Equilibrium Cluster Formation in Concentrated Protein Solutions and Colloids. *Nature* **2004**, *432* (7016), 492–495. https://doi.org/10.1038/nature03109.
(159) Šarić, A.; Chebaro, Y. C.; Knowles, T. P. J.; Frenkel, D. Crucial Role of Nonspecific Interactions in Amyloid Nucleation. *PNAS* **2014**, *111* (50), 17869–17874. https://doi.org/10.1073/pnas.1410159111.
(160) Wang, W. Protein Aggregation and Its Inhibition in Biopharmaceutics. *Int J Pharm* **2005**, *289* (1–2), 1–30. https://doi.org/10.1016/j.ijpharm.2004.11.014.
(161) Roberts, C. J. Therapeutic Protein Aggregation: Mechanisms, Design, and Control. *Trends in Biotechnology* **2014**, *32* (7), 372–380. https://doi.org/10.1016/j.tibtech.2014.05.005.
(162) Takata, S.; Norisuye, T.; Tanaka, N.; Shibayama, M. Heat-Induced Gelation of β-Lactoglobulin. 1. Time-Resolved Dynamic Light Scattering. *Macromolecules* **2000**, *33* (15), 5470–5475. https://doi.org/10.1021/ma0003295.
(163) Mine, Y. Recent Advances in the Understanding of Egg White Protein Functionality. *Trends in Food Science & Technology* **1995**, *6* (7), 225–232. https://doi.org/10.1016/S0924-2244(00)89083-4.

(164) Aymard, P.; Gimel, J. C.; Nicolai, T.; Durand, D. Experimental Evidence for a Two-Step Process in the Aggregation of β-Lactoglobulin at PH 7. *J. Chim. Phys.* **1996**, *93*, 987–997. https://doi.org/10.1051/jcp/1996930987.
(165) Nicolai, T.; Urban, C.; Schurtenberger, P. Light Scattering Study of Turbid Heat-Set Globular Protein Gels Using Cross-Correlation Dynamic Light Scattering. *J Colloid Interface Sci* **2001**, *240* (2), 419–424. https://doi.org/10.1006/jcis.2001.7672.
(166) Mezzenga, R.; Fischer, P. The Self-Assembly, Aggregation and Phase Transitions of Food Protein Systems in One, Two and Three Dimensions. *Rep Prog Phys* **2013**, *76* (4), 046601. https://doi.org/10.1088/0034-4885/76/4/046601.
(167) Li, Y.; Lubchenko, V.; Vorontsova, M. A.; Filobelo, L.; Vekilov, P. G. Ostwald-Like Ripening of the Anomalous Mesoscopic Clusters in Protein Solutions. *J. Phys. Chem. B* **2012**, *116* (35), 10657–10664. https://doi.org/10.1021/jp303316s.
(168) Vorontsova, M. A.; Chan, H. Y.; Lubchenko, V.; Vekilov, P. G. Lack of Dependence of the Sizes of the Mesoscopic Protein Clusters on Electrostatics. *Biophysical Journal* **2015**, *109* (9), 1959–1968. https://doi.org/10.1016/j.bpj.2015.09.025.
(169) Pan, W.; Vekilov, P. G.; Lubchenko, V. Origin of Anomalous Mesoscopic Phases in Protein Solutions. *J. Phys. Chem. B* **2010**, *114* (22), 7620–7630. https://doi.org/10.1021/jp100617w.
(170) Safari, M. S.; Byington, M. C.; Conrad, J. C.; Vekilov, P. G. Polymorphism of Lysozyme Condensates. *J. Phys. Chem. B* **2017**, *121* (39), 9091–9101. https://doi.org/10.1021/acs.jpcb.7b05425.
(171) Vekilov, P. G.; McCabe, J. W.; Angel, L. A.; Hawke, D. H.; Byington, M. C.; Safari, M. S.; Lubchenko, V.; Conrad, J. C. Weakly-Bound Dimers That Underlie the Crystal Nucleation Precursors in Lysozyme Solutions. *bioRxiv* **2018**, 275222. https://doi.org/10.1101/275222.
(172) Nikfarjam, S.; Ghorbani, M.; Adhikari, S.; Karlsson, A. J.; Jouravleva, E. V.; Woehl, T. J.; Anisimov, M. A. Irreversible Nature of Mesoscopic Aggregates in Lysozyme Solutions. *Colloid J* **2019**, *81* (5), 546–554. https://doi.org/10.1134/S1061933X19050090.
(173) Pecora, R. Dynamic Light Scattering Measurement of Nanometer Particles in Liquids. *Journal of Nanoparticle Research* **2000**, *2* (2), 123–131. https://doi.org/10.1023/A:1010067107182.
(174) Zheng, X.; Anisimov, M. A.; Sengers, J. V.; He, M. Mesoscopic Diffusion of Poly(Ethylene Oxide) in Pure and Mixed Solvents. *The Journal of Physical Chemistry B* **2018**, *122* (13), 3454–3464. https://doi.org/10.1021/acs.jpcb.7b10420.
(175) Weitz, D. A.; Huang, J. S.; Lin, M. Y.; Sung, J. Limits of the Fractal Dimension for Irreversible Kinetic Aggregation of Gold Colloids. *Phys. Rev. Lett.* **1985**, *54* (13), 1416–1419. https://doi.org/10.1103/PhysRevLett.54.1416.
(176) Breure, B.; Subramanian, D.; Leys, J.; Peters, C. J.; Anisimov, M. A. Modeling Asphaltene Aggregation with a Single Compound. *Energy Fuels* **2013**, *27* (1), 172–176. https://doi.org/10.1021/ef3016766.
(177) Kryven, I.; Lazzari, S.; Storti, G. Population Balance Modeling of Aggregation and Coalescence in Colloidal Systems. *Macromolecular Theory and Simulations* **2014**, *23* (3), 170–181. https://doi.org/10.1002/mats.201300140.

(178) Avanti, C.; Saluja, V.; van Streun, E. L. P.; Frijlink, H. W.; Hinrichs, W. L. J. Stability of Lysozyme in Aqueous Extremolyte Solutions during Heat Shock and Accelerated Thermal Conditions. *PLoS One* **2014**, *9* (1). https://doi.org/10.1371/journal.pone.0086244.
(179) Lesturgeon, V.; Nicolai, T.; Durand, D. Dynamic and Static Light Scattering Study of the Formation of Cross-Linked PMMA Gels. *Eur. Phys. J. B* **1999**, *9* (1), 71–82. https://doi.org/10.1007/s100510050743.
(180) Martin, J. E.; Wilcoxon, J.; Odinek, J. Decay of Density Fluctuations in Gels. *Phys. Rev. A* **1991**, *43* (2), 858–872. https://doi.org/10.1103/PhysRevA.43.858.
(181) Nicolai, T.; Urban, C.; Schurtenberger, P. Light Scattering Study of Turbid Heat-Set Globular Protein Gels Using Cross-Correlation Dynamic Light Scattering. *J Colloid Interface Sci* **2001**, *240* (2), 419–424. https://doi.org/10.1006/jcis.2001.7672.
(182) Tsurusawa, H.; Leocmach, M.; Russo, J.; Tanaka, H. Direct Link between Mechanical Stability in Gels and Percolation of Isostatic Particles. *Science Advances* **2019**, *5* (5), eaav6090. https://doi.org/10.1126/sciadv.aav6090.
(183) Zimmerman, J. K. Biological Thermodynamics, 2nd Edition by Donald T. Haynie. *Biochemistry and Molecular Biology Education* **2009**, *37* (2), 133–133. https://doi.org/10.1002/bmb.20274.
(184) Li-Blatter, X.; Seelig, J. Thermal and Chemical Unfolding of Lysozyme. Multistate Zimm–Bragg Theory Versus Two-State Model. *J. Phys. Chem. B* **2019**, *123* (48), 10181–10191. https://doi.org/10.1021/acs.jpcb.9b08816.
(185) Lindorff-Larsen, K.; Piana, S.; Dror, R. O.; Shaw, D. E. How Fast-Folding Proteins Fold. *Science* **2011**, *334* (6055), 517–520. https://doi.org/10.1126/science.1208351.
(186) Matagne, A.; Radford, S. E.; Dobson, C. M. Fast and Slow Tracks in Lysozyme Folding: Insight into the Role of Domains in the Folding Process. *J. Mol. Biol.* **1997**, *267* (5), 1068–1074. https://doi.org/10.1006/jmbi.1997.0963.
(187) Chung, H. S.; Eaton, W. A. Protein Folding Transition Path Times from Single Molecule FRET. *Curr. Opin. Struct. Biol.* **2018**, *48*, 30–39. https://doi.org/10.1016/j.sbi.2017.10.007.
(188) Weijers, M.; Barneveld, P. A.; Cohen Stuart, M. A.; Visschers, R. W. Heat-Induced Denaturation and Aggregation of Ovalbumin at Neutral PH Described by Irreversible First-Order Kinetics. *Protein Sci* **2003**, *12* (12), 2693–2703.
(189) Woodard, D.; Bell, D.; Tipton, D.; Durrance, S.; Cole, L.; Li, B.; Xu, S. Gel Formation in Protein Amyloid Aggregation: A Physical Mechanism for Cytotoxicity. *PLOS ONE* **2014**, *9* (4), e94789. https://doi.org/10.1371/journal.pone.0094789.
(190) Renkema, J. M. S.; van Vliet, T. Heat-Induced Gel Formation by Soy Proteins at Neutral PH. *J. Agric. Food Chem.* **2002**, *50* (6), 1569–1573. https://doi.org/10.1021/jf010763l.
(191) Ako, K.; Nicolai, T.; Durand, D. Salt-Induced Gelation of Globular Protein Aggregates: Structure and Kinetics. *Biomacromolecules* **2010**, *11* (4), 864–871. https://doi.org/10.1021/bm9011437.
(192) Šarić, A.; Buell, A. K.; Meisl, G.; Michaels, T. C. T.; Dobson, C. M.; Linse, S.; Knowles, T. P. J.; Frenkel, D. Physical Determinants of the Self-Replication of Protein Fibrils. *Nature Physics* **2016**, *12* (9), 874–880. https://doi.org/10.1038/nphys3828.

(193) James, D.; Beairsto, S.; Hartt, C.; Zavalov, O.; Saika-Voivod, I.; Bowles, R. K.; Poole, P. H. Phase Transitions in Fluctuations and Their Role in Two-Step Nucleation. *J. Chem. Phys.* **2019**, *EDCH2019* (1), 074501. https://doi.org/10.1063/1.5057429@jcp.2020.EDCH2019.issue-1.
(194) Wierenga, H.; Wolde, P. R. T. Diffusible Cross-Linkers Cause Superexponential Friction Forces. *Phys Rev Lett* **2020**, *125* (7), 078101. https://doi.org/10.1103/PhysRevLett.125.078101.
(195) Clark, A. G.; Paluch, E. Mechanics and Regulation of Cell Shape during the Cell Cycle. *Results Probl Cell Differ* **2011**, *53*, 31–73. https://doi.org/10.1007/978-3-642-19065-0_3.
(196) Hess, H.; Ross, J. L. Non-Equilibrium Assembly of Microtubules: From Molecules to Autonomous Chemical Robots. *Chem. Soc. Rev.* **2017**, *46* (18), 5570–5587. https://doi.org/10.1039/C7CS00030H.
(197) Carlier, M. F.; Pantaloni, D. Control of Actin Dynamics in Cell Motility. *J Mol Biol* **1997**, *269* (4), 459–467. https://doi.org/10.1006/jmbi.1997.1062.
(198) Blanchoin, L.; Boujemaa-Paterski, R.; Sykes, C.; Plastino, J. Actin Dynamics, Architecture, and Mechanics in Cell Motility. *Physiological Reviews* **2014**, *94* (1), 235–263. https://doi.org/10.1152/physrev.00018.2013.
(199) Weißenfels, M.; Gemen, J.; Klajn, R. Dissipative Self-Assembly: Fueling with Chemicals versus Light. *Chem* **2021**, *7* (1), 23–37. https://doi.org/10.1016/j.chempr.2020.11.025.
(200) Chien, M.-P.; Rush, A. M.; Thompson, M. P.; Gianneschi, N. C. Programmable Shape-Shifting Micelles. *Angewandte Chemie International Edition* **2010**, *49* (30), 5076–5080. https://doi.org/10.1002/anie.201000265.
(201) Wang, X.; Guerin, G.; Wang, H.; Wang, Y.; Manners, I.; Winnik, M. A. Cylindrical Block Copolymer Micelles and Co-Micelles of Controlled Length and Architecture. *Science* **2007**, *317* (5838), 644–647. https://doi.org/10.1126/science.1141382.
(202) Shevchenko, E. V.; Talapin, D. V.; Kotov, N. A.; O'Brien, S.; Murray, C. B. Structural Diversity in Binary Nanoparticle Superlattices. *Nature* **2006**, *439* (7072), 55–59. https://doi.org/10.1038/nature04414.
(203) Macfarlane, R. J.; Jones, M. R.; Lee, B.; Auyeung, E.; Mirkin, C. A. Topotactic Interconversion of Nanoparticle Superlattices. *Science* **2013**, *341* (6151), 1222–1225. https://doi.org/10.1126/science.1241402.
(204) Grötsch, R. K.; Wanzke, C.; Speckbacher, M.; Angı, A.; Rieger, B.; Boekhoven, J. Pathway Dependence in the Fuel-Driven Dissipative Self-Assembly of Nanoparticles. *J. Am. Chem. Soc.* **2019**, *141* (25), 9872–9878. https://doi.org/10.1021/jacs.9b02004.
(205) Boekhoven, J.; Hendriksen, W. E.; Koper, G. J. M.; Eelkema, R.; van Esch, J. H. Transient Assembly of Active Materials Fueled by a Chemical Reaction. *Science* **2015**, *349* (6252), 1075–1079. https://doi.org/10.1126/science.aac6103.
(206) Rossum, S. A. P. van; Tena-Solsona, M.; Esch, J. H. van; Eelkema, R.; Boekhoven, J. Dissipative Out-of-Equilibrium Assembly of Man-Made Supramolecular Materials. *Chemical Society Reviews* **2017**, *46* (18), 5519–5535. https://doi.org/10.1039/C7CS00246G.

(207) Esch, J. H. van; Klajn, R.; Otto, S. Chemical Systems out of Equilibrium. *Chem. Soc. Rev.* **2017**, *46* (18), 5474–5475. https://doi.org/10.1039/C7CS90088K.
(208) Tena-Solsona, M.; Rieß, B.; Grötsch, R. K.; Löhrer, F. C.; Wanzke, C.; Käsdorf, B.; Bausch, A. R.; Müller-Buschbaum, P.; Lieleg, O.; Boekhoven, J. Non-Equilibrium Dissipative Supramolecular Materials with a Tunable Lifetime. *Nat Commun* **2017**, *8* (1), 15895. https://doi.org/10.1038/ncomms15895.
(209) Jeong, B.; Kim, S. W.; Bae, Y. H. Thermosensitive Sol–Gel Reversible Hydrogels. *Advanced Drug Delivery Reviews* **2002**, *54* (1), 37–51. https://doi.org/10.1016/S0169-409X(01)00242-3.
(210) Zhang, Y. S.; Khademhosseini, A. Advances in Engineering Hydrogels. *Science* **2017**, *356* (6337), eaaf3627. https://doi.org/10.1126/science.aaf3627.
(211) Ogden, W. A.; Guan, Z. Redox Chemical-Fueled Dissipative Self-Assembly of Active Materials. *ChemSystemsChem* **2020**, *2* (4), e1900030. https://doi.org/10.1002/syst.201900030.
(212) te Brinke, E.; Groen, J.; Herrmann, A.; Heus, H. A.; Rivas, G.; Spruijt, E.; Huck, W. T. S. Dissipative Adaptation in Driven Self-Assembly Leading to Self-Dividing Fibrils. *Nature Nanotech* **2018**, *13* (9), 849–855. https://doi.org/10.1038/s41565-018-0192-1.
(213) van Ravensteijn, B. G. P.; Hendriksen, W. E.; Eelkema, R.; van Esch, J. H.; Kegel, W. K. Fuel-Mediated Transient Clustering of Colloidal Building Blocks. *J. Am. Chem. Soc.* **2017**, *139* (29), 9763–9766. https://doi.org/10.1021/jacs.7b03263.
(214) Makey, G.; Galioglu, S.; Ghaffari, R.; Engin, E. D.; Yıldırım, G.; Yavuz, Ö.; Bektaş, O.; Nizam, Ü. S.; Akbulut, Ö.; Şahin, Ö.; Güngör, K.; Dede, D.; Demir, H. V.; Ilday, F. Ö.; Ilday, S. Universality of Dissipative Self-Assembly from Quantum Dots to Human Cells. *Nat. Phys.* **2020**, *16* (7), 795–801. https://doi.org/10.1038/s41567-020-0879-8.
(215) Wanzke, C.; Jussupow, A.; Kohler, F.; Dietz, H.; Kaila, V. R. I.; Boekhoven, J. Dynamic Vesicles Formed By Dissipative Self-Assembly. *ChemSystemsChem* **2020**, *2* (1), e1900044. https://doi.org/10.1002/syst.201900044.
(216) Wood, C. S.; Browne, C.; Wood, D. M.; Nitschke, J. R. Fuel-Controlled Reassembly of Metal–Organic Architectures. *ACS Cent. Sci.* **2015**, *1* (9), 504–509. https://doi.org/10.1021/acscentsci.5b00279.
(217) Pezzato, C.; Prins, L. J. Transient Signal Generation in a Self-Assembled Nanosystem Fueled by ATP. *Nat Commun* **2015**, *6* (1), 7790. https://doi.org/10.1038/ncomms8790.
(218) De, S.; Klajn, R. Dissipative Self-Assembly Driven by the Consumption of Chemical Fuels. *Advanced Materials* **2018**, *30* (41), 1706750. https://doi.org/10.1002/adma.201706750.
(219) Dhiman, S.; Jain, A.; Kumar, M.; George, S. J. Adenosine-Phosphate-Fueled, Temporally Programmed Supramolecular Polymers with Multiple Transient States. *J. Am. Chem. Soc.* **2017**, *139* (46), 16568–16575. https://doi.org/10.1021/jacs.7b07469.
(220) Hao, X.; Sang, W.; Hu, J.; Yan, Q. Pulsating Polymer Micelles via ATP-Fueled Dissipative Self-Assembly. *ACS Macro Lett.* **2017**, *6* (10), 1151–1155. https://doi.org/10.1021/acsmacrolett.7b00649.
(221) Tena-Solsona, M.; Janssen, J.; Wanzke, C.; Schnitter, F.; Park, H.; Rieß, B.; Gibbs, J. M.; Weber, C. A.; Boekhoven, J. Accelerated Ripening in Chemically

Fueled Emulsions**. *ChemSystemsChem* **2021**, *3* (2), e2000034. https://doi.org/10.1002/syst.202000034.
(222) Singh, N.; Formon, G. J. M.; De Piccoli, S.; Hermans, T. M. Devising Synthetic Reaction Cycles for Dissipative Nonequilibrium Self-Assembly. *Advanced Materials* **2020**, *32* (20), 1906834. https://doi.org/10.1002/adma.201906834.
(223) Fialkowski, M.; Bishop, K. J. M.; Klajn, R.; Smoukov, S. K.; Campbell, C. J.; Grzybowski, B. A. Principles and Implementations of Dissipative (Dynamic) Self-Assembly. *J. Phys. Chem. B* **2006**, *110* (6), 2482–2496. https://doi.org/10.1021/jp054153q.
(224) Kong, N.; Fu, L.; Peng, Q.; Li, H. Metal Chelation Dynamically Regulates the Mechanical Properties of Engineered Protein Hydrogels. *ACS Biomater. Sci. Eng.* **2017**, *3* (5), 742–749. https://doi.org/10.1021/acsbiomaterials.6b00374.
(225) Hughes, M. D. G.; Cussons, S.; Mahmoudi, N.; Brockwell, D. J.; Dougan, L. Tuning Protein Hydrogel Mechanics through Modulation of Nanoscale Unfolding and Entanglement in Postgelation Relaxation. *ACS Nano* **2022**. https://doi.org/10.1021/acsnano.2c02369.
(226) G. Hughes, M. D.; Cussons, S.; Mahmoudi, N.; J. Brockwell, D.; Dougan, L. Single Molecule Protein Stabilisation Translates to Macromolecular Mechanics of a Protein Network. *Soft Matter* **2020**, *16* (27), 6389–6399. https://doi.org/10.1039/C9SM02484K.
(227) Hughes, M. D. G.; Hanson, B. S.; Cussons, S.; Mahmoudi, N.; Brockwell, D. J.; Dougan, L. Control of Nanoscale In Situ Protein Unfolding Defines Network Architecture and Mechanics of Protein Hydrogels. *ACS Nano* **2021**, *15* (7), 11296–11308. https://doi.org/10.1021/acsnano.1c00353.
(228) PaulRussoLSU2012DLS_Minicourse.Pdf. https://www.eng.uc.edu/~beaucag/Classes/Characterization/DLS/PaulRussoLSU2012DLS_Minicourse.pdf (accessed 2022-06-30).
(229) Branigan, E.; Pliotas, C.; Hagelueken, G.; Naismith, J. H. Quantification of Free Cysteines in Membrane and Soluble Proteins Using a Fluorescent Dye and Thermal Unfolding. *Nat Protoc* **2013**, *8* (11), 10.1038/nprot.2013.128. https://doi.org/10.1038/nprot.2013.128.
(230) *Biomolecules | Free Full-Text | Effects of Protein Unfolding on Aggregation and Gelation in Lysozyme Solutions*. https://www.mdpi.com/2218-273X/10/9/1262 (accessed 2022-07-05).
(231) Santra, M. K.; Banerjee, A.; Rahaman, O.; Panda, D. Unfolding Pathways of Human Serum Albumin: Evidence for Sequential Unfolding and Folding of Its Three Domains. *International Journal of Biological Macromolecules* **2005**, *37* (4), 200–204. https://doi.org/10.1016/j.ijbiomac.2005.10.009.
(232) Sánchez-Morán, H.; Weltz, J. S.; Schwartz, D. K.; Kaar, J. L. Understanding Design Rules for Optimizing the Interface between Immobilized Enzymes and Random Copolymer Brushes. *ACS Appl Mater Interfaces* **2021**, *13* (23), 26694–26703. https://doi.org/10.1021/acsami.1c02443.
(233) Tien, M. Z.; Meyer, A. G.; Sydykova, D. K.; Spielman, S. J.; Wilke, C. O. Maximum Allowed Solvent Accessibilites of Residues in Proteins. *PLoS One* **2013**, *8* (11), e80635. https://doi.org/10.1371/journal.pone.0080635.

(234) Geisbrecht, B. V.; Bouyain, S.; Pop, M. An Optimized System for Expression and Purification of Secreted Bacterial Proteins. *Protein Expression and Purification* **2006**, *46* (1), 23–32. https://doi.org/10.1016/j.pep.2005.09.003.
(235) Naeem, A.; Fazili, N. A. Defective Protein Folding and Aggregation as the Basis of Neurodegenerative Diseases: The Darker Aspect of Proteins. *Cell Biochem Biophys* **2011**, *61* (2), 237–250. https://doi.org/10.1007/s12013-011-9200-x.
(236) Fink, A. L. Protein Aggregation: Folding Aggregates, Inclusion Bodies and Amyloid. *Folding and Design* **1998**, *3* (1), R9–R23. https://doi.org/10.1016/S1359-0278(98)00002-9.
(237) *Labeling of a protein with fluorophores using maleimide derivitization - PubMed*. https://pubmed.ncbi.nlm.nih.gov/24423268/ (accessed 2022-11-12).
(238) McParland, V. J.; Kad, N. M.; Kalverda, A. P.; Brown, A.; Kirwin-Jones, P.; Hunter, M. G.; Sunde, M.; Radford, S. E. Partially Unfolded States of B2-Microglobulin and Amyloid Formation in Vitro. *Biochemistry* **2000**, *39* (30), 8735–8746. https://doi.org/10.1021/bi000276j.
(239) Gasser, B.; Saloheimo, M.; Rinas, U.; Dragosits, M.; Rodríguez-Carmona, E.; Baumann, K.; Giuliani, M.; Parrilli, E.; Branduardi, P.; Lang, C.; Porro, D.; Ferrer, P.; Tutino, M. L.; Mattanovich, D.; Villaverde, A. Protein Folding and Conformational Stress in Microbial Cells Producing Recombinant Proteins: A Host Comparative Overview. *Microb Cell Fact* **2008**, *7*, 11. https://doi.org/10.1186/1475-2859-7-11.
(240) Cole, J. L.; Lary, J. W.; Moody, T.; Laue, T. M. Analytical Ultracentrifugation: Sedimentation Velocity and Sedimentation Equilibrium. *Methods Cell Biol* **2008**, *84*, 143–179. https://doi.org/10.1016/S0091-679X(07)84006-4.
(241) Xu, S. C. S.; LoRicco, J. G.; Bishop, A. C.; James, N. A.; Huynh, W. H.; McCallum, S. A.; Roan, N. R.; Makhatadze, G. I. Sequence-Independent Recognition of the Amyloid Structural Motif by GFP Protein Family. *Proceedings of the National Academy of Sciences* **2020**, *117* (36), 22122–22127. https://doi.org/10.1073/pnas.2001457117.
(242) Iadanza, M. G.; Jackson, M. P.; Hewitt, E. W.; Ranson, N. A.; Radford, S. E. A New Era for Understanding Amyloid Structures and Disease. *Nat Rev Mol Cell Biol* **2018**, *19* (12), 755–773. https://doi.org/10.1038/s41580-018-0060-8.
(243) Rambaran, R. N.; Serpell, L. C. Amyloid Fibrils. *Prion* **2008**, *2* (3), 112–117.
(244) Dobson, C. M. Protein Folding and Misfolding. *Nature; London* **2003**, *426* (6968), 884–890.
(245) Eisenberg, D. S.; Sawaya, M. R. Structural Studies of Amyloid Proteins at the Molecular Level. *Annu Rev Biochem* **2017**, *86*, 69–95. https://doi.org/10.1146/annurev-biochem-061516-045104.
(246) Ivanova, M. I.; Sawaya, M. R.; Gingery, M.; Attinger, A.; Eisenberg, D. An Amyloid-Forming Segment of 2-Microglobulin Suggests a Molecular Model for the Fibril. *Proceedings of the National Academy of Sciences* **2004**, *101* (29), 10584–10589. https://doi.org/10.1073/pnas.0403756101.
(247) Chiti, F.; Dobson, C. M. Protein Misfolding, Functional Amyloid, and Human Disease. *Annu. Rev. Biochem.* **2006**, *75* (1), 333–366. https://doi.org/10.1146/annurev.biochem.75.101304.123901.

(248) Sipe, J. D.; Benson, M. D.; Buxbaum, J. N.; Ikeda, S.; Merlini, G.; Saraiva, M. J. M.; Westermark, P. Amyloid Fibril Proteins and Amyloidosis: Chemical Identification and Clinical Classification International Society of Amyloidosis 2016 Nomenclature Guidelines. *Amyloid* **2016**, *23* (4), 209–213. https://doi.org/10.1080/13506129.2016.1257986.
(249) Chiti, F.; Dobson, C. M. Protein Misfolding, Amyloid Formation, and Human Disease: A Summary of Progress Over the Last Decade. *Annu Rev Biochem* **2017**, *86*, 27–68. https://doi.org/10.1146/annurev-biochem-061516-045115.
(250) Sipe, J. D.; Cohen, A. S. Review: History of the Amyloid Fibril. *Journal of Structural Biology* **2000**, *130* (2), 88–98. https://doi.org/10.1006/jsbi.2000.4221.
(251) Blancas-Mejía, L. M.; Ramirez-Alvarado, M. Systemic Amyloidoses. *Annu Rev Biochem* **2013**, *82*, 745–774. https://doi.org/10.1146/annurev-biochem-072611-130030.
(252) Baumgart, J.-V.; Stuhlmann-Laeisz, C.; Hegenbart, U.; Nattenmüller, J.; Schönland, S.; Krüger, S.; Behrens, H.-M.; Röcken, C. Local vs. Systemic Pulmonary Amyloidosis—Impact on Diagnostics and Clinical Management. *Virchows Arch* **2018**, *473* (5), 627–637. https://doi.org/10.1007/s00428-018-2442-x.
(253) McLean, C. A.; Cherny, R. A.; Fraser, F. W.; Fuller, S. J.; Smith, M. J.; Beyreuther, K.; Bush, A. I.; Masters, C. L. Soluble Pool of Abeta Amyloid as a Determinant of Severity of Neurodegeneration in Alzheimer's Disease. *Ann Neurol* **1999**, *46* (6), 860–866. https://doi.org/10.1002/1531-8249(199912)46:6<860::aid-ana8>3.0.co;2-m.
(254) Lue, L.-F.; Kuo, Y.-M.; Roher, A. E.; Brachova, L.; Shen, Y.; Sue, L.; Beach, T.; Kurth, J. H.; Rydel, R. E.; Rogers, J. Soluble Amyloid β Peptide Concentration as a Predictor of Synaptic Change in Alzheimer's Disease. *The American Journal of Pathology* **1999**, *155* (3), 853–862. https://doi.org/10.1016/S0002-9440(10)65184-X.
(255) Caughey, B.; Lansbury, P. T. PROTOFIBRILS, PORES, FIBRILS, AND NEURODEGENERATION: Separating the Responsible Protein Aggregates from The Innocent Bystanders. *Annual Review of Neuroscience* **2003**, *26* (1), 267–298. https://doi.org/10.1146/annurev.neuro.26.010302.081142.
(256) Dear, A. J.; Michaels, T. C. T.; Meisl, G.; Klenerman, D.; Wu, S.; Perrett, S.; Linse, S.; Dobson, C. M.; Knowles, T. P. J. Kinetic Diversity of Amyloid Oligomers. *Proceedings of the National Academy of Sciences* **2020**, *117* (22), 12087–12094. https://doi.org/10.1073/pnas.1922267117.
(257) Ebo, J. S.; Guthertz, N.; Radford, S. E.; Brockwell, D. J. Using Protein Engineering to Understand and Modulate Aggregation. *Current Opinion in Structural Biology* **2020**, *60*, 157–166. https://doi.org/10.1016/j.sbi.2020.01.005.
(258) L. Almeida, Z.; M. M. Brito, R. Structure and Aggregation Mechanisms in Amyloids. *Molecules* **2020**, *25* (5), 1195. https://doi.org/10.3390/molecules25051195.
(259) Quintas, A.; Saraiva, M. j. m; Brito, R. M. M. The Amyloidogenic Potential of Transthyretin Variants Correlates with Their Tendency to Aggregate in Solution. *FEBS Letters* **1997**, *418* (3), 297–300. https://doi.org/10.1016/S0014-5793(97)01398-7.
(260) Jesus, C. S. H.; Almeida, Z. L.; Vaz, D. C.; Faria, T. Q.; Brito, R. M. M. A New Folding Kinetic Mechanism for Human Transthyretin and the Influence of the

Amyloidogenic V30M Mutation. *International Journal of Molecular Sciences* **2016**, *17* (9), 1428. https://doi.org/10.3390/ijms17091428.
(261) Isaacson, R. L.; Weeds, A. G.; Fersht, A. R. Equilibria and Kinetics of Folding of Gelsolin Domain 2 and Mutants Involved in Familial Amyloidosis–Finnish Type. *Proceedings of the National Academy of Sciences* **1999**, *96* (20), 11247–11252. https://doi.org/10.1073/pnas.96.20.11247.
(262) Grant, M. A.; Lazo, N. D.; Lomakin, A.; Condron, M. M.; Arai, H.; Yamin, G.; Rigby, A. C.; Teplow, D. B. Familial Alzheimer's Disease Mutations Alter the Stability of the Amyloid β-Protein Monomer Folding Nucleus. *Proceedings of the National Academy of Sciences* **2007**, *104* (42), 16522–16527. https://doi.org/10.1073/pnas.0705197104.
(263) Dobson, C. M. Protein Misfolding, Evolution and Disease. *Trends in Biochemical Sciences* **1999**, *24* (9), 329–332. https://doi.org/10.1016/S0968-0004(99)01445-0.
(264) Thirumalai, D.; Klimov, D. K.; Dima, R. I. Emerging Ideas on the Molecular Basis of Protein and Peptide Aggregation. *Curr Opin Struct Biol* **2003**, *13* (2), 146–159. https://doi.org/10.1016/s0959-440x(03)00032-0.
(265) Andrews, J. M.; Roberts, C. J. A Lumry−Eyring Nucleated Polymerization Model of Protein Aggregation Kinetics: 1. Aggregation with Pre-Equilibrated Unfolding. *J. Phys. Chem. B* **2007**, *111* (27), 7897–7913. https://doi.org/10.1021/jp070212j.
(266) Cohen, S. I. A.; Linse, S.; Luheshi, L. M.; Hellstrand, E.; White, D. A.; Rajah, L.; Otzen, D. E.; Vendruscolo, M.; Dobson, C. M.; Knowles, T. P. J. Proliferation of Amyloid-B42 Aggregates Occurs through a Secondary Nucleation Mechanism. *Proceedings of the National Academy of Sciences* **2013**, *110* (24), 9758–9763. https://doi.org/10.1073/pnas.1218402110.
(267) Mazzini, G.; Ricagno, S.; Caminito, S.; Rognoni, P.; Milani, P.; Nuvolone, M.; Basset, M.; Foli, A.; Russo, R.; Merlini, G.; Palladini, G.; Lavatelli, F. Protease-sensitive Regions in Amyloid Light Chains: What a Common Pattern of Fragmentation across Organs Suggests about Aggregation. *FEBS J* **2022**, *289* (2), 494–506. https://doi.org/10.1111/febs.16182.
(268) Selkoe, D. J.; Hardy, J. The Amyloid Hypothesis of Alzheimer's Disease at 25 Years. *EMBO Molecular Medicine* **2016**, *8* (6), 595–608. https://doi.org/10.15252/emmm.201606210.
(269) Chun Ke, P.; Zhou, R.; C. Serpell, L.; Riek, R.; J. Knowles, T. P.; A. Lashuel, H.; Gazit, E.; W. Hamley, I.; P. Davis, T.; Fändrich, M.; Erik Otzen, D.; R. Chapman, M.; M. Dobson, C.; S. Eisenberg, D.; Mezzenga, R. Half a Century of Amyloids: Past, Present and Future. *Chemical Society Reviews* **2020**, *49* (15), 5473–5509. https://doi.org/10.1039/C9CS00199A.
(270) Meisl, G.; Yang, X.; Hellstrand, E.; Frohm, B.; Kirkegaard, J. B.; Cohen, S. I. A.; Dobson, C. M.; Linse, S.; Knowles, T. P. J. Differences in Nucleation Behavior Underlie the Contrasting Aggregation Kinetics of the Aβ40 and Aβ42 Peptides. *Proceedings of the National Academy of Sciences* **2014**, *111* (26), 9384–9389. https://doi.org/10.1073/pnas.1401564111.

(271) Knowles, T. P. J.; Vendruscolo, M.; Dobson, C. M. The Amyloid State and Its Association with Protein Misfolding Diseases. *Nat Rev Mol Cell Biol* **2014**, *15* (6), 384–396. https://doi.org/10.1038/nrm3810.
(272) Michaels, T. C. T.; Šarić, A.; Curk, S.; Bernfur, K.; Arosio, P.; Meisl, G.; Dear, A. J.; Cohen, S. I. A.; Dobson, C. M.; Vendruscolo, M.; Linse, S.; Knowles, T. P. J. Dynamics of Oligomer Populations Formed during the Aggregation of Alzheimer's Aβ42 Peptide. *Nat. Chem.* **2020**, *12* (5), 445–451. https://doi.org/10.1038/s41557-020-0452-1.
(273) Karamanos, T. K.; Jackson, M. P.; Calabrese, A. N.; Goodchild, S. C.; Cawood, E. E.; Thompson, G. S.; Kalverda, A. P.; Hewitt, E. W.; Radford, S. E. Structural Mapping of Oligomeric Intermediates in an Amyloid Assembly Pathway. *eLife* **2019**, *8*, e46574. https://doi.org/10.7554/eLife.46574.
(274) Gejyo, F.; Yamada, T.; Odani, S.; Nakagawa, Y.; Arakawa, M.; Kunitomo, T.; Kataoka, H.; Suzuki, M.; Hirasawa, Y.; Shirahama, T.; Cohen, A. S.; Schmid, K. A New Form of Amyloid Protein Associated with Chronic Hemodialysis Was Identified as B2-Microglobulin. *Biochemical and Biophysical Research Communications* **1985**, *129* (3), 701–706. https://doi.org/10.1016/0006-291X(85)91948-5.
(275) Cornwell, O.; Radford, S. E.; Ashcroft, A. E.; Ault, J. R. Comparing Hydrogen Deuterium Exchange and Fast Photochemical Oxidation of Proteins: A Structural Characterisation of Wild-Type and ΔN6 B2-Microglobulin. *J. Am. Soc. Mass Spectrom.* **2018**, *29* (12), 2413–2426. https://doi.org/10.1007/s13361-018-2067-y.
(276) Loureiro, R. J. S.; Faísca, P. F. N. The Early Phase of B2-Microglobulin Aggregation: Perspectives From Molecular Simulations. *Frontiers in Molecular Biosciences* **2020**, *7*.
(277) Hodkinson, J. P.; Radford, S. E.; Ashcroft, A. E. The Role of Conformational Flexibility in B2-Microglobulin Amyloid Fibril Formation at Neutral PH. *Rapid Communications in Mass Spectrometry* **2012**, *26* (16), 1783–1792. https://doi.org/10.1002/rcm.6282.
(278) Platt, G. W.; Radford, S. E. Glimpses of the Molecular Mechanisms of B2-Microglobulin Fibril Formation in Vitro: Aggregation on a Complex Energy Landscape. *FEBS Letters* **2009**, *583* (16), 2623–2629. https://doi.org/10.1016/j.febslet.2009.05.005.
(279) Yamamoto, S.; Hasegawa, K.; Yamaguchi, I.; Goto, Y.; Gejyo, F.; Naiki, H. Kinetic Analysis of the Polymerization and Depolymerization of B2-Microglobulin-Related Amyloid Fibrils in Vitro. *Biochimica et Biophysica Acta (BBA) - Proteins and Proteomics* **2005**, *1753* (1), 34–43. https://doi.org/10.1016/j.bbapap.2005.07.007.
(280) Karamanos, T. K.; Pashley, C. L.; Kalverda, A. P.; Thompson, G. S.; Mayzel, M.; Orekhov, V. Y.; Radford, S. E. A Population Shift between Sparsely Populated Folding Intermediates Determines Amyloidogenicity. *J. Am. Chem. Soc.* **2016**, *138* (19), 6271–6280. https://doi.org/10.1021/jacs.6b02464.
(281) Valleix, S.; Gillmore, J. D.; Bridoux, F.; Mangione, P. P.; Dogan, A.; Nedelec, B.; Boimard, M.; Touchard, G.; Goujon, J.-M.; Lacombe, C.; Lozeron, P.; Adams, D.; Lacroix, C.; Maisonobe, T.; Planté-Bordeneuve, V.; Vrana, J. A.; Theis, J. D.; Giorgetti, S.; Porcari, R.; Ricagno, S.; Bolognesi, M.; Stoppini, M.; Delpech, M.; Pepys, M. B.; Hawkins, P. N.; Bellotti, V. Hereditary Systemic Amyloidosis Due

to Asp76Asn Variant B2-Microglobulin. *New England Journal of Medicine* **2012**, *366* (24), 2276–2283. https://doi.org/10.1056/NEJMoa1201356.
(282) Rosa, M. de; Barbiroli, A.; Giorgetti, S.; Mangione, P. P.; Bolognesi, M.; Ricagno, S. Decoding the Structural Bases of D76N SS2-Microglobulin High Amyloidogenicity through Crystallography and Asn-Scan Mutagenesis. *PLOS ONE* **2015**, *10* (12), e0144061. https://doi.org/10.1371/journal.pone.0144061.
(283) Cawood, E. E.; Karamanos, T. K.; Wilson, A. J.; Radford, S. E. Visualizing and Trapping Transient Oligomers in Amyloid Assembly Pathways. *Biophysical Chemistry* **2021**, *268*, 106505. https://doi.org/10.1016/j.bpc.2020.106505.
(284) Karamanos, T. K.; Kalverda, A. P.; Radford, S. E. Generating Ensembles of Dynamic Misfolding Proteins. *Frontiers in Neuroscience* **2022**, *16*.
(285) Michaels, T. C. T.; Šarić, A.; Habchi, J.; Chia, S.; Meisl, G.; Vendruscolo, M.; Dobson, C. M.; Knowles, T. P. J. Chemical Kinetics for Bridging Molecular Mechanisms and Macroscopic Measurements of Amyloid Fibril Formation. *Annu Rev Phys Chem* **2018**, *69*, 273–298. https://doi.org/10.1146/annurev-physchem-050317-021322.
(286) Uralcan, B.; Longo, T. J.; Anisimov, M. A.; Stillinger, F. H.; Debenedetti, P. G. Interconversion-Controlled Liquid–Liquid Phase Separation in a Molecular Chiral Model. *J. Chem. Phys.* **2021**, *155* (20), 204502. https://doi.org/10.1063/5.0071988.
(287) Longo, T. J.; Anisimov, M. A. Phase Transitions Affected by Natural and Forceful Molecular Interconversion. *J. Chem. Phys.* **2022**, *156* (8), 084502. https://doi.org/10.1063/5.0081180.
(288) Longo, T. J.; Anisimov, M. A. Phase Transitions Affected by Molecular Interconversion. *arXiv:2102.11148 [cond-mat]* **2021**.
(289) Fitzner, M.; Sosso, G. C.; Pietrucci, F.; Pipolo, S.; Michaelides, A. Pre-Critical Fluctuations and What They Disclose about Heterogeneous Crystal Nucleation. *Nat Commun* **2017**, *8* (1), 2257. https://doi.org/10.1038/s41467-017-02300-x.
(290) Chung, H. S. Transition Path Times Measured by Single-Molecule Spectroscopy. *Journal of Molecular Biology* **2018**, *430* (4), 409–423. https://doi.org/10.1016/j.jmb.2017.05.018.
(291) Kramers, H. A. Brownian Motion in a Field of Force and the Diffusion Model of Chemical Reactions. *Physica* **1940**, *7* (4), 284–304. https://doi.org/10.1016/S0031-8914(40)90098-2.
(292) Marchand, T. L.; Rosa, M. de; Salvi, N.; Sala, B. M.; Andreas, L. B.; Barbet-Massin, E.; Sormanni, P.; Barbiroli, A.; Porcari, R.; Mota, C. S.; Sanctis, D. de; Bolognesi, M.; Emsley, L.; Bellotti, V.; Blackledge, M.; Camilloni, C.; Pintacuda, G.; Ricagno, S. Conformational Dynamics in Crystals Reveal the Molecular Bases for D76N Beta-2 Microglobulin Aggregation Propensity. *Nature Communications* **2018**, *9* (1), 1658. https://doi.org/10.1038/s41467-018-04078-y.
(293) *Foerster Resonance Energy Transfer (FRET) | PicoQuant*. https://www.picoquant.com/applications/category/life-science/foerster-resonance-energy-transfer-fret (accessed 2022-11-21).
(294) Merchant, K. A.; Best, R. B.; Louis, J. M.; Gopich, I. V.; Eaton, W. A. Characterizing the Unfolded States of Proteins Using Single-Molecule FRET

Spectroscopy and Molecular Simulations. *Proceedings of the National Academy of Sciences* **2007**, *104* (5), 1528–1533. https://doi.org/10.1073/pnas.0607097104.
(295) Rüttinger, S.; Kapusta, P.; Patting, M.; Wahl, M.; Macdonald, R. On the Resolution Capabilities and Limits of Fluorescence Lifetime Correlation Spectroscopy (FLCS) Measurements. *J Fluoresc* **2010**, *20* (1), 105–114. https://doi.org/10.1007/s10895-009-0528-1.
(296) Gambin, Y.; Schug, A.; Lemke, E. A.; Lavinder, J. J.; Ferreon, A. C. M.; Magliery, T. J.; Onuchic, J. N.; Deniz, A. A. Direct Single-Molecule Observation of a Protein Living in Two Opposed Native Structures. *Proceedings of the National Academy of Sciences* **2009**, *106* (25), 10153–10158. https://doi.org/10.1073/pnas.0904461106.
(297) de Boer, M.; Gouridis, G.; Vietrov, R.; Begg, S. L.; Schuurman-Wolters, G. K.; Husada, F.; Eleftheriadis, N.; Poolman, B.; McDevitt, C. A.; Cordes, T. Conformational and Dynamic Plasticity in Substrate-Binding Proteins Underlies Selective Transport in ABC Importers. *eLife* **2019**, *8*, e44652. https://doi.org/10.7554/eLife.44652.
(298) Deniz, A. A.; Dahan, M.; Grunwell, J. R.; Ha, T.; Faulhaber, A. E.; Chemla, D. S.; Weiss, S.; Schultz, P. G. Single-Pair Fluorescence Resonance Energy Transfer on Freely Diffusing Molecules: Observation of Förster Distance Dependence and Subpopulations. *Proceedings of the National Academy of Sciences* **1999**, *96* (7), 3670–3675. https://doi.org/10.1073/pnas.96.7.3670.
(299) Deniz, A. A.; Laurence, T. A.; Beligere, G. S.; Dahan, M.; Martin, A. B.; Chemla, D. S.; Dawson, P. E.; Schultz, P. G.; Weiss, S. Single-Molecule Protein Folding: Diffusion Fluorescence Resonance Energy Transfer Studies of the Denaturation of Chymotrypsin Inhibitor 2. *Proceedings of the National Academy of Sciences* **2000**, *97* (10), 5179–5184. https://doi.org/10.1073/pnas.090104997.
(300) Deniz, A. A.; Mukhopadhyay, S.; Lemke, E. A. Single-Molecule Biophysics: At the Interface of Biology, Physics and Chemistry. *Journal of The Royal Society Interface* **2008**, *5* (18), 15–45. https://doi.org/10.1098/rsif.2007.1021.
(301) Michalet, X.; Weiss, S.; Jäger, M. Single-Molecule Fluorescence Studies of Protein Folding and Conformational Dynamics. *Chem. Rev.* **2006**, *106* (5), 1785–1813. https://doi.org/10.1021/cr0404343.
(302) Gopich, I. V.; Szabo, A. FRET Efficiency Distributions of Multistate Single Molecules. *J. Phys. Chem. B* **2010**, *114* (46), 15221–15226. https://doi.org/10.1021/jp105359z.
(303) Loureiro, R. J. S.; Faísca, P. F. N. The Early Phase of B2-Microglobulin Aggregation: Perspectives From Molecular Simulations. *Front Mol Biosci* **2020**, *7*, 578433. https://doi.org/10.3389/fmolb.2020.578433.
(304) Otzen, D. E. Protein Unfolding in Detergents: Effect of Micelle Structure, Ionic Strength, PH, and Temperature. *Biophysical Journal* **2002**, *83* (4), 2219–2230. https://doi.org/10.1016/S0006-3495(02)73982-9.
(305) Jelińska, A.; Zagożdżon, A.; Górecki, M.; Wisniewska, A.; Frelek, J.; Holyst, R. Denaturation of Proteins by Surfactants Studied by the Taylor Dispersion Analysis. *PLoS One* **2017**, *12* (4), e0175838. https://doi.org/10.1371/journal.pone.0175838.

(306) Dib, N.; Lépori, C. M. O.; Correa, N. M.; Silber, J. J.; Falcone, R. D.; García-Río, L. Biocompatible Solvents and Ionic Liquid-Based Surfactants as Sustainable Components to Formulate Environmentally Friendly Organized Systems. *Polymers (Basel)* **2021**, *13* (9), 1378. https://doi.org/10.3390/polym13091378.
(307) Ali, M. K.; Moshikur, R. M.; Wakabayashi, R.; Tahara, Y.; Moniruzzaman, M.; Kamiya, N.; Goto, M. Synthesis and Characterization of Choline-Fatty-Acid-Based Ionic Liquids: A New Biocompatible Surfactant. *J Colloid Interface Sci* **2019**, *551*, 72–80. https://doi.org/10.1016/j.jcis.2019.04.095.
(308) Farrag, S. A.; Rageh, A. H.; Askal, H. F.; Saleh, G. A. Biocompatible Magnetite Nanoparticles Coated with Ionic Liquid-Based Surfactantas a Hydrophilic Sorbent for Dispersive Solid Phase Microextraction of Cephalosporins Prior to Their Quantitation by HPTLC. *Journal of Chromatography B* **2022**, *1205*, 123339. https://doi.org/10.1016/j.jchromb.2022.123339.
(309) Longo, T. J.; Anisimov, M. A. Phase Transitions Affected by Natural and Forceful Molecular Interconversion. *J. Chem. Phys.* **2022**, *156* (8), 084502. https://doi.org/10.1063/5.0081180.
(310) Uralcan, B.; Longo, T. J.; Anisimov, M. A.; Stillinger, F. H.; Debenedetti, P. G. Interconversion-Controlled Liquid–Liquid Phase Separation in a Molecular Chiral Model. *J. Chem. Phys.* **2021**, *155* (20), 204502. https://doi.org/10.1063/5.0071988.